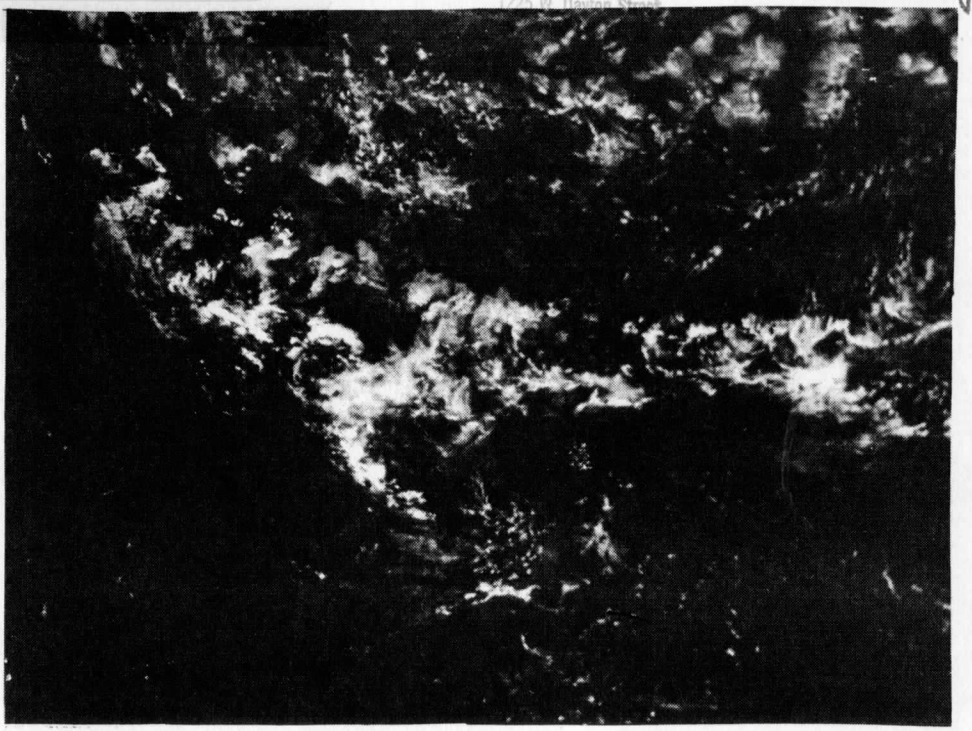

STUDIES OF THE ATMOSPHERE USING AEROSPACE PROBES

Annual Scientific Report - 1974

NOAA Grant 04-3-158-61

Space Science and Engineering Center
University of Wisconsin - Madison

March 1975

COVER ILLUSTRATION

U.S. Defense Meteorological Satellite Program image 7 August 1973 at 1600 GMT covering the area 15°-35°N, 45°-70°W. Resolution is about 1/3 nm. At 20°N, 60°W American, Russian, and Mexican ships met to intercompare observations from their several sensor systems which were to be used in the GARP Atlantic Tropical Experiment (GATE). The SSEC contributions to the GATE Intercomparison Sea Trial (GIST) were Prof. Verner Suomi and the Boundary Layer Instrumentation System (BLIS). The paper by Dr. Elizabeth A. Berman presents some of the scientific findings from the BLIS-GIST data.

STUDIES OF THE ATMOSPHERE

USING AEROSPACE PROBES

1974

STUDIES OF THE ATMOSPHERE

USING AEROSPACE PROBES

1974

Annual Report, NOAA Grant 04-3-158-61

The research reported in this document has been supported by the National Oceanic and Atmospheric Administration.

March 1975

Published for the

Space Science and Engineering Center

by the

University of Wisconsin Press

Published 1975
The University of Wisconsin Press
Box 1379, Madison, Wisconsin 53701

The University of Wisconsin Press, Ltd.
70 Great Russell Street, London

First Printing

Printed in the United States of America

ISBN 0-299-97056-6

This work is a result of research sponsored by the NOAA National Environmental Satellite Service, Department of Commerce, under Grant No. 04-3-158-61. The U. S. Government is authorized to produce and distribute reprints for governmental purposes notwithstanding any copyright notation that may appear hereon.

Correspondence concerning editorial matters should be addressed to
Space Science and Engineering Center
University of Wisconsin
1225 West Dayton Street
Madison, Wisconsin 53706

Orders for copies of this report should be addressed to
The University of Wisconsin Press

Principal Investigator: Verner E. Suomi

Contributors: B. Auvine

E. A. Berman

D. W. Martin

R. E. Peterson

D. N. Sikdar

University of Wisconsin

CONTENTS

PREFACE

The GARP Atlantic Tropical Experiment (GATE) took precedence over most other meteorological research during 1974, and the number of publishable papers has been reduced as a consequence. We anticipate a larger volume as GATE results become available during 1975.

I am pleased to include Dr. Elizabeth Berman's thesis in this report. The data upon which her work is based was collected during a pre-GATE test by the untried Boundary Layer Instrumentation Systems (BLIS). As expected, the data were noisy and bore evidence of several BLIS faults discovered during the test. Nevertheless, Dr. Berman was able to extract some very interesting and scientifically important results.

My sincere thanks are extended to the authors and to all those in SSEC who helped in the work reported upon here. We are very grateful to the National Oceanic and Atmospheric Administration for the continuing support which makes our work possible.

Verner E. Suomi
Principal Investigator

CLOUD BUBBLES AND SQUALLS:

THE ANATOMY OF AN ATLANTIC TROPICAL DISTURBANCE

David W. Martin and Dhirendra N. Sikdar

ABSTRACT

Geosynchronous satellite pictures for 23 July 1969 show a small, very active cloud cluster in the western equatorial Atlantic. This cluster lay just inside a much larger cloud ring or "bubble," which persisted, growing in area, through the entire seven-hour picture sequence. Westerly movement of the bubble cloud carried it over the research ship Oceanographer, on station for the Barbados Oceanographic and Meteorological Experiment.

Using the Man-Computer Interactive Data Access System (McIDAS), measurements were made of bubble location and area, cluster location, and cloud tracer locations in the vicinity of the bubble. Time changes for these yielded velocities for the bubble cloud cluster, divergence of the bubble cloud, and a low level stream field for the bubble and its environment. Three hourly soundings from the Oceanographer were analyzed as time series of temperature, relative humidity and equivalent potential temperature, and also as hodographs of wind.

Satellite measurements yielded a large positive divergence for the bubble cloud, 2×10^{-5} sec^{-1}. Low level winds show the bubble cloud and cluster as a distinctly squall-like structure in a cyclonically sheared field. The indication of a squall structure is confirmed by the Oceanographer's soundings. These define a low tropospheric pocket of air that in terms of its moisture and equivalent potential temperature is both dry and cold relative to the air around. The bubble, it is concluded, was formed by cumulus clouds marking the boundary of near-surface outflow air from unsaturated downdrafts within the cluster.

This study compares satellite and surface conventional observations to document and understand a particular atmospheric event. In so doing, it demonstrates the use of McIDAS to measure time dependent characteristics of clouds with a focus and a precision that begin to match the focus and precision of ground-based systems, and turn out to be highly complementary as well.

1. INTRODUCTION

Much of the fascination of watching movie loops of satellite pictures lies in the discovery--in finding in the moving clouds a new pattern or structure. The interest is especially high if there are ground-based observations close to this feature, for then hypotheses on its nature can be tested. Such a case is described here.

The picture sequence is from the Applications Technology Satellite (ATS-3). It covers almost seven hours on 23 July (day 204), 1969, at a basic interval of 27 minutes. (An abbreviated sequence is reproduced in Figure 1). When viewed as a "movie" loop, these pictures show a small cloud cluster steaming up a band of scattered cumulus clouds, very much as a flame sparks along a fuse. Even more remarkable is the cloud ring or "bubble" which intercepts the cluster. This bubble cloud persists throughout the sequence. It is large in the first picture--several times the size of the cluster--and grows visibly as it moves westward. The presence of the active cluster within and along the bubble suggests an origin in convective downdrafts--the bubble was formed by cumulus clouds marking the boundary of near-surface outflow air from unsaturated downdrafts within the cluster. It is this hypothesis which is tested against measurements on the satellite picture sequence and observations from the research ship Oceanographer.

2. BACKGROUND AND SETTING

ATS-3 produced visible-wavelength images, with a ground resolution in the area of interest of about 5 km. The images analyzed here are television displays generated from digital magnetic tapes on the University of Wisconsin's Man-Computer Interactive Data Access System.

The Oceanographer, as the southernmost of the ships participating in the Barbados Oceanographic and Meteorological Experiment, occupied a station at 7° 30' N, 52° 42' W. It took soundings of temperature, moisture, and wind every three hours (for details, see de la Moriniere, 1972).

The cluster and bubble formed near the intersection of a meridional cloud band with the Intertropical Cloud Band (ITCB) (Figure 2).[1] The meridional band was associated with a moisture pattern--moist low-troposphere, dry mid-troposphere--representing relatively high potential instability. This instability was loosely bound by a weak trade inversion. Behind the westward moving cloud band and along the ITCB lay a clear tongue associated with the leading edge of a mid-tropospheric pool of warm, dry air of Saharan origin.

---

[1] A more complete description of the larger scale setting is given in Martin and Sikdar (1974).

3. CLOUDS, WINDS, AND DIVERGENCE

A tracing of bubble cloud positions (Figure 3) shows regular growth and steady movement at 10.4 m sec^{-1} toward the west. The cluster moved slightly north of west, at a substantially higher speed: 15.3 m sec^{-1}; thus, over the picture sequence, it slid along the inside of the bubble from the northern sector to the northwest sector, following the point of intersection of the meridional cloud band with the bubble cloud.

Using McIDAS, the area of the bubble was measured on six pictures spanning the sequence. A plot of these areas shows expansion throughout the period, at a steadily decreasing rate (Figure 4). Thus, although the area-averaged divergence, computed from the formula

$$\text{div} = \frac{1}{A}\frac{\Delta A}{\Delta t},$$

decreased also by an order of magnitude over the period; its 2 x 10^{-5} sec^{-1} average over six hours represents quite strongly divergent flow.

A low cloud tracer wind field, computed on McIDAS from the last three pictures in the sequence, affords a snapshot view of flow along and outside the bubble (Figure 5). Despite the absence of good low cloud tracers within the bubble, the overall pattern is well defined. Flow is confluent along the ITCB. It is difluent within the bubble cloud, which has evolved in a cyclonic shear zone of the easterly flow. The bubble not only encloses air of markedly divergent character, it defines the boundary between air masses of markedly different characteristics. Dynamically, what is suggested is a squall, embedded in a slightly convergent, sheared easterly flow.

The Oceanographer's rawinsonde observations show this easterly current extended to at least 400 mb (Figure 6). Vertical shear was weak within and behind the bubble cloud; however, ahead of the bubble midtropospheric winds were some 15 m sec^{-1} stronger than winds near the surface. Interestingly, it is only in this sounding that winds at any level matched the velocity of the cluster; this match occurred at 480 mb.

4. TEMPERATURE, MOISTURE, AND UNSATURATED DOWNDRAFTS

Temperature, moisture, and equivalent potential temperature from the Oceanographer's soundings are presented as time-height sections. (Details of the sounding characteristics and processing are given in Martin and Sikdar). The time of passage of the bubble cloud's trailing edge across the Oceanographer was estimated from the satellite pictures to be 1228 GMT, with an uncertainty of $\pm$ 20 minutes; time of passage of the leading edge was estimated to be 0439 GMT, with an uncertainty of $\pm$ 1.6 hours.

Temperature is treated as an anomaly--the difference between observed temperatures and Jordan's (1958) mean July sounding for the West Indies. The three soundings taken as the bubble cloud passed define a warm pocket at 700 mb (Figure 7a). These stand our sharply from the flat pattern around.

Most notable in the relative humidity time section (Figure 7b) is the dish-like dry pocket which extends from 800 mb down to the surface. Above it is a moist layer, with humidities in excess of 90%. This is separated from a deeper moist layer centered at 625 mb by an upward arching shell of quite dry air that appears to be connected at its eastern end with the dry pocket below.

Temperature and moisture soundings both define a cell, within which atmospheric properties and structure are quite different from those around. The time section of equivalent potential temperature (Figure 7c) shows that, relative to its environment, most of the air within this cell is potentially cold. The tongue of coldest air, at the top, arcs downward on the trailing side toward the surface, where θ_e values are 8 to 10°K colder than those outside of the bubble cloud.

These soundings provide information essential to understanding what the bubble cloud represents. They confirm what was inferred from the satellite pictures, that the bubble cloud was a low tropospheric phenomenon. They also help locate the source of the near surface divergent air. There was no plausibly close upstream low level source for air of such dry, potentially cold characteristics. There was, however, a middle level source--the layer between 750 and 450 mb. Moderately low θ_e values within the bubble cloud suggest the mechanism for transport of this air toward the surface was evaporative cooling, occurring within rain areas. This implies very local transport, in downdrafts--an inference consistent with the smooth, oval boundary of the divergent air. Finally, the soundings penetrated air that was dry; thus, in spite of evaporation, the downdrafts were unsaturated.

Excepting perhaps the 1145 GMT sounding, there is little evidence these downdrafts occurred over the Oceanographer. (The presence of dry layers is testimony against deep convection as well; a conclusion which is consistent with the satellite pictures). The winds, however, point to a source for the outflow air in the northern part of the bubble. Although the bright clouds along the trailing edge are one possibility, the cluster at the top, by its position, movement, and activity, is a much more likely source, at least over the period of the picture sequence.

5. PERSPECTIVE

In form and behavior, the bubble cloud is similar to the cloud arcs described by Oliver and Purdom (1974) and Purdom (1974)--arcs which emanate from thunderstorms, and are attributed to surface outflow from rain cooled air within the thunderstorms. Although such arcs are best known from subtropical and middle latitude thunderstorms, Zipser (1969) has documented an East Pacific equatorial arc cloud disturbance bearing a striking resemblance to the Atlantic system. Like the Atlantic disturbance, this Pacific disturbance, had definite squall characteristics, including massive transport of cold midtropospheric air in unsaturated downdrafts, spreading of this air near the surface, and the formation of a cloud arc marking the boundary of the outflow air. At this point, however, the evolutions diverged. Whereas in the Pacific disturbance deep convection died near or shortly after the time the arc cloud appeared, in the Atlantic disturbance deep convection continued

through the whole six hour period of bubble cloud presence. Convection in the Pacific disturbance was overtaken, undercut, and killed by outflow air; convection in the Atlantic disturbance held its position along the outflow boundary and thrived. The presence of the cloud band along which the cluster was moving accounts for part of this unusual longevity. But a more important factor is found in dynamics. Although in both cases there was a low tropospheric maximum in the easterly flow, upper tropospheric flows were opposite: westerlies strongly opposing convective cell movement in the Pacific disturbance, easterlies weakly opposing cell movement in the Atlantic disturbance. Convection in the weakly sheared Atlantic environment was able to keep pace with the outflow boundary.

The point of view we began with--that movie loop satellite pictures are fascinating to watch--is familiar to most of us. Perhaps the real significance of this study is its demonstration of how the new tool called McIDAS can be used to probe more deeply into the flesh and bone of nature's cloud creations. With McIDAS, we can measure as well as see. Precise measurements of location, area, and brightness, and their changes in time give us a set of information that begins to match that available from ground based systems such as rawinsondes, and turns out to be highly complementary as well. Comparative studies of the type described here accomplish two things: we learn something about clouds and the organization of the atmosphere, and we also learn about satellites and how to interpret the observations they provide.

ACKNOWLEDGEMENTS

John T. Young and Gary Chatters assisted in the use and operation of McIDAS, Anthony Schreiner and Walter Knaack in processing, display, and analysis of data. David Suchman reviewed the manuscript. Final typing was done by Mrs. Vicki Epps. Support for the early stages of data processing was provided by National Science Foundation Grant 32496, the balance by NOAA Grant 04-3-158-61.

REFERENCES

Zipser, Edward J., 1969: The Role of Organized Unsaturated Convective Downdrafts in the Structure and Rapid Decay of an Equatorial Disturbance. J. Appl. Meteor., 8, pp. 799-814.

de la Moriniere, Terry, 1971: BOMEX Temporary Archive Description of Available Data. NOAA Technical Report EDS 10, Siver Spring, Maryland, 304 pp.

Martin, David W. and Dhirendra N. Sikdar, 1974: A Case Study of Atlantic Cloud Clusters. Part I: Morphology and Thermodynamic Structure, Submitted to Mon. Wea. Rev.

Jordan, C. L., 1958: Mean Soundings for the West Indies Area. J. Meteor., 15, pp. 91-97.

Oliver, Vincent J., and James F. W. Purdom, 1974: Mesoscale Convective Processes in the Tropics as Revealed by Satellite Imagery. Preprint Volume, Fifth Conference on Weather Forecasting and Analysis, Am. Meteor. Soc., Boston, pp. 61-62.

Purdom, James F.W., 1974: Satellite Imagery Applied to the Mesoscale Surface Analysis and Forecast. Preprint Volume, Fifth Conference of Weather Forecasting and Analysis, Am. Meteor. Soc., Boston pp. 63-68.

CAPTIONS

Figure 1 Evolution of the bubble cloud in pictures of the Applications Technology Satellite, photographed on the McIDAS TV display. Each picture has been individually enhanced to maximize cloud-background contrast. Circular white lines show the path followed by the cursor for computer measurement of areas inside the bubble cloud. A cross marks the position of the Oceanographer.

Figure 2 ATS-3 picture of 1426 GMT, 23 July, showing the larger scale setting of the bubble cloud. The bubble cloud, cloud band, and clear tongue are marked by arrows; certain landmarks and the ITCB are also identified.

Figure 3 Successive positions of the bubble cloud, mapped on a one degree by one degree grid of latitude and longitude. Greenwich times are marked next to each position.

Figure 4 Plots of area change (broken line) and divergence (solid line) for the bubble cloud.

Figure 5 Streamline pattern representing low level flow at 16 GMT, 23 July. Single line vectors represent low cloud motions averaged over the three ATS pictures at 1545, 1612, and 1637 GMT. Double line vectors represent 940 mb ship winds. Those between 7 and 8N are for the Oceanographer at observing times of 06, 09, 12, and 15 GMT; double line vectors between 10 and 11N are for the Mt. Mitchell at 15 and 18 GMT. The 16 GMT position of the bubble cloud is shown by a heavy dot-dash line. Stippling marks the coast of South America.

Figure 6 Hodographs of wind at the Oceanographer for three soundings: ahead of (23 14 57 GMT), within (9 0 2 GMT), and behind (14 59 56 GMT) the bubble cloud. Numbers along each hodograph give pressures in centibars. Vector displacements of the bubble center and cluster are indicated for comparison.

Figure 7 Time-height sections for the Oceanographer. The vertical coordinate is pressure in decibars. Vertical arrows along the bottom of each time section indicate soundings; the tops of these soundings are marked by small circles.

a. Temperature anomaly, in degrees K. Synoptic observations at three hourly intervals are plotted according to convention, except wind speed, for which each full barb represents 5 kn.

b. Relative humidity, in percent.

c. Equivalent potential temperature, in degrees K; with the 300 digit dropped.

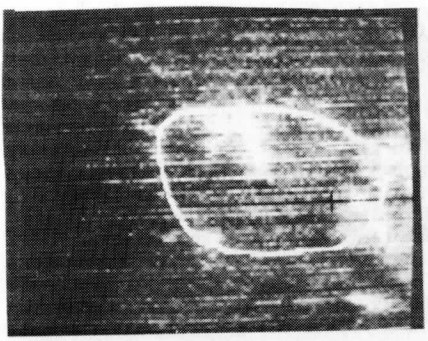

0955z

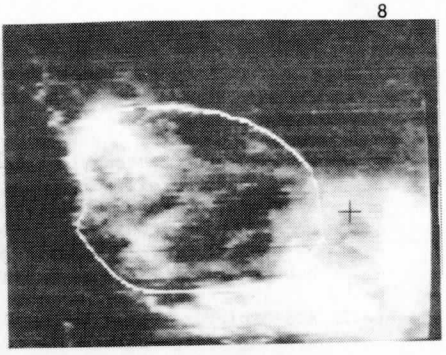

1400z

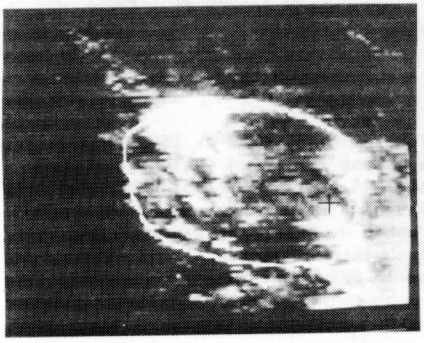

1112z

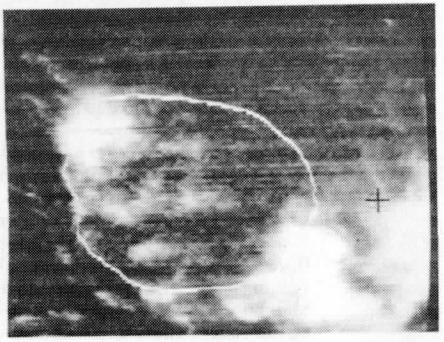

1518z

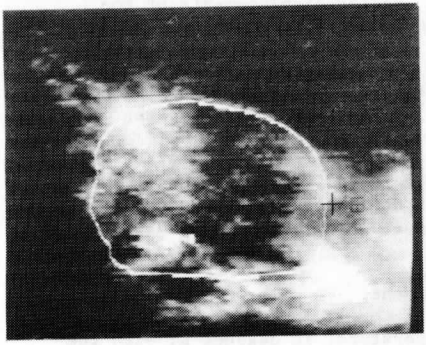

1242z

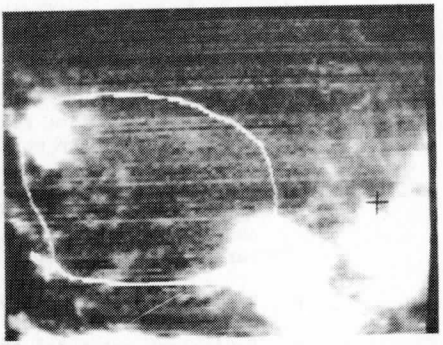

1637z

Figure 1.

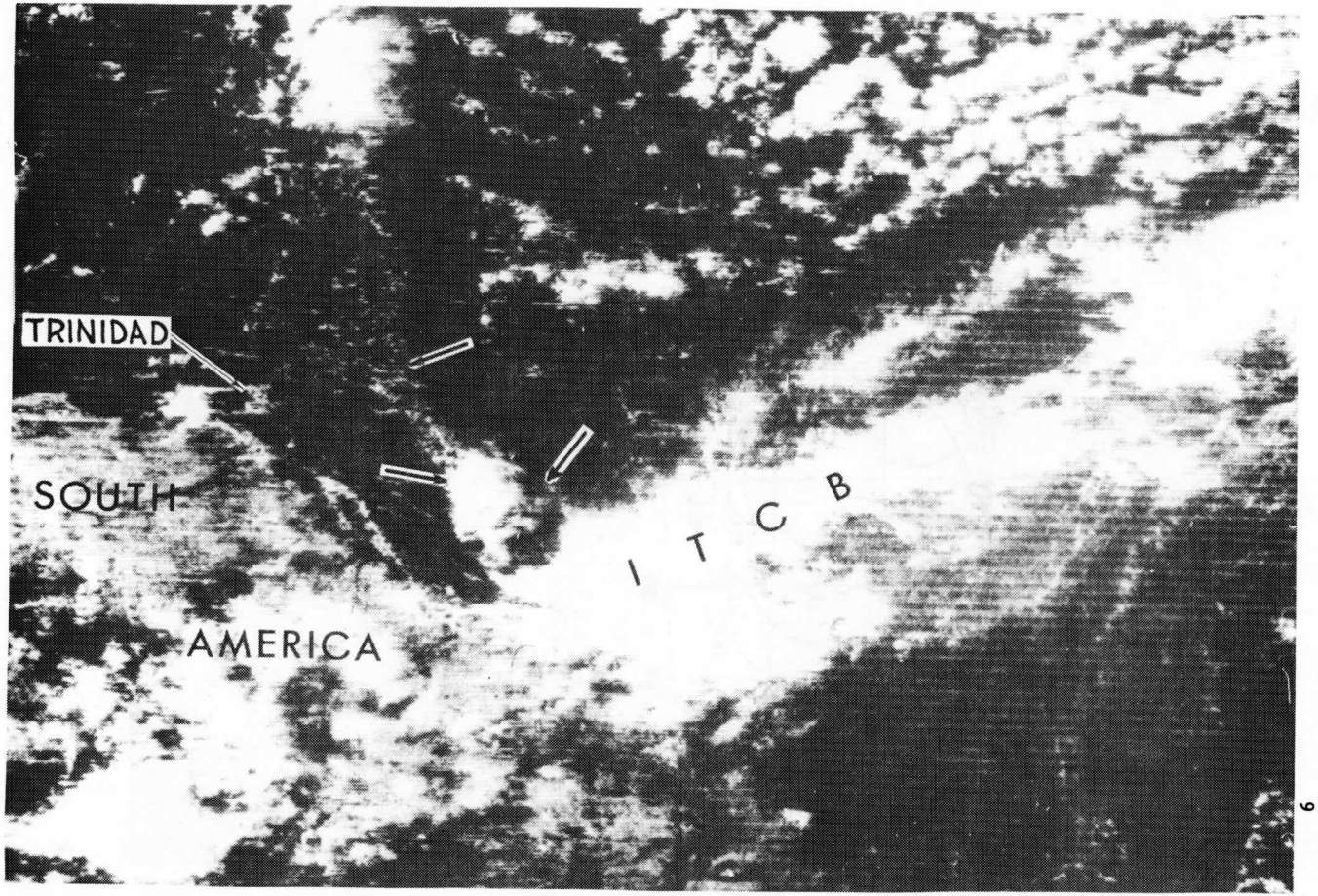

Figure 2.

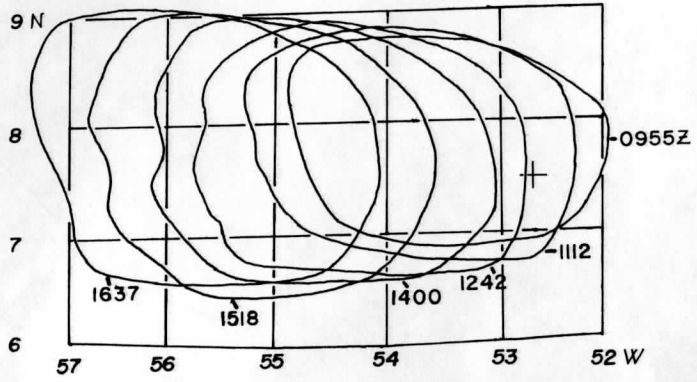

Figure 3.

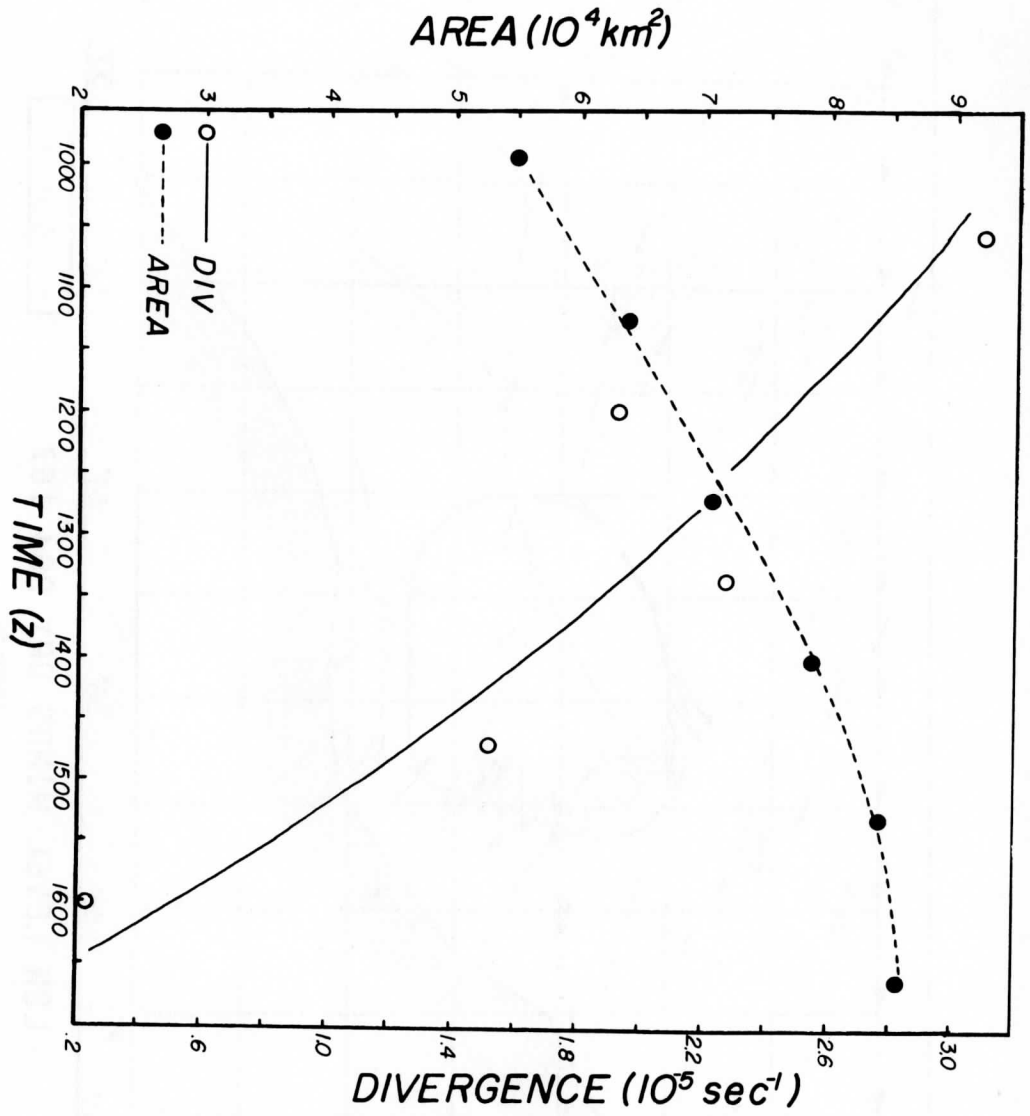
AREA (10^4km^2)
2
3
4
5
6
7
8
9
DIV
AREA
TIME (z)
1000
1100
1200
1300
1400
1500
1600
.2
.6
1.0
1.4
1.8
2.2
2.6
3.0
DIVERGENCE (10^{-5} sec^{-1})

Figure 4.

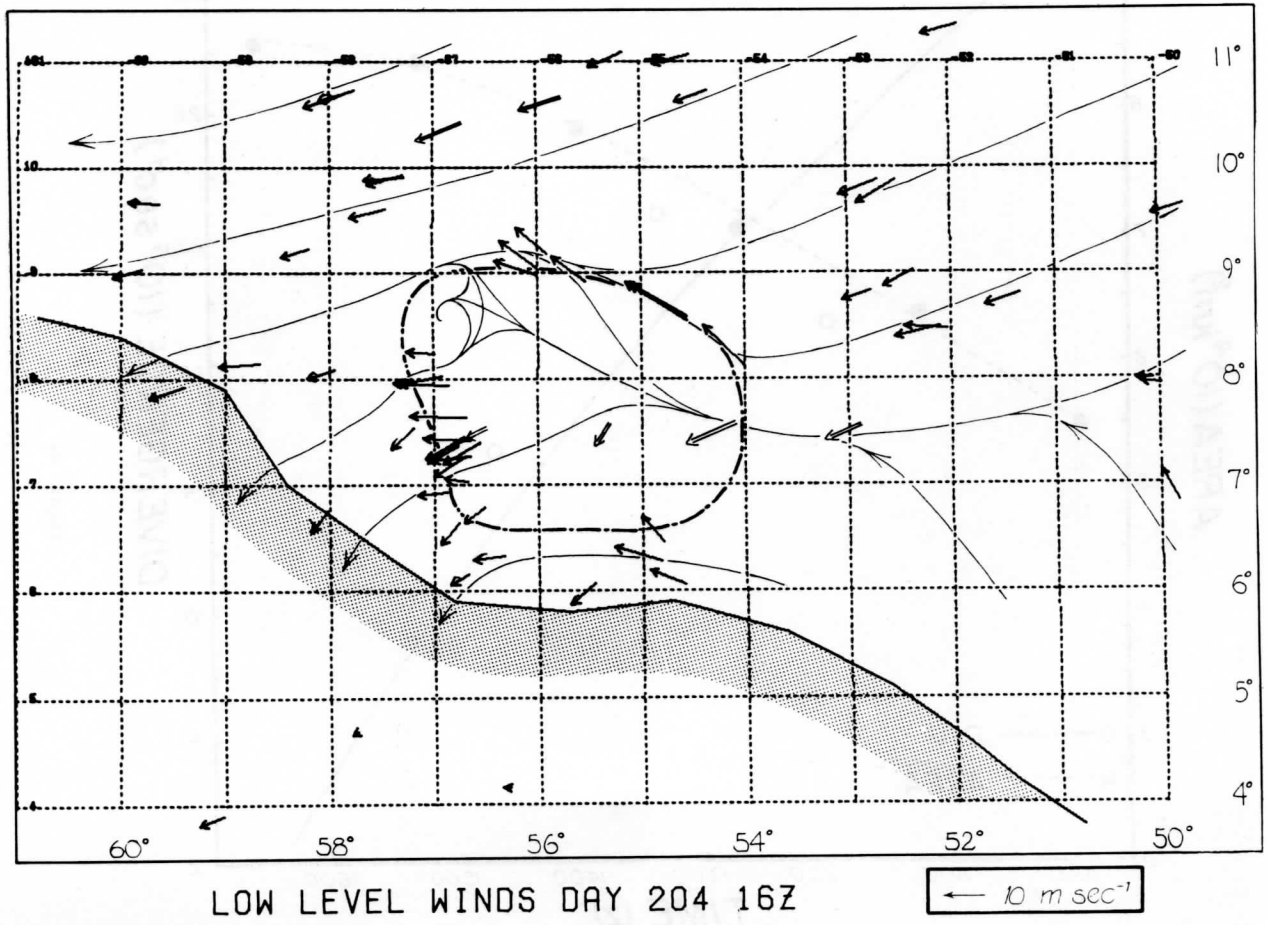
11°
10°
9°
8°
7°
6°
5°
4°
60°
58°
56°
54°
52°
50°
LOW LEVEL WINDS DAY 204 16Z
← 10 m sec⁻¹

Figure 5.

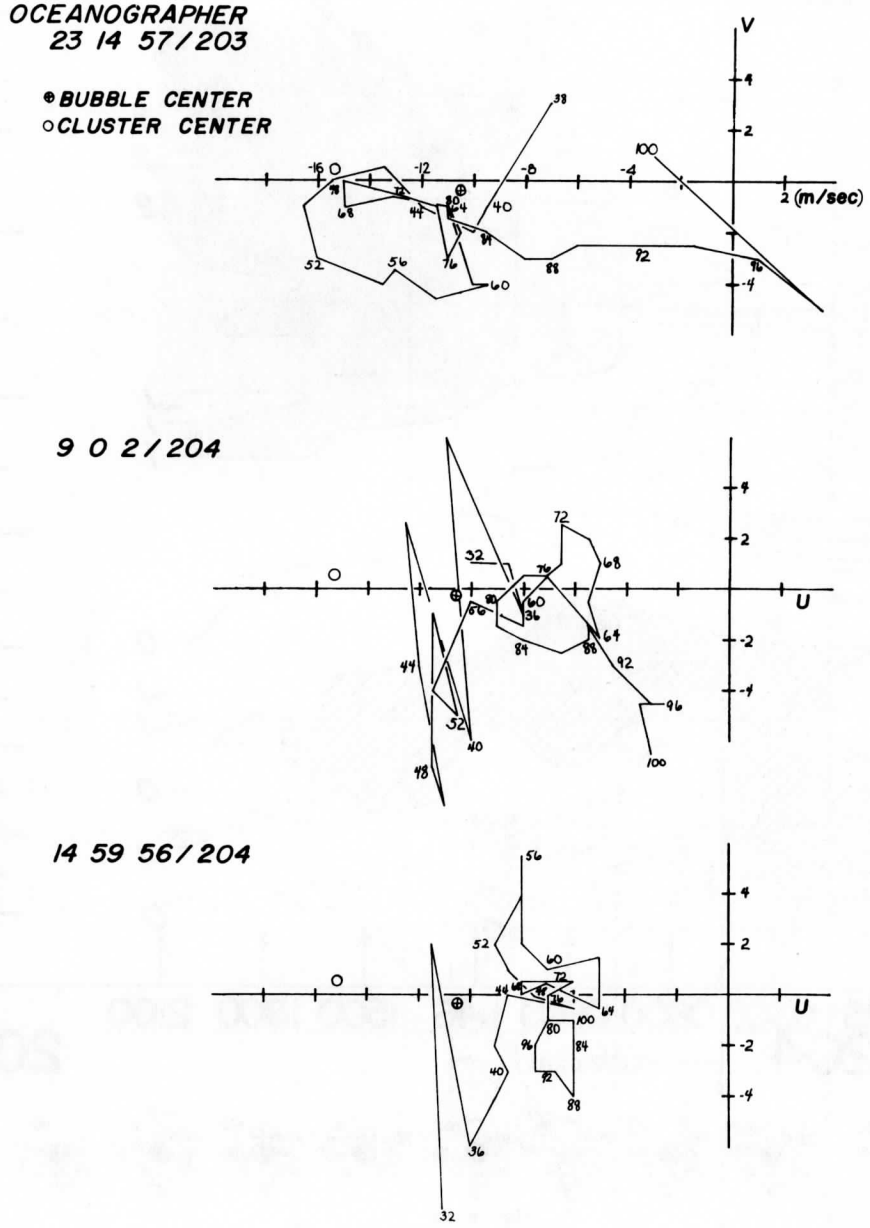
OCEANOGRAPHER
23 14 57/203
⊕ BUBBLE CENTER
○ CLUSTER CENTER
V
U
2 (m/sec)
9 0 2/204
14 59 56/204

Figure 6.

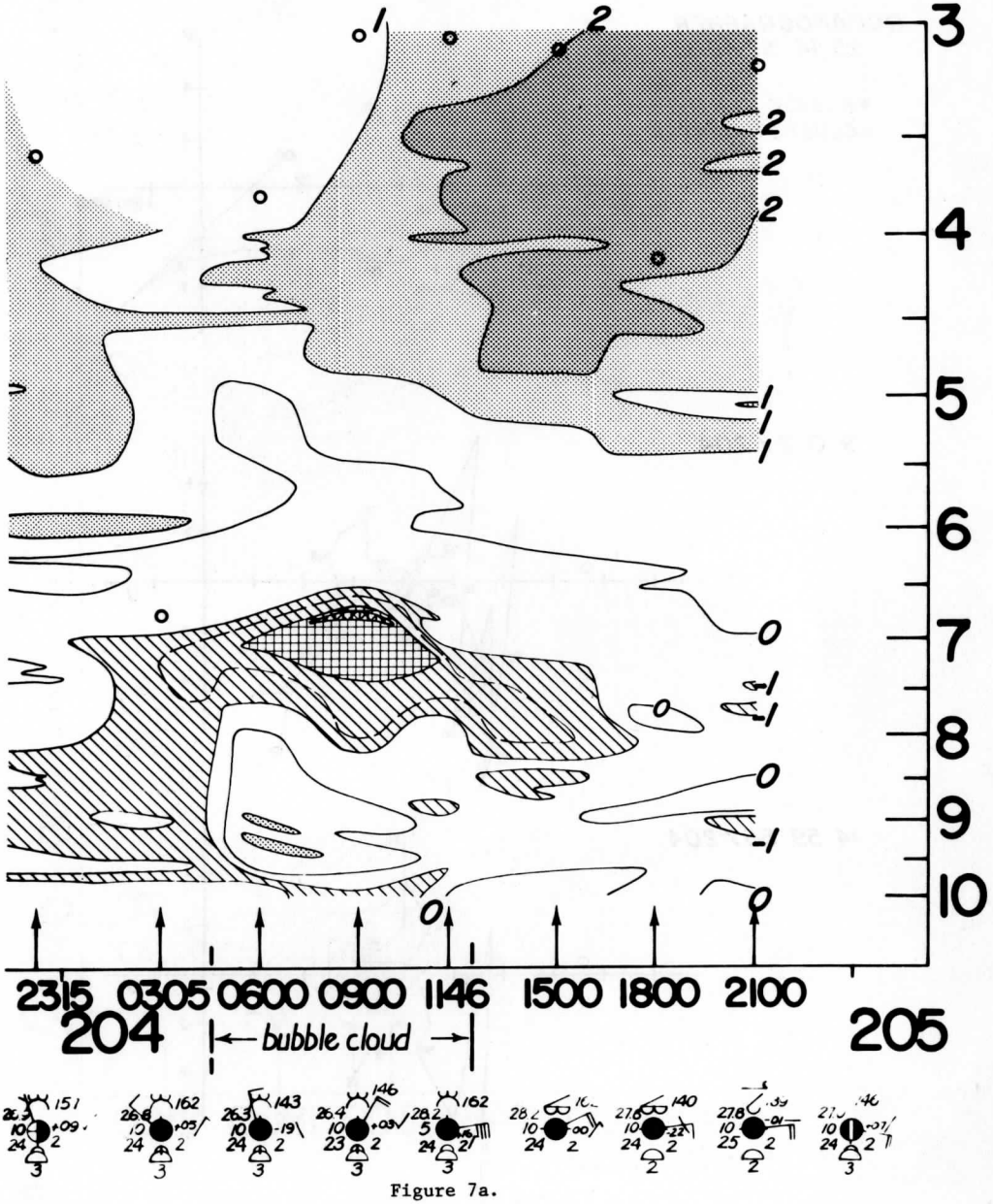
3
4
5
6
7
8
9
10
2315
0305
0600
0900
1146
1500
1800
2100
204
bubble cloud
205

Figure 7a.

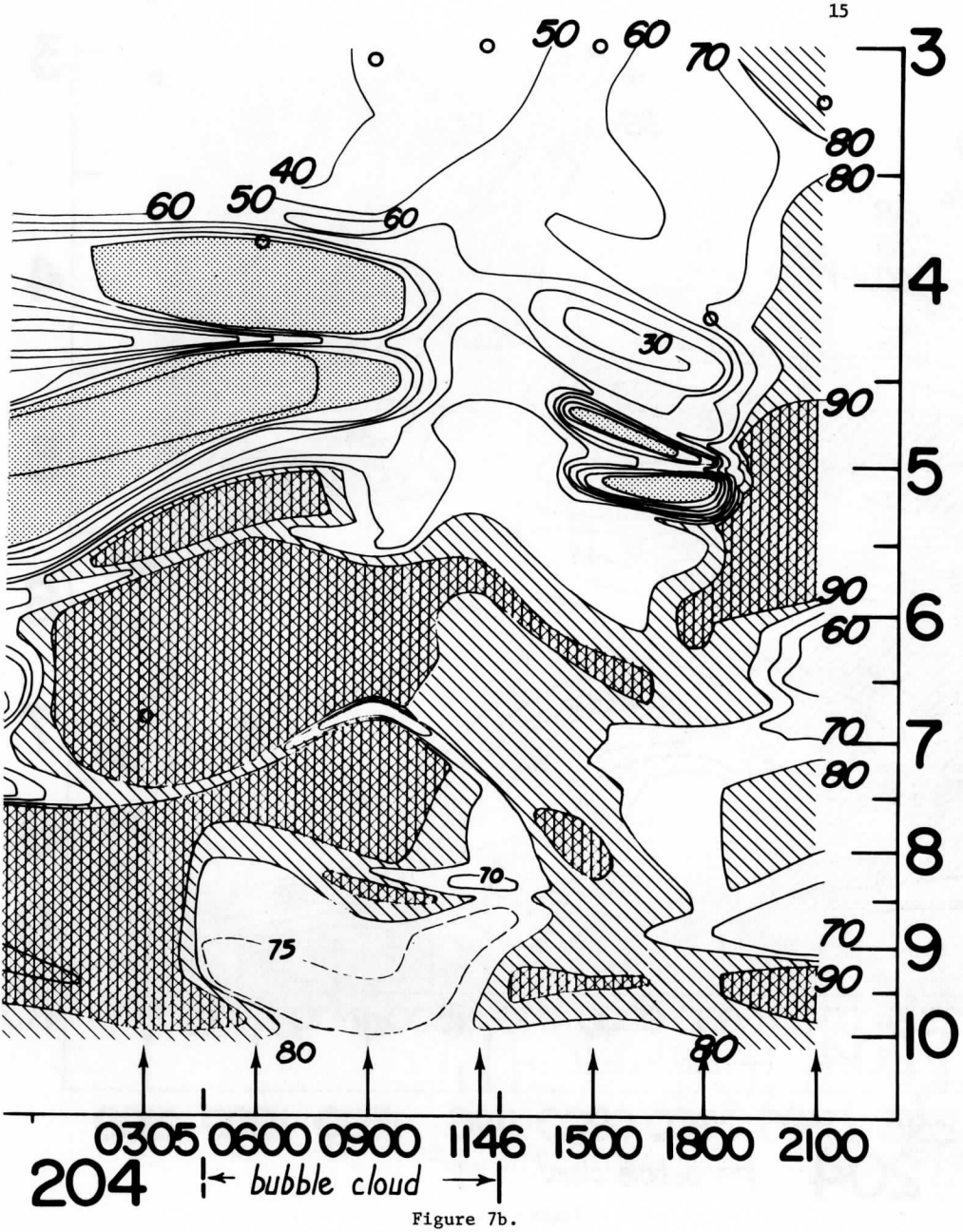
50
60
70
80
80
40
60
50
60
3
4
30
90
5
90
6
60
70
7
80
8
70
75
70
9
90
10
80
80
0305
0600
0900
1146
1500
1800
2100
204
bubble cloud

Figure 7b.

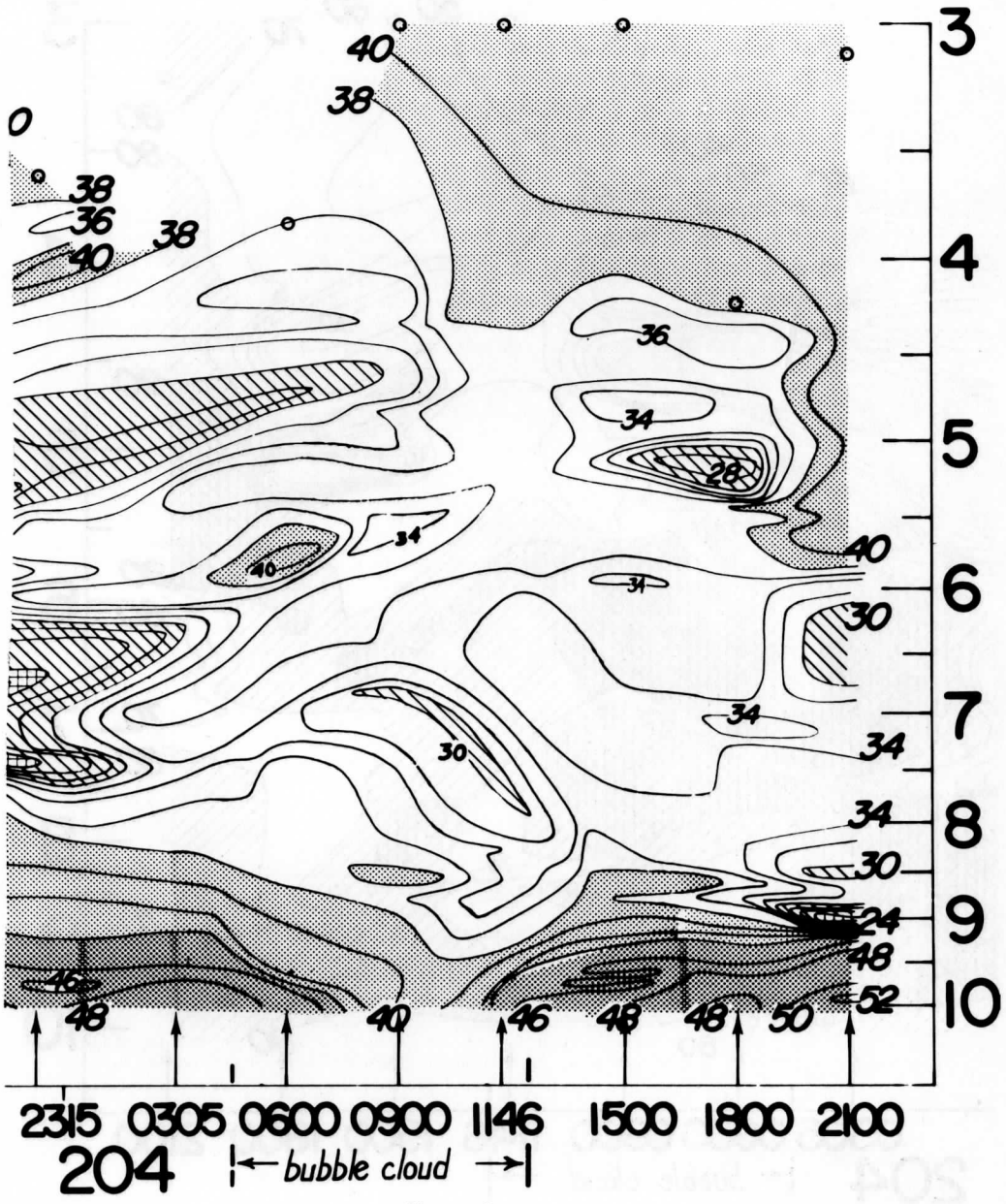
3
4
5
6
7
8
9
10
0
38
36
38
40
40
38
36
34
28
40
34
40
34
30
34
30
34
34
30
24
48
46
48
40
46
48
48
50
52
2315
0305
0600
0900
1146
1500
1800
2100
204
bubble cloud

Figure 7c.

A STUDY OF SATELLITE-DERIVED CLOUDINESS DURING THE INDIAN SUMMER MONSOON

Robert E. Peterson

ABSTRACT

Cloudiness data from video satellite pictures during three summer monsoons over India and the adjoining ocean areas are examined using monthly and ten-day mean cloudiness values for sixty 5° latitude by 10° longitude areas. Seasonal, inter-annual, and areal variations in monsoon onset and intensity are discussed for the strong 1967 monsoon, the weak 1968 monsoon, and the 1969 monsoon. Monthly mean cloudiness information from these years is then used to develop an estimation technique for monthly rainfall. Verification of the estimation technique is done using data from the strong 1970 monsoon season. Estimates for stations in central India verified in sixteen of 25 (64%) cases.

1. INTRODUCTION

The Indian summer monsoon has long been a topic of keen interest to meteorologists. In 1921 Simpson presented a comphehensive view of the monsoon in a lecture to the Royal Meteorological Society (Simpson, 1921). He said the primary cause of the monsoon circulation was the difference in temperature between land and sea areas. He explained that the relatively high temperatures which result over land as the sun moves toward summer solstice result in lower pressure and hence a flow of moist air from the ocean areas toward land.

Yin (1949) related the onset of the 1946 monsoon to changes in the upper air pattern. He noted monsoon onset was accompanied by a westward shift in a low latitude trough at the 8 km level from its winter position near 85°E to a summer position near 75°E. From this he inferred monsoon onset occurs later in India than in Burma due to India's location to the west of the wintertime position of the trough. Onset is delayed over India until the trough shifts to the west over the Indian subcontinent.

Flohn in two papers (Flohn, 1957 and 1964) discussed the relationship between the Tibetan plateau and the tropical easterly jet. He found seasonal heating on the plateau results in formation of a thermal anticyclone, forcing the westerlies to the north and creating a thermal gradient which is conducive to the formation of the easterly jet.

Recently, reports of drought and food shortages caused by rainfall deficiencies have focused attention on the need for a better understanding of the monsoon. For example, in a presentation of five year running

means of the percentage change in seasonal rainfall for stations in northwest India and the Sudan during the period 1943 to 1971, Gribbin (1973) indicates a substantial decline in rainfall from 1956 through 1971. The impact of such a trend upon agriculture is quite obvious.

Presently, the increasing availability of satellite data is steadily providing new tools for monsoon study. Satellite systems are rapidly increasing in number, resolution, and type of data. In addition to video cloudiness information as used in this study, possibilities such as vertical temperature profiles and wind information from satellites will greatly increase the amount of data available, especially over the vast ocean areas included in the southwest monsoon circulation.

Study of the climatological distribution of cloudiness has been greatly aided by the advent of meteorological satellite data. Dittberner (1969) used low resolution radiation data from Tiros IV to provide information on albedo and long wave outgoing radiation over the area of the Indian summer monsoon during the years 1963 through 1965. He also developed an intensity index for the monsoon. Sadler (1969) compiled monthly mean cloudiness for the area from 30°N to 30°S around the entire globe during the years 1965 and 1966. The cloudiness values were taken from operational nephanalyses prepared from Tiros X, ESSA 1, and ESSA 3. A different type of presentation was used by Miller and Feddes (1971). They employed automated methods to produce charts of mean monthly brightness as observed from video satellite data over the entire globe during 1967 through 1970. This analysis of brightness, instead of areal cloud cover, must be used with extreme care over desert and other areas where the earth's surface is bright and may be falsely interpreted as cloudiness on the mean brightness charts. Automated methods for deducing actual cloudiness from satellite data have been developed which attempt to eliminate this deficiency (See, for example, Collins and Coburn, 1971).

This study, in addition to presenting monthly mean satellite-derived cloud cover, investigates the inter-annual and seasonal variations in the cloudiness over India and the Indian Ocean during the summer monsoon seasons of 1967 through 1969. A technique for estimation of monthly rainfall from the mean monthly cloudiness over the Indian subcontinent is also presented.

2. SATELLITE DATA ACQUISITION

The satellite data used in this study were analyzed for the total areal cloud cover in sixty 5° latitude by 10° longitude areas over India, the Arabian Sea, the Bay of Bengal and the Indian Ocean between 30°N and 30°S latitude and 50°E and 100°E longitude as shown in Figure 1. The analysis for each of the sixty areas covers the period of the south-west monsoon (May - September) for the years 1967 through 1969.

Satellite Data Used in the Analysis

Daily mosaics of cloudiness presented on a mercator projection over the tropics were used for analysis. These mosaics were produced once a day from the video data output of ESSA 3 through ESSA 9 by the National Environmental Satellite Service. A complete list of the satellites used is presented in Table 1. The local time of the data from these satellites centers is the early afternoon.

TABLE 1

SATELLITES USED FOR ANALYSIS

Dates	Satellites
1 May - 30 May 1967	ESSA 3
31 May - 14 September 1967	ESSA 5
15 September - 30 September 1967	ESSA 3
1 May - 8 August 1968	ESSA 5
9 August - 12 August 1968	ESSA 3
13 August - 3 September 1968	ESSA 5
4 September - 30 September 1968	ESSA 7
1 May - 30 September 1969	ESSA 9

Measurement Methods

The cloud analysis was completed by dividing each 5° latitude by 10° longitude area into small sections, each containing two percent of the 5° by 10° area. The total areal cloud cover was then determined by estimating the number of these smaller areas which were cloud covered.

The initial analysis was carried out by three analysts working independently. Each completed one of the three years used in the study. The values of areal cloud cover were compiled by the author into latitude versus time charts for each ten degree longitude sector. Even after a very coarse analysis of these charts a bias toward excessively low values during August 1967 and all of 1968 was suspected based upon a comparison of the three years. A reanalysis of several randomly chosen days during these time periods by the author verified the bias. Complete reanalysis was therefore undertaken by the author for August 1967 and all of 1968. To assure consistency within the final data set a

random reanalysis of several days during each month was performed. Mean differences between the reanalysis for these random days and the final data set were near zero, indicating no significant bias. Root-mean-square differences ranged from 5 to 8 percent.

This range of RMS differences is small in comparison with that obtained by Young (1967) when he tested the ability of ten qualified weather observers at the Environmental Technical Applications Center to estimate the amount of an area covered by torn pieces of paper which simulated varying cloud shapes, sizes, and patterns. The RMS error range on Young's test was 7.5 to 30.0 percent, with largest errors occurring when the estimate was for a large number of very small torn pieces.

Young's test, since it produced a large error range, indicates the need for careful training of analysts who make areal cloud coverage estimates. Trained analysts should produce a much smaller error range on similar tests.

Data Limitations

Several limitations which are inherent in the data of this study must be understood to properly interpret the results of this work.

Only one satellite observation is available per day. The cloudiness at that observation time is assumed to be representative of the pattern of cloudiness for the entire day. Since the time of observation changes whenever observations shift from one satellite to another, it is reasonable to expect a change in the estimated daily cloudiness when a new satellite is introduced. All satellites used in this study view the India area during the local early afternoon (1200-1530 LST). The change in the areal cloud cover from one observation time to another during the early afternoon is not considered to be significant during the monsoon season.

Another factor within the satellite data which may influence the cloudiness analysis is variation in the brightness of the data. Schwalb and Gross (1969) describe brightness variations which occur during the life of each satellite. Variations also occur from one satellite to another, as well as within the data due to sun glint, bright background areas, etc. The trained analyst can eliminate these variations successfully by searching for brightness patterns which are identifiable as clouds. His analysis should therefore be superior to any technique which merely considers the observed brightness of an area for the determination of cloudiness.

One other limitation in the data set is the size of the basic analysis area. The 5° latitude by 10° longitude analysis areas are large (approximately 180,000 sq. nm.). Consequently, variations in small cloudiness patterns may not be resolved. The size is adequate, however, to depict large scale changes in cloudiness which occur during the Indian summer monsoon as discussed in the following section.

The product of the satellite data analysis as described above is a set of areal cloud cover values for each of the sixty areas depicted in Figure 1. The values for each area consist of three time series covering the months May through September for the years 1967 through 1969. The 180 time series were carefully intercompared to insure consistency. It is assumed that the one satellite observation per day used to produce the cloudiness estimates is representative of the cloudiness for the entire day. It is further assumed that changes of a few hours in the time of the observations used for analysis as observations shift from one satellite to another do not introduce significant changes in the cloudiness estimates.

3. CLIMATOLOGICAL CONDITIONS

Several investigations were undertaken following the analysis of the satellite data as described in the previous section. An analysis of mean monthly cloudiness was completed, isopleths of cloudiness in time versus latitude were analyzed for each 10 degree longitude sector, mean monthly cloudiness was compared to rainfall data, and an autocorrelation analysis was carried out on the data set.

The analysis of the autocorrelation of the data time series was carried out in view of several recent publications indicating periodicities in data similar to that of this study. (See, for example, Young and Sikdar, 1973 and Sikdar et al., 1972.) The autocorrelation calculations were done for each year 1967 through 1969, and for all sixty areas depicted in Figure 1. The results were then examined for characteristics recognizable in each of the three years which would imply similar periodicities in several adjacent analysis areas. It was expected that once such characteristics were found, a cross correlation at various lags between these areas would provide information on the movement of cloud systems. For example, it was hoped the movement of easterly waves and other cloudiness patterns through successive cloud analysis areas could be detected in this manner.

Other than the high persistence which was noted over the Indian subcontinent and adjoining areas, no significant inter-area similarities were found. In particular, no lags could be identified which consistently showed coefficients higher than expected values over several analysis areas. Consequently this portion of the investigation was terminated.

Monthly Mean Cloudiness

Cloudiness information from ground based observations can be analyzed in great detail over land areas having a high station density. The analysis rapidly becomes difficult, however, as station density and distribution fall below optimum levels. Analysis in ocean areas is most difficult due to the very sparse distribution of ship observations. In direct contrast to surface based cloud analysis is the analysis of satellite-derived cloudiness where the simultaneous observation of land and sea areas occurs at the same resolution. Figures 2 through 6 present the mean satellite-derived areal cloud cover for the months May through September during the years 1967 through 1969.

Miller and Feddes (1971) present satellite-derived mean brightness information for the period 1967 through 1970. Their analysis yields patterns which are somewhat similar to those of this study. However, conversion from area mean brightness to areal cloud cover is not easily done due to the varying brightness of cloud tops, the substantial brightness of certain surface areas, and the brightness variations introduced by different satellite sensors themselves. Consequently, the percentage cloud cover estimates as used in this study are more effective representations of total cloudiness.

Several features are noteworthy in Figures 2 through 6. Sizeable changes occur in the area covered by less than 10% cloudiness and in that covered by greater than 50% cloudiness as the season progresses. A double-banded maximum of cloudiness is present through all five months, while a distinct band of minimum cloudiness is present in the Southern Hemisphere.

In May the area containing more than 50% cloud coverage is restricted to the extreme northeast portion of the analysis area. During monsoon development (June map) the area advances southwestward. By July the monsoon cloudiness has increased to its maximum areal extent. The area with cloudiness in excess of 50% covers the eastern portions of the Arabian Sea, the Bay of Bengal and all but the extreme northwest portion of the Indian subcontinent. Associated with this strong southwestward advance of the maximum cloudiness area is the northwestward retreat of the area of minimum cloudiness. The area possessing less than 10% areal coverage, while covering a large portion of the Indian subcontinent and Arabian Sea during May, retreats during June to its most northwesterly location in July. The increased monsoon cloudiness over the subcontinent in July results in a very strong gradient in cloudiness across the northern portion of the Arabian Sea which persists on the August chart. The strong gradient is related to the fact that in the northwest the low level flow generally has a dry trajectory. Trewartha

(1961) explains the lack of precipitation in the Rajastan Desert area, where minimum cloudiness is present, by noting this region is dominated by a stable anticyclone aloft. Any moist flow from the Arabian Sea at low levels is capped by the anticyclone aloft. It is only to the south of this stable anticyclonic circulation that significant rainfall may develop. In view of this reasoning, the strong gradient in mean cloudiness should indicate the edge of the anticyclonic circulation aloft.

During August maximum cloudiness retreats slightly northward over southernmost India, while it progresses southward over Sumatra in the east. The retreat along 5-10°N actually results in an east-west band of minimum cloudiness with lowest values in the Bay of Bengal near 7°N. This minimum is noted by Nene (1971) during both 1968 and 1969. The September chart depicts the retreat of the monsoon as the maximum and minimum cloudiness areas begin a return toward their May locations.

Two distinct bands of regional maximum cloudiness are evident throughout the entire monsoon season. In May they are located near the equator with a separation near 85°E. The more meridional orientation of the eastern band in May indicates the beginning of flow into the eastern portion of the Bay of Bengal at this time. Farther to the west the zonal orientation is more typical of the type of pattern noted within the intertropical convergence.

During both June and July the eastern maximum remains relatively fixed in location, particularly at its southern end. The western maximum, however, rotates to a northeast-southwest orientation as southwesterly circulation develops over the Indian subcontinent. By July it extends from 5°S, 50°E through the central portions of the Indian subcontinent and on to 30°N, 100°E.

The August chart indicates the westward extension along the equator to 50°E of the eastern maximum which during May through July extended only to 85°E. The maximum associated with monsoon penetration into the subcontinent exists only in the north where it is maintained by continued southwesterly flow into that region. In September both maxima move southward and decrease in intensity as the monsoon retreats.

The area of minimum cloudiness in the Bay of Bengal during August takes on a new perspective in view of the above discussion. In the vicinity of the minimum, values of cloudiness change by only 13% through the five months. The minimum in August is emphasized by the bands of maximum cloudiness to the north and south. It is not completely the result of a large decrease in cloudiness over the Bay itself.

Throughout the entire five month period a relative minimum of cloudiness associated with subsidence within the Southern Hemisphere subtropical high extends from east to west along 15-20°S. Little north-south motion of this feature occurs.

The monthly mean cloudiness charts presented by Sadler (1969) for the years 1965 and 1966 generally agree with the features discussed above. There is one noteworthy exception. His analysis of July two-year mean cloudiness depicts a minimum band of cloudiness extending from 10°N, 50°E across the equator near 80°E then on to 8°S, 100°E, with no significant minimum band of cloudiness in the Southern Hemisphere as seen in Figure 4. This feature in Sadler's analysis is an anomaly which appears because only two years were averaged. Only the July 1965 cloudiness exhibits such a minimum. July 1966, the other year presented by Sadler, does not show a similar feature. Neither do any of the years studied in this work (1967 through 1969). Dittberner (1969) in his study of the 1963 through 1965 monsoons states that the 1965 monsoon was very weak. His analysis of mean albedo values confirms the minimum in July 1965, but does not show it in 1963 or 1964.

Isopleths of Cloudiness - Mean Values

Figure 7 presents three year mean isopleths of cloudiness for the three 10° longitude sectors between 60° and 90°E. The charts were prepared by computing ten-day mean cloudiness values and then averaging to produce the three year mean within each 5° latitude by 10° longitude area.

The 60-70°E longitude sector consists completely of ocean south of 25°N. Monsoon onset and withdrawal here are relatively gradual. Note the systematic northward movement of the 20% isopleth to 29°N by the end of July, followed immediately by slow southward movement. Northward movement of the latitude of maximum cloudiness from the equator in May to 7°N in early June is very gradual also. A division in the maximum band then occurs with one maximum returning to the equator and another strong maximum moving to 18°N. The northerly maximum remains near 18°N until middle September when it ends abruptly.

Within the 70-80°E sector monsoon onset is more rapid. The normal onset times expressed by Das (1968) are depicted as a double broken line from 4 to 24 June. This onset line lies approximately parallel to the 20% isopleth and is in the area of strongest gradient in cloudiness. In this sector, as well as in the 60-70°E sector, a band of maximum cloudiness exists near the equator in early May. It expands rapidly northward to 12°N during the first half of June and then continues to progress more gradually to 20°N by early August. A secondary maximum develops on the equator in middle August. As this secondary maximum

moves southward during September the maximum cloudiness in the north rapidly disappears.

The onset curve presented by Das (1968) in the 80-90°E sector bears little relationship to the isopleths of cloudiness. Cloudiness in this sector increases almost simultaneously at all latitudes north of 12°N. The maximum cloudiness band which exists just south of the equator in early May does not progress northward as in the other two sectors. Instead it remains near the equator through the entire season. It does show intensification during August as in the 70-80°E sector. Just to the north of the equator the Bay of Bengal minimum discussed earlier appears in late July and is evident to the north of the intensification in the equatorial maximum.

Isopleths of Cloudiness - Individual Years

To depict inter-annual changes in the monsoon, isopleths of cloudiness for the 70-80°E longitude sector are presented in Figure 8 for each of the years 1967 through 1969. Monsoon onset and withdrawal in each year are accompanied by a northward and then southward movement of the latitude at which maximum cloudiness occurs. Withdrawal of the monsoon is marked in each year by an increase in cloudiness on the equator just prior to the southward movement of the band of maximum cloudiness.

Since the normal dates of monsoon onset as presented by Das (1968) for this longitude sector appear to be approximately parallel to the 20% isopleth in Figure 7, location of the 20% isopleth relative to the normal onset curve will be used to describe the timeliness of monsoon onset.

Onset in 1967 was normal near 12°N, but progressed northward much more rapidly than normal, reaching 28°N ten days early. This is directly in contrast to 1968, when onset was early near 12°N, but was delayed by approximately 8 days in reaching 28°N. Earliest onset near 12°N occurred in 1969, but northward progress was extremely slow resulting in the latest arrival at 28°N.

The northward progress of the maximum cloudiness band occurred in a stepwise fashion in every one of the three years studied. In 1968 and 1969 the cloudiness maximum completed its first northward progression by early June while it was delayed until late June in 1967. During 1968 and 1969 cloudiness was concentrated in a narrow band near the maximum. Consequently, cloudiness values were low in the northern latitudes. The northern latitudes in 1967, however, had significant cloudiness due to the broad character of the maximum cloudiness band.

The second northward advance of the maximum cloudiness band occurred during middle to late July in all three years. The motion was much less distinct than the first. During 1967 the maximum maintained its most northerly location longer than in the other years. Significant southward motion of the maximum cloudiness occurred in 1968 and 1969 during late August and early September. In 1967 it did not begin southward movement until late September. One must conclude from the above discussion that the 1967 monsoon was the strongest of the three years studied, a conclusion which is reinforced in the following section.

The occurrence of an area of maximum cloudiness near the equator during August or September is typical of the start of monsoon withdrawal. As noted above, the 1967 withdrawal was late. The equatorial maximum began to appear during middle August and reached maximum strength in early September. Southward motion of the maximum cloudiness band began shortly after the equatorial maximum reached greatest intensity. Similar conditions took place in 1968 and 1969. The dates on which the equatorial maximum reached greatest intensity occurred during middle August, however.

Mean Cloudiness and Rainfall

Frequently the question of whether a given monsoon is "good" or "bad" is asked. This question in general refers to the adequacy of the rainfall received for agricultural purposes. The following discussion concentrates on west central India and intercompares the ten-day mean cloudiness and monthly cumulative rainfall for the years 1967 through 1970 to illustrate the relative effectiveness of the four monsoons.

Figure 9 presents ten-day mean cloudiness and monthly cumulative rainfall over the area 10-25°N, 70-80°E for the four years 1967 through 1970. A description of the source of the rainfall data is contained in Section 4.

A significant deficit in rainfall is noted during the 1968 season, while excesses were experienced in 1967 and 1970. A normal amount of rainfall occurred in 1969. These rainfall differences are very much related to the variations in ten-day mean cloudiness from year to year.

The contrast between the cloudiness in 1967 and 1970 is significant. While both years produced precipitation in excess of the ten year mean, there is a significant difference in the time at which the excess occurred. Cloudiness values in 1970 rose above the three year mean very early in the season and remained greater than the long term mean with the exception of three weeks at the end of July through early August. The maximum value

of the cloudiness never reached the high value of 1967, however. In contrast, the 1967 cloudiness increased abruptly during early June, reached a very high level during July, and ended the season near the three year mean. The rainfall curves closely correspond to the cloudiness. Largest increases over the ten year mean precipitation occurred in July during 1967 when the amount of cloudiness was very large. In 1970 it was during May, June, and September that large increases over the ten year mean rainfall occurred. These are the months when cloudiness was significantly above the three year mean.

The differences between 1969 (when rainfall was nearly equal to the ten year mean) and 1968 (when only 80% of the ten year mean occurred) are not immediately obvious. Inspection of the cloudiness curves indicates that during 1968 the ten-day mean cloudiness was below the long term mean nine times and above the long term mean only twice. The corresponding values for 1969 are seven times below and six times above. The greater amount of cloudiness during 1969 corresponds to the larger amount of rainfall in that year.

The above discussion points out that over the area 10-25°N, 70-80°E the monthly rainfall expressed as a percentage of the ten year mean rainfall appears to be related to mean cloudiness values. Bedi and Sikka (1971) indicate a good comparison between changes in six-day mean brightness from satellite data and six-day mean rainfall for several areas over the Indian subcontinent. It is this reasonably direct relationship anticipated from comparison of mean cloudiness and rainfall curves which encouraged the investigation of the following section.

The results of this section indicate several interesting climatological features of the summer monsoon over India. The maps of monthly mean cloudiness indicate two distinct cloudiness maxima in all of the months studied. One of these maxima extends across the Bay of Bengal while the other crosses the Indian subcontinent. The study of isopleths of cloudiness in time versus latitude indicates that within the 70-80°E longitude sector the northward advance of the 20% isopleth coincides with the normal northward advance of the monsoon as presented by Das (1968). Within the 80-90°E longitude sector the isopleths bear little relationship to the normal onset curve presented by Das. A feature which appears in both the 70-80°E and 80-90°E sectors is a strong intensification in cloudiness near the equator during middle August. This intensification occurs just prior to the beginning of monsoon withdrawal. The isopleth analysis for individual years within the 70-80°E longitude sector shows a stepwise northward movement of the latitude of maximum cloudiness during the monsoon onset. The comparison of ten-day mean cloudiness and cumulative monthly rainfall over west central India provides a ranking of the relative effectiveness of the monsoons from 1967 through 1970 for producing rainfall, as

well as a strong indication of a rather direct relationship between cloudiness and rainfall. The 1967 and 1970 monsoons produced amounts of rainfall significantly above the ten year mean. The 1969 monsoon produced an amount nearly equal to the ten year mean, while in 1968 only 80% of the ten year mean was realized.

4. RAINFALL - CLOUDINESS RELATIONSHIPS

A linear regression model was used to investigate the relationship between the monthly mean cloudiness and the monthly rainfall, a relationship anticipated due to comparison of mean cloudiness and rainfall as in Section 3. The linear model produced correlation coefficients in excess of 0.7 in areas where the strong relationship was expected. Monthly precipitation estimates are easily generated from monthly mean values of satellite-derived cloudiness through the use of the regression.

Previous Rainfall - Cloudiness Relationships

Sadler (1969) indicated "crude agreement" between patterns in the long-term mean of February rainfall and a two year (1965-1966) average cloudiness for February over Africa. Gerrish (1970) demonstrated a correlation between the average cloud cover and the mean daily precipitation over the Florida area.

Barrett (1970) devised a method for estimating monthly rainfall using nephanalysis data prepared from satellite pictures. The method uses a rainfall coefficient which depends upon the amount and type of cloudiness to produce the rainfall estimate. A test of the method was conducted over Australia and the East Indies. The method is general, however, and was designed for use in areas other than where it was devised. Follansbee (1973) used Barrett's method to estimate daily rainfall by including only three cloud types and obtaining the cloud amount and type directly from satellite data. A test of the method over the southern United States resulted in less than a fifteen percent average daily difference between estimated and observed rainfall for the nine days of the test.

Davis et al. (1971) as reviewed by Martin and Scherer (1973) describe an estimation method for the total precipitation including snow over the Flathead River basin in western Montana. The technique consists of assigning the cloud pattern over the area to one of nine categories. A precipitation coefficient for each category gives the rainfall expected from that particular pattern. Martin and Scherer also review methods which utilize brightness statistics derived from satellite data to infer short term rainfall and rainfall rates.

Barrett's method requires a determination of cloud types and the amount of each type present. In the Davis method, classification of a cloudiness pattern is necessary to make the rainfall estimate. Within the areas influenced by the southwest monsoon, mean amount of cloudiness is expected to be a rather direct indicator of the rain-producing ability or strength of the monsoon. Consequently, in this study it was expected that a simpler relationship between cloudiness and rainfall might well exist, namely that high values of mean cloudiness should correspond directly to large values of rainfall. Therefore, since monthly rainfall amounts and monthly cloudiness averages were available, they were used to derive a monthly rainfall estimation method.

Rainfall Data

The rainfall data of this study is contained on a magnetic tape containing World Weather Records Data and available through the National Center for Atmospheric Research or the National Climatic Center, NOAA. Data were available for the stations depicted in Figure 10. A list of stations is contained in the Appendix. This rainfall information consists of monthly and yearly amounts of precipitation for each station. To convert the individual station information to areal statistics for each 5° latitude by 10° longitude cloud analysis area, the following procedure was adopted. First, the monthly rainfall amounts at each station were converted to a percentage of the station's ten year mean seasonal rainfall using equation (1).

$$P_{ij} = \frac{R_{ij}}{S_i} \times 100, \qquad (1)$$

where R_{ij} is the rainfall in centimeters which occurred at station i during month j, S_i is the ten year (1961-1970) mean seasonal (May - September) precipitation for station i, and P_{ij} is the monthly rainfall percentage for station i during month j. Following the above conversion, all stations within each 5° latitude by 10° longitude area were averaged to produce a representative value of the monthly rainfall percentage for the area using equation (2).

$$\overline{P_j} = \frac{1}{N} \sum_{i=1}^{N} P_{ij}, \qquad (2)$$

where N is the total number of stations in the area, P_{ij} is as defined in equation (1), and $\overline{P_j}$ is the area representation of the rainfall during month j as a percentage of the ten year mean seasonal rainfall.

Several factors influenced the adoption of the above method to represent area rainfall. The size of the area used for cloudiness

analysis (5° latitude by 10° longitude) is large. Each one therefore has within it a large spatial variation in the monthly rainfall. Expression of rainfall at each point as a percentage of a mean amount yields approximately normalized values which aid intercomparison of stations and produce representative values when several stations are averaged. The choice of ten year mean seasonal rainfall over mean monthly rainfall as the normalization factor was made because it presents several advantages. The relative contribution of each month to total monsoon precipitation is directly expressed, and cumulative information may be obtained by simply adding the monthly values. The range of monthly values using the seasonal mean for normalization rarely exceeds 50%, while it frequently exceeds 100% when monthly means are used for normalization. The smaller range of values is much more stable and more easily applied to the computations of this study.

The areal average rainfall percentage described above becomes more representative of the actual conditions over an area when more well-distributed stations are available. The region enclosed in heavy dark lines in Figure 10 has at least five well-distributed stations in each cloud analysis area. Hence, the rainfall percentages for the enclosed area should effectively represent the actual precipitation.

A monsoon rainfall summary is published yearly in the Indian Journal of Meteorology and Geophysics. The summary gives monthly rainfall data as a percentage of the monthly normal precipitation for each of the meteorological subdivisions of India. To assure that the rainfall information of this study is comparable to the published data, a computation of percentages in a manner yielding the type of values published was completed. Comparison of these computed values with the published data produced no significant discrepancies.

Generation of the Regression Model

In deriving a relationship between the monthly mean cloudiness and the percent of mean rainfall described above, a linear regression model was applied to every cloud analysis area for which rainfall information was available. Fifteen data points consisting of one point for each of the five months May through September during the years 1967 through 1969 were available for computation in each area. The resulting relationship is unique for each cloud analysis area. It uses the same regression line, however, to relate rainfall and cloudiness during all months.

The linear correlation coefficients which resulted from the regression are presented in Figure 11. The coefficients indicate an excellent correlation over continental areas, those having good station coverage. Even in several areas which have poor station

distribution or only a few stations the correlation is above 0.6, indicating a good relationship. The regression lines corresponding to each area with a correlation coefficient greater than 0.5 are presented in Figure 12. Note that the slope of the regression lines shows a sizable decrease from west to east and from north to south. The greater slope in the west and north indicates a larger contribution to total rainfall by convective activity which produces large amounts of rain at relatively low values of mean cloudiness.

Another noteworthy feature of the linear regression lines is the fact that the curves do not in general pass through the origin of the graphs. Those which indicate a value of rainfall when the mean cloudiness is zero lead one to believe the relationship is likely to be nonlinear with very small amounts of cloudiness. Nonlinearities are also likely with very large values of cloudiness since it is expected that increasing the cloudiness beyond some threshold value will result in a smaller increase in rainfall than in middle value ranges. The linear relationship is a first approximation. Its usefulness as a rainfall estimation technique is evaluated in the following section. A much larger data set than that of this study would be needed to identify the nature of the expected nonlinearities.

Test of the Regression

The regression equation for each area was tested by performing an analysis of the 1970 cloudiness (an independent population) for each of the eleven 5° latitude by 10° longitude areas having a linear correlation coefficient larger than 0.5 in the dependent data. See Figure 11 for the exact area. Estimates of monthly rainfall percentage were then obtained from the cloudiness values. These estimates were finally compared to the observed rainfall percentages.

Five estimates were made for each area, one for each of the months May through September. The root-mean-square differences from the observed values are presented in Figure 13. Note that the errors are smallest (7.5% or less) in the areas having the largest number and best distribution of station data for rainfall analysis. This is an expected result since areas which are not reasonably well covered by stations may undergo large cloudiness variations over portions where no rainfall data are available. For example, in the longitude sector 60-70°E few stations were available for rainfall analysis. The dependent data produced correlations greater than 0.75 in spite of this. However, errors in the 1970 estimates were larger here than in any of the other areas.

Figure 13 also contains the root-mean-square differences which resulted from using a ten year mean rainfall percentage for each

monthly estimate. The root-mean-square differences for these estimates are smaller than those of the estimation technique in only three of the eleven areas.

A verification for each of the five stations in the area 15-20°N, 70-80°E is presented in Table 2 to better illustrate the errors and method of this technique. In each case the estimate made using this method is compared to the estimate which would result from using the average monthly precipitation in centimeters at the station during the previous nine years. The RMS difference between the estimated and observed precipitation is 15.5 centimeters for the estimates produced by the linear regression model, and 19.5 centimeters for the estimates produced by the nine year average rainfall. Also, in 16 of 25 cases the monthly estimates produced by the regression model were above or below the nine year mean rainfall amount when the observed rainfall amount was above or below, respectively. Four of the five seasonal estimates obtained by summing the monthly amounts are correct using the same verification scheme. Figure 14 presents a scatter diagram of the data in Table 2 for the estimates derived from the regression model. The monthly estimates for individual stations are computed by multiplying the estimated monthly percentage for the area containing a station by the station's ten year mean seasonal rainfall amount.

The results of this section indicate a reasonably simple estimation technique for rainfall using satellite-derived cloudiness in the monsoon area may be feasible. The study also reinforces the general feeling that the effectiveness of the monsoon for producing rainfall may be easily evaluated qualitatively by examining several satellite photographs covering a period of time and noting the amount of cloudiness present relative to similar periods in which the rainfall amount is known.

The estimation technique discussed in this section was applied in September 1974 to the months May through August 1974 for the area 10-30°N, 70-80°E and the area 20-25°N, 80-100°E. The satellite data used for the estimation were from NOAA 3 which receives data near 0900 local time. This is a significant departure from the time of the data used to develop the estimation technique. The results of the monthly estimations indicated that the cumulative rainfall for May through August 1974 was below normal for all of the areas with the exception of 20-25°N, 90-100°E where above normal values were estimated. Although no specific rainfall information is available at this time, the reports in newspapers, etc. coming from India appear to verify the estimates.

TABLE 2

INDIVIDUAL STATION VERIFICATION DATA

FOR THE 15-20°N, 70-80°E AREA

	MAY		JUNE		JULY		AUGUST		SEPTEMBER		SEASON	
STATION	EST	OB	EST	OB	EST	OB	EST	OB	EST	OB	EST	OB
Bombay	15.0	2.9	48.6	94.3	54.0	54.9	60.3	73.0	46.4	31.1	224.3	256.2
	0.4		47.5		76.8		36.7		24.2		185.6	
Poona	4.4	4.8	14.2	8.4	15.7	13.3	17.6	8.0	13.5	3.9	65.4	38.4
	4.7		9.7		23.5		11.1		9.2		58.2	
Begampet	5.3	7.8	17.2	17.5	19.1	10.9	21.3	40.0	16.4	29.2	79.3	105.4
	2.8		8.0		20.6		11.9		20.8		64.1	
Goa	20.2	23.6	65.2	81.4	72.5	83.1	81.0	96.9	62.4	23.6	301.3	308.6
	7.0		78.5		101.1		38.3		28.3		253.2	
Belgaum	9.2	21.5	26.4	20.9	32.9	42.9	36.7	30.0	28.3	12.9	133.5	128.2
	12.4		12.2		49.6		31.0		11.0		116.2	

All values are given in centimeters of rainfall. The top numbers in the esimation columns are the values estimated by the technique presented in this study. The lower numbers represent the mean rainfall for the station during the previous nine years (1961-1969). Underlined cases are those in which the estimated rainfall amount using the technique of this study is in the same direction from the nine year average as the observed values.

5. SUMMARY

Satellite-derived cloudiness data for three monsoon seasons were analyzed in this study of the southwest monsoon over India. In addition to a climatological examination of the monsoon area, a method for estimating rainfall over the Indian subcontinent and surrounding land areas was suggested.

The monsoon seasons of 1967 through 1969 were used in discussing the climatology of the area. The cloudiness during the 1970 monsoon was partially analyzed for use as independent data in the rainfall estimation scheme. This partial analysis was therefore added to the climatology in Section 3. The analysis of Section 3 indicated that over central India the 1967 and 1970 monsoons were well developed, yielding a seasonal precipitation in excess of the ten year mean (1961-1970). The 1969 monsoon produced normal rainfall, while in 1968 only 80% of the ten year mean rainfall was observed.

The analysis of the monthly mean charts of cloudiness revealed two distinct areas with regional cloudiness maxima which appear in May and continue during each month of the monsoon season. One maximum area extends across the Bay of Bengal, the other across the Indian subcontinent. This double maximum agrees with the conclusion of Dittberner (1969) that the monsoon consists of two main activity centers.

The analysis of the relationship between mean cloudiness and rainfall in Section 4 demonstrates that a reasonably simple estimation technique for monsoon rainfall is possible. While the linear regression model used in this study is in all likelihood only a crude approximation to the actual relationship, it does demonstrate reasonable usefulness.

Several areas of further research are suggested by this study. These are primarily in the area of rainfall estimation. Inclusion of a larger dependent data sample would allow for consideration of a regression model which is nonlinear and would also allow development of a regression for each month as well as for each area. The rainfall estimate would be improved by decreasing the size of the individual areas. It is also expected that the relationship could be established on a much shorter time scale than a month. A six to ten day cloudiness average for estimation would make the results extremely useful as agricultural information for crop assessments.

Several other types of satellite data will allow for improvement of the estimation method. The use of data from a geosynchronous satellite over the monsoon region would produce a more representative daily cloudiness value than the once a day coverage of this study.

Inclusion of simultaneous infrared data which was not available during the 1967 through 1969 period would serve to further refine the method, since the height of cloud tops as well as the areal coverage could be used to characterize areas which are likely to produce significant precipitation.

Although many refinements in estimation techniques are needed, the concept of using such a method to do rapid analysis of monsoon rainfall for input to agricultural decisions presents several advantages over analysis of conventional station reports. The estimation technique uses continuous cloudiness fields to infer the amount of precipitation, which while "tuned" to station reports in its development, may actually better represent conditions over large areas than the point sampling done by individual stations. In addition, estimates from satellite data can be made quickly for very large regions by a facility receiving the satellite data. This fact greatly shortens the time between data collection and rainfall determination when compared to the collection and analysis of rainfall information from remote locations.

ACKNOWLEDGEMENTS

I desire to express my most sincere gratitude and appreciation to Dr. Eberhard W. Wahl for his support, guidance, and encouragement during the entire course of this research. I also wish to thank Dr. Wayne M. Wendland for his assistance in the preparation of this paper, and Dr. D. N. Sikdar who provided a portion of the data as well as the suggestion of the general area of this research. My gratitude must also be expressed to Dr. Kenneth G. Bauer for his advice during the final completion of this work.

Finally I must thank my wife, Linda, and children for the love, patience, and understanding provided through the duration of this study.

This research was partially supported by DOC/NOAA Grant 04-3-158-61.

REFERENCES

Barrett, E. C., 1970: The Estimation of Monthly Rainfall from Satellite Data. Mon. Wea. Rev., Vol. 98, 322-327.

Bedi, H. S. and D. R. Sikka, 1971: A Study of 6-Day Mean Satellite-Derived Brightness Patterns in Relation to Upper Air Circulation Features During the 1967 Southwest Monsoon Season. Indian J. Met. Geophys., Vol. 22, 299-304.

Collins, R. W., and A. R. Coburn, 1971: Application of Satellite Data to an Automated Nephanalysis and Forecasting Program. Automated Weather Support, AWS Technical Report 242, Air Weather Service (MAC), United States Air Force, Scott AFB, Illinois, 248-260.

Das, P. K., 1968: The Monsoons, National Book Trust, New Delhi, India.

Davis, P. A., E. J. Weigman, and S. M. Serebreny, 1971: Estimation of Precipitation Over Flathead Drainage Basin Using Meteorological Satellite Photographs. Final Report Contract 14-06-D-7047, Stanford Research Institute, Menlo Park, California.

Dittberner, Gerald J., 1969: A Study of the Indian Monsoon Using Satellite Measured Albedo and Long Wave Radiation. M. S. Thesis, Department of Meteorology, University of Wisconsin, Madison, Wisconsin.

Flohn, Hermann, 1957: Large Scale Aspects of the "Summer Monsoon" in South and East Asia. J. Met. Soc. Japan, Vol. 35, 180-186.

_____ 1964: Investigations on the Tropical Easterly Jet, Meteorologisches Institut Der Universitat, Bonn.

Follansbee, W., 1973: Estimation of Average Daily Rainfall from Satellite Cloud Photographs. NOAA Tech. Memo. NESS 44., National Environmental Satellite Service, NOAA, Washington, D.C.

Gerrish, Harold P., 1970: Satellite and Radar Analysis of Mesoscale Features in the Tropics. Final Report ECOM-0205-F. U. S. Army Electronics Command, Fort Monmouth, New Jersey.

Gribbin, John, 1973: Our Weather: A Link with the Planets?. New Scientist, Vol. 60, 893-895.

Martin, David W. and Wolfgang Scherer, 1973: Review of Satellite Rainfall Estimation Methods. BAMS, Vol. 54, 661-674.

Miller, Donald B. and Robert G. Feddes, 1971: Global Atlas of Relative Cloud Cover 1967-1970, U. S. Department of Commerce, National Environmental Satellite Service, NOAA, Washington, D.C.

Nene, Y. R., 1971: Some Features of Mean Clouding Over Bay of Bengal During July and August 1968 and 1969. Indian J. Met. Geophys., Vol. 22, 403-404.

Panofsky, Hans A. and Glenn W. Brier, 1968: Some Applications of Statistics to Meteorology, Pennsylvania State University, University Park, Pennsylvania.

Sadler, James C., 1969: Average Cloudiness in the Tropics, East-West Center Press, Honolulu, Hawaii.

Schwalb, Arthur and James Gross, 1969: Vidicon Data Limitations. ESSA Tech. Memo. NESCTM 17, U.S. Department of Commerce, Washington, D.C.

Sikdar, D. N., J. A. Young and V. E. Suomi, 1972: Time-Spectral Characteristics of Large-Scale Cloud Systems in the Tropical Pacific. JAS, Vol. 29, 229-239.

Simpson, G. C., 1921: The Southwest Monsoon. Quart. J. Royal Met. Soc., Vol. XLVII, 151-172.

Trewartha, Glenn T., 1961: The Earth's Problem Climates, The University of Wisconsin Press, Madison, Wisconsin.

Yin, Maung Tun, 1949: A Synoptic-Aerologic Study of the Onset of the Summer Monsoon Over India and Burma. J. of Met., Vol. 6, 393-400.

Young, John A. and D. N. Sikdar, 1973: A Filtered View of Fluctuating Cloud Patterns in the Tropical Pacific. JAS, Vol. 30, 393-407.

Young, Murray J., 1967: Variability of Estimating Total Cloud Cover From Satellite Pictures. JAM, Vol. 6, 573-579.

APPENDIX: LIST OF STATIONS USED FOR RAINFALL ANALYSIS

STATION	WMO NUMBER	LATITUDE	LONGITUDE
Agra	42261	27.2N	78.0E
Ahamabad	42647	23.0N	76.6E
Akola	42933	20.7N	77.0E
Allahabad	42475	25.5N	81.9E
Bangalore	43295	13.0N	77.6E
Begampet	43128	17.5N	78.5E
Belgaum	43197	15.9N	74.7E
Bikaner	42165	28.0N	73.3E
Bogra	41858	24.9N	89.4E
Bombay	43057	18.9N	72.9E
Calcutta	42807	22.5N	88.4E
Chaingmai	43827	18.8N	99.0E
Cherrapunji	42515	25.3N	91.8E
Chumphon	48517	10.5N	99.3E
Colombo	43466	6.9N	79.9E
Cuttack	42970	20.8N	85.9E
Daltonganj	42587	24.1N	84.1E
Darbhanga	42391	26.2N	85.9E
Darjelling	42295	27.1N	88.3E
Dhubri	42404	26.0N	90.0E
Dibrugarh	42314	27.5N	95.0E
Dumka	42599	24.3N	87.3E
Dwarka	42731	22.4N	69.1E
Fort Cochin	43351	10.0N	76.3E
Gauhait	42410	26.1N	91.6E
Goa	43192	15.5N	73.8E
Hambantuta	43497	6.1N	87.1E
Hyderabad	41765	25.4N	68.4E
Indore	42754	22.7N	75.8E
Jacobadad	41715	28.3N	68.5E
Jagdalpur	43041	19.1N	82.0E
Jessore	41915	23.2N	89.2E
Jodhpur	42339	26.3N	73.0E
Kota	42451	25.2N	75.9E
Madras	43279	13.1N	80.3E
Mangalore	42383	12.9N	74.9E
Mannar	43413	9.0N	79.9E
Masulipatam	43185	16.2N	81.2E
Minicoy	43369	8.3N	72.8E
Mukteswar Kumaon	42147	29.5N	79.7E
Nagpur	42867	21.2N	79.2E
Narayanjanj	41919	23.6N	90.5E
New Delhi	42182	28.7N	77.3E

STATION	WMO NUMBER	LATITUDE	LONGITUDE
Pamban	43363	9.3N	79.3E
Poona	43063	18.5N	73.9E
Port Blair	43333	11.7N	92.8E
Prachaup Khirikhan	48500	11.8N	99.8E
Sagar	42671	23.9N	78.8E
Srimangal	41880	24.3N	91.7E
Silchar	42619	24.8N	92.8E
Trincomalee	43418	8.6N	81.2E
Trivandrum	43371	8.5N	77.0E
Veraval	42909	20.9N	70.4E
Vishakhapatnum	43149	17.7N	83.3E

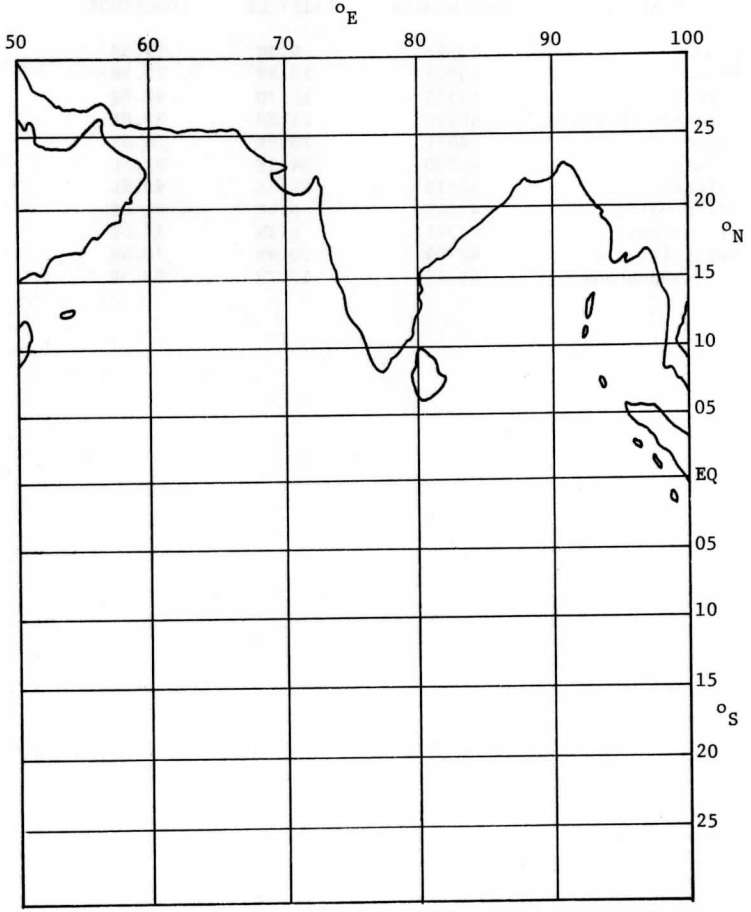

Figure 1. Geographical location of the study area. The sixty cloud analysis areas are outlined by the latitude and longitude lines.

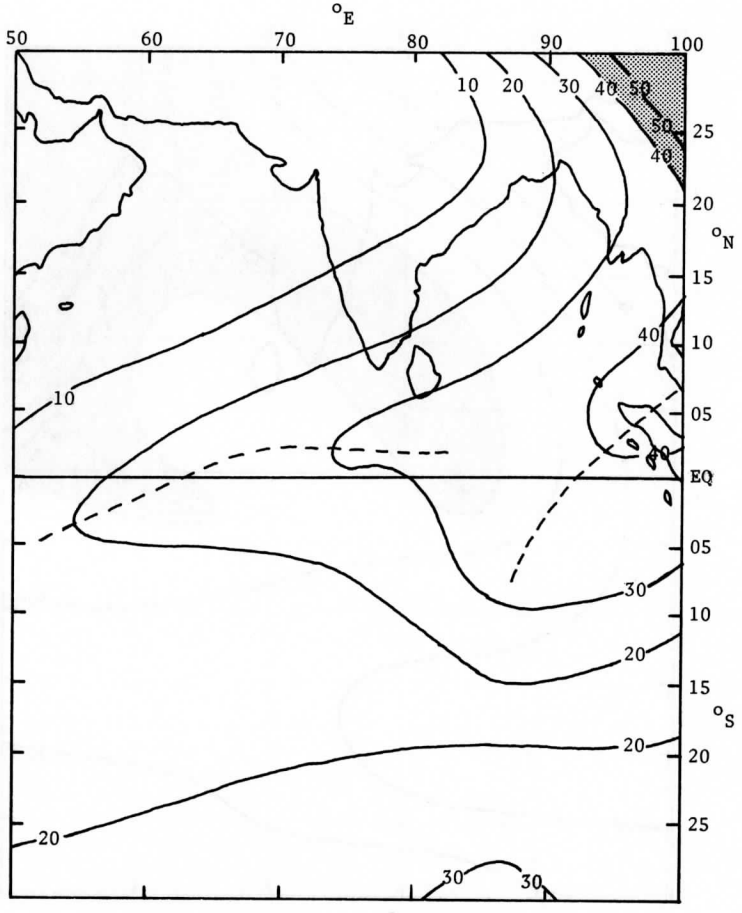

Figure 2. Mean areal cloud cover in percent for May during the years 1967 through 1969. Areas with greater than 40 percent coverage are shaded. Dashed lines indicate regional maximum values.

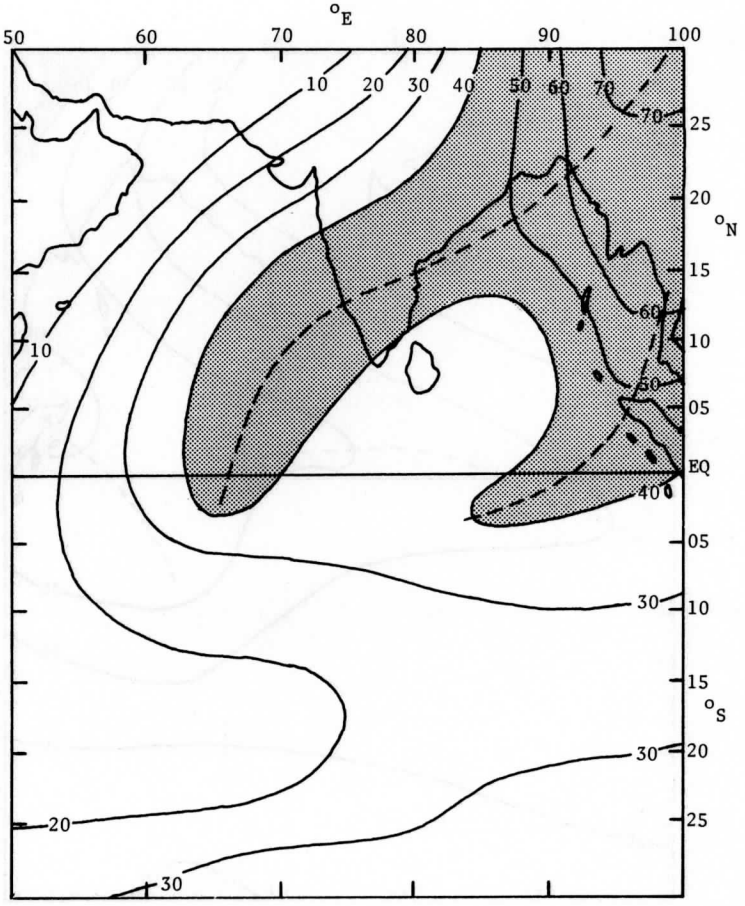

Figure 3. June mean cloud cover as presented in Figure 2.

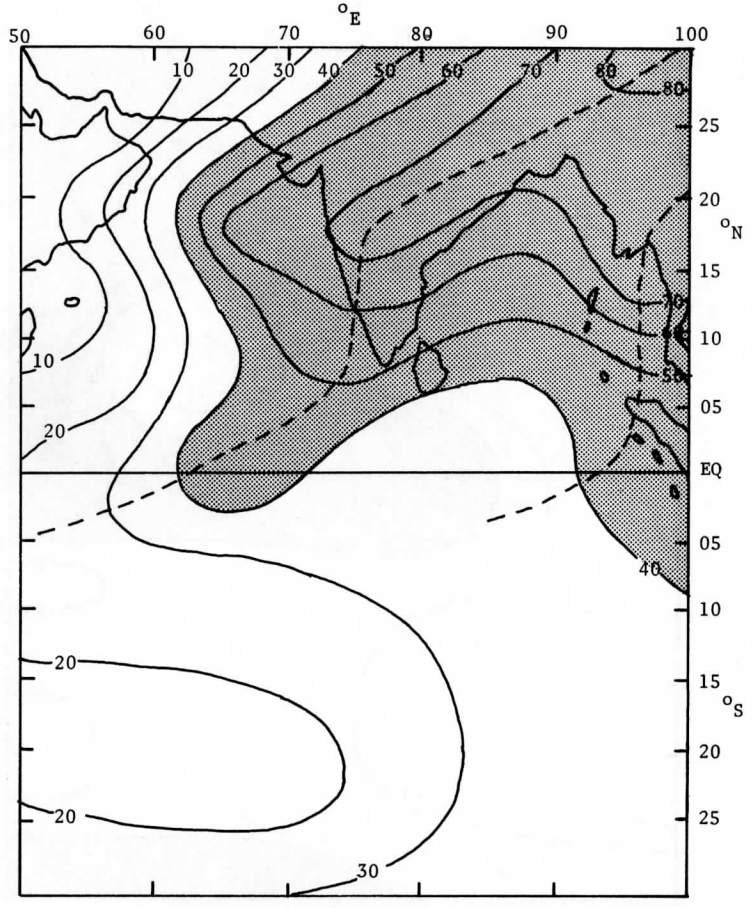

Figure 4. July mean cloud cover as presented in Figure 2.

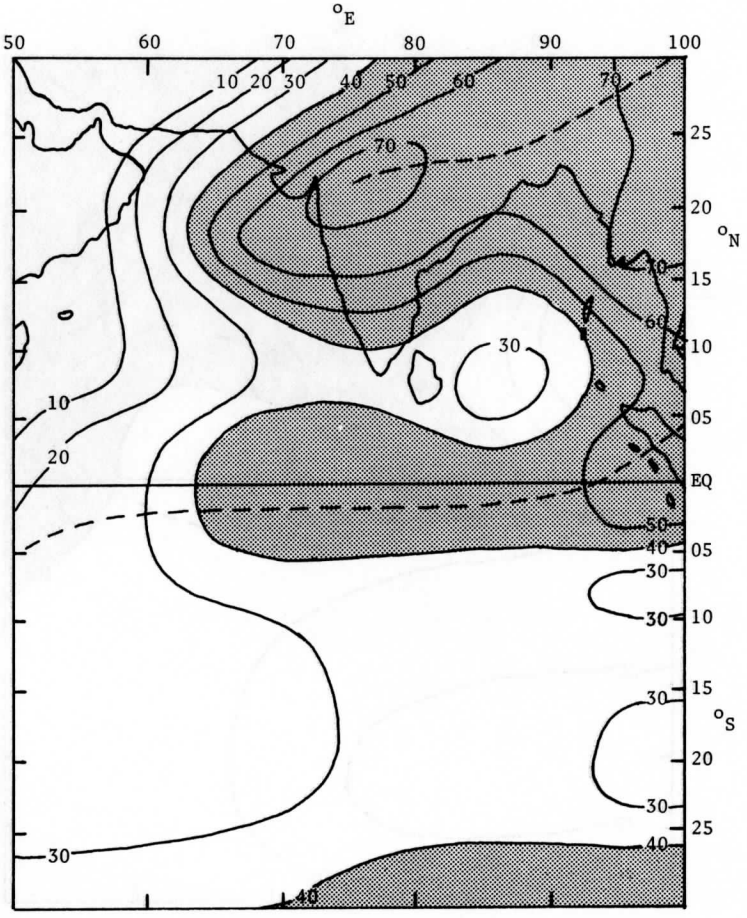

Figure 5. August mean cloud cover as presented in Figure 2.

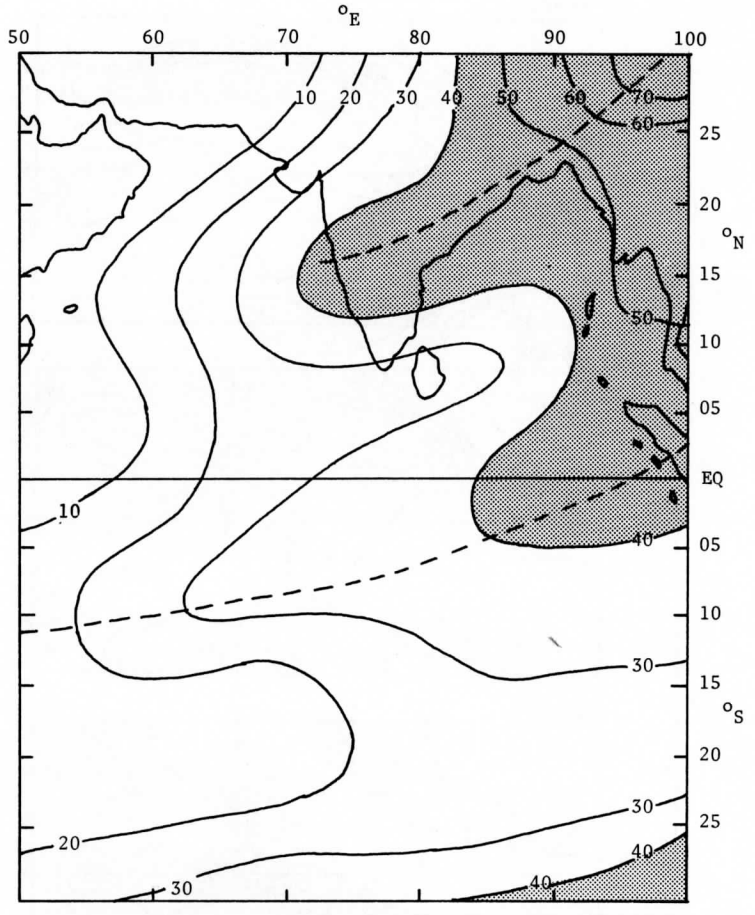

Figure 6. September mean cloud cover as presented in Figure 2.

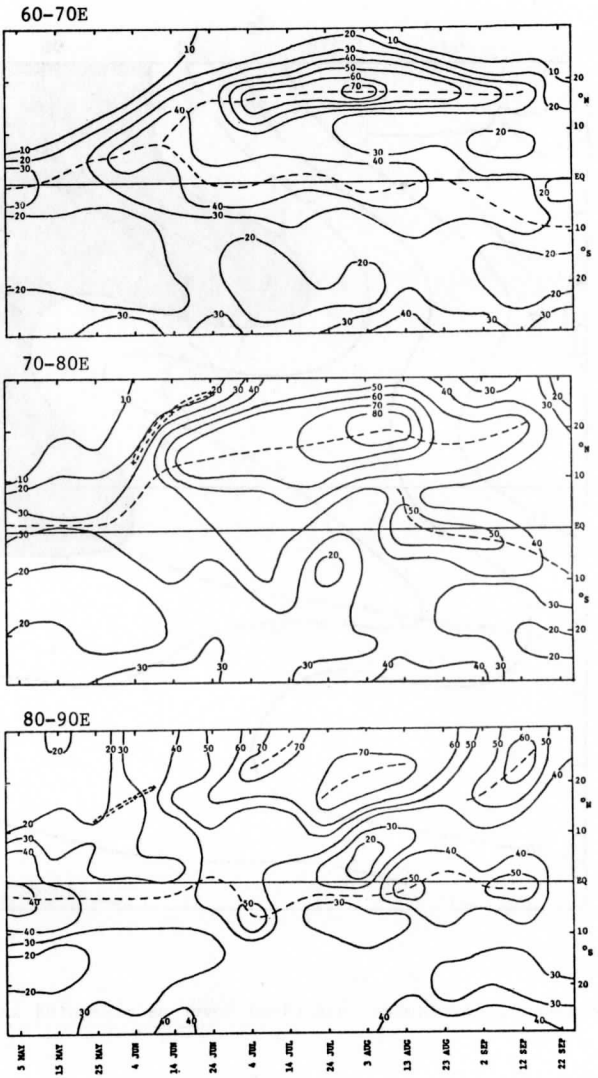

Figure 7. Isopleths of percentage areal cloud cover in time versus latitude for the longitude sectors 60-70°E, 70-80°E and 80-90°E. Values are mean values for 1967 through 1969. Double dashed lines are normal monsoon onset as presented by Das (1968). Single dashed lines indicate maximum values.

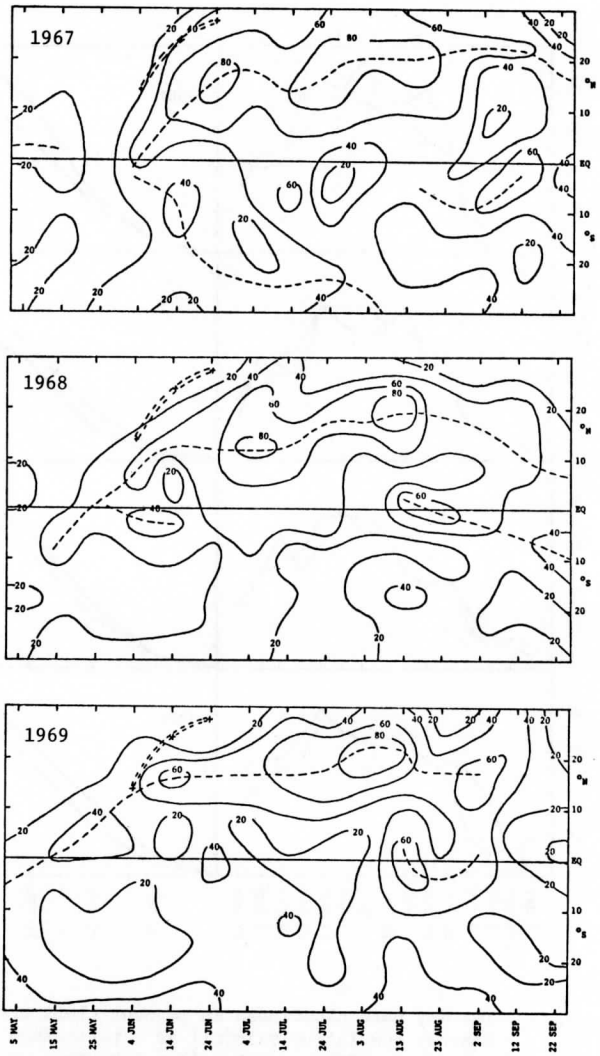

Figure 8. Isopleths of percentage areal cloud cover in time versus latitude for the longitude sector 70-80°E during each year 1967 through 1969. The double dashed line represents the normal monsoon onset as presented by Das (1968). The single dashed lines indicate maximum values.

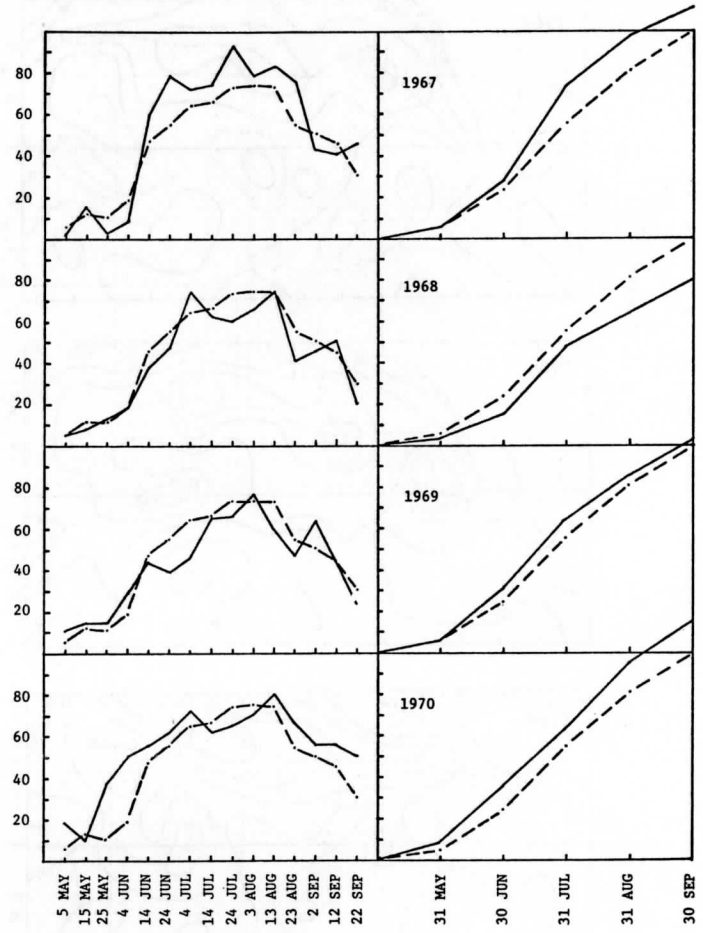

Figure 9. Ten day mean cloudiness in percent (left graphs). Monthly cumulative rainfall as a percentage of the ten year (1961-1970) seasonal (May-September) rainfall (right graphs). The years 1967 through 1970 are presented. The area represented is 10-15°E. Vertical coordinate is in percent. The dashed rainfall curve is the ten year mean rainfall for 1961 through 1970. The dashed cloudiness curve is the mean of the three years 1967-1969.

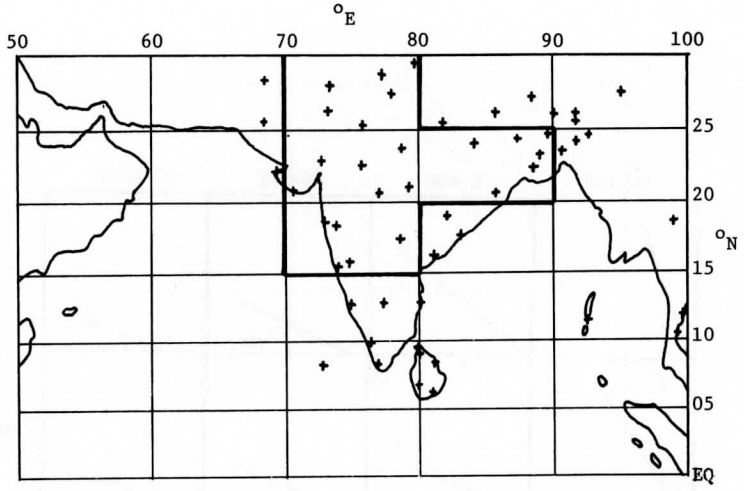

Figure 10. Plot of stations used for rainfall analysis. The area enclosed in dark lines is that with best station coverage.

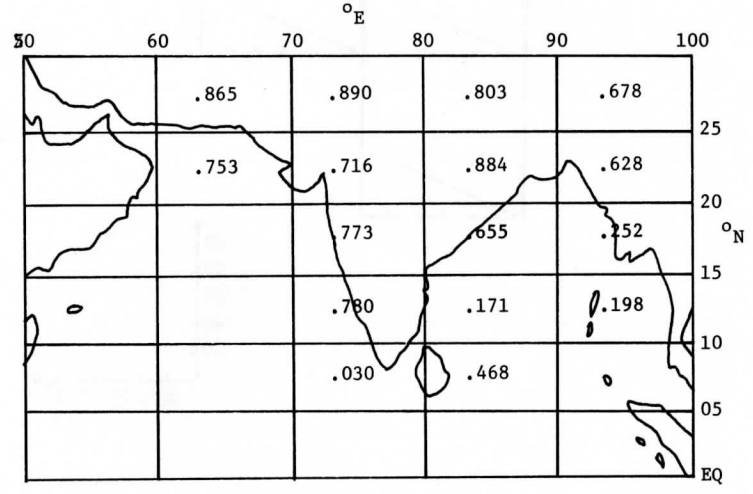

Figure 11. Linear correlation coefficients between monthly mean cloudiness and monthly rainfall.

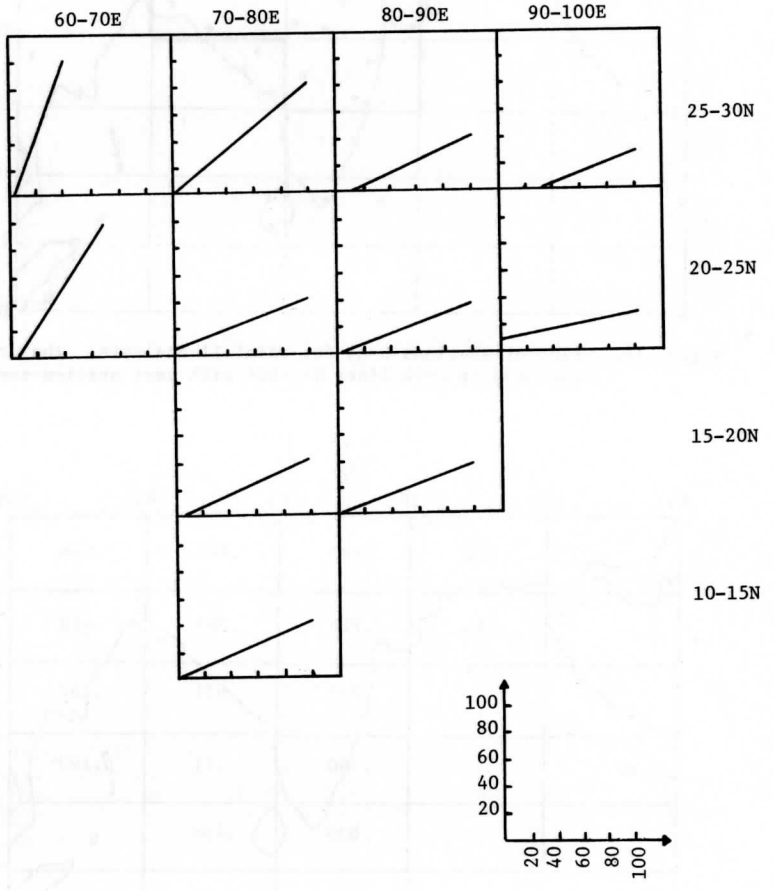

Figure 12. Linear regression lines relating mean monthly cloudiness to monthly rainfall by area. Percent of mean seasonal rainfall is the ordinate. Percent of areal cloud cover is the abscissa.

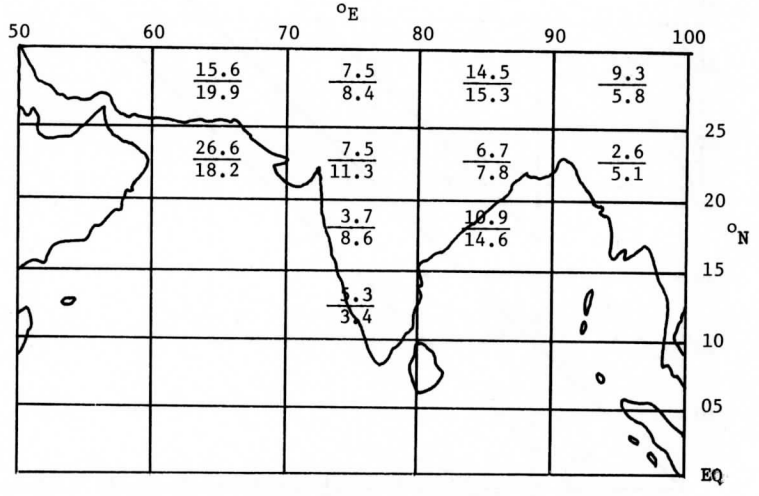

Figure 13. RMS differences in percent of mean seasonal precipitation between estimated and observed rainfall for 1970. Upper numbers present errors which resulted from use of the estimation technique of this study. Lower numbers represent the errors which resulted from use of a ten year mean for estimation.

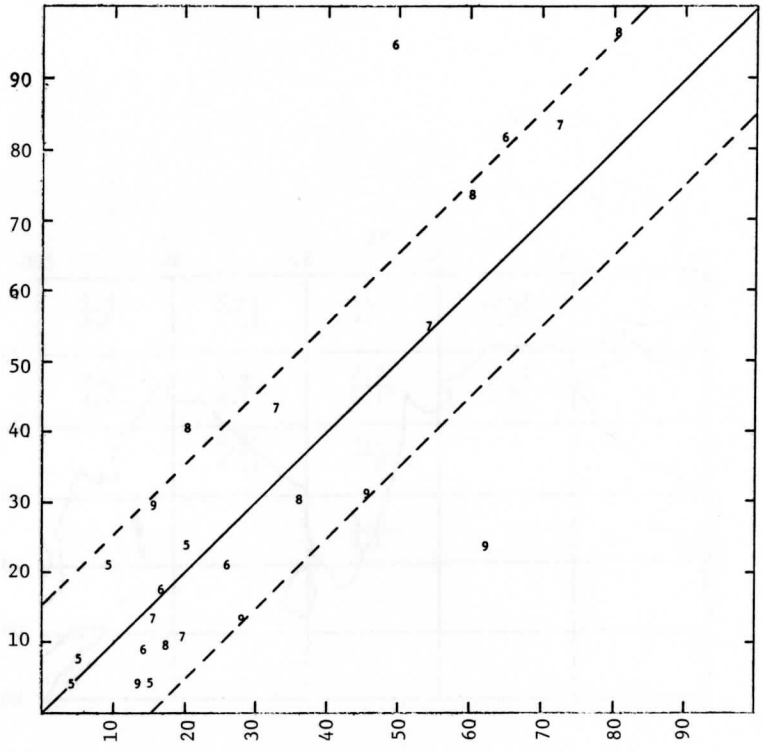

Figure 14. Scatter diagram of the 1970 verification data given in Table 4.1 for the estimation technique of this study. The number plotted indicates the month of the estimate.

TEMPORAL CLOUD STATISTICS OVER THE ASIAN MONSOON REGION AND ADJACENT AREAS DURING THE SUMMER

D. N. Sikdar and B. Auvine

ABSTRACT

Daily estimates of percentage cloud cover taken from ESSA-3 mosaics for réctangular areas, 5° latitude by 10° longitude were compiled for the summer seasons of 1967 thru 1969 over an area 30°N to 30°S and covering varying longitudes between 0° and 140°E. Monthly and seasonal averages were obtained, as well as a spectral analysis of the data. Results show a clear progression of the monsoon northward from the equator in the 60° to 90°E sector with cloudiness reaching a peak of 75%. The spectral analysis indicates the presence of northward and westward moving waves with periods between 8.6 and 20 days over the Indian subcontinent, the Bay of Bengal, and parts of Southeast Asia. Waves of shorter periodicities can be found in areas closer to the equator and over Africa.

1. INTRODUCTION

This is the fifth in a series of papers using satellite cloud data to quantitatively document the space-time behavior of tropical cloud systems. In this paper attention is given specifically to the Asian monsoon, utilizing synoptic scale satellite cloud data during the summer months. While some use of such data has been made previously (Ramage, 1971) in the form of mean monthly charts of monsoon cloudiness, this study has the objective of obtaining the spectral characteristics of the large scale cloud systems that affect the region. An additional goal of this study is to document the geographical variations in cloudiness in the region from 0° to 140°E, as a suppliment to what has already been done in the tropical Pacific (Sikdar, Young, and Suomi, 1972) (Young and Sikdar 1973a) and the tropical Atlantic (Young and Sikdar 1973b) (Heinricy and Young, 1974). Finally, the relevance of the findings in this paper to Indian and Southeast Asian monsoon research will be briefly examined.

2. DATA ANALYSIS

The data set used in this study consists of daily estimates of percentage cloud cover taken from ESSA-3 mosaics for rectangular areas measuring 5° latitude by 10° longitude. Three years of such data were utilized: 1967 thru 1969 for the months of May thru October (May to September in 1969). Latitudes covered were from 30°N to 30°S and longitudes 60°E to 120°E (0° to 140°E for 1967). Of these three years, precipitation records show 1967 and 1969 were the most active monsoonally (in terms of rainfall) while 1968 had a relatively weak monsoon season.

This area includes a larger region than that affected by the classical monsoon; however, in order to facilitate the detection of waves entering the monsoon region from adjacent areas, a larger area covering Africa and the oceanic areas south of the equator needs to be included for at least part of the data sample. The time series of the cloud amount data has been analyzed by computing the time mean and using a normalized high band pass filter. The reader is referred to Sikdar, Young, and Suomi (1972) for additional details on the data and data analysis.

3. CLIMATOLOGICAL FEATURES OF THE UNFILTERED CLOUD AMOUNTS

Before going on to the spectral analyses, a clear picture of the observable behavior of the raw mean cloud patterns over the region of study is desirable. Figure 1 shows a base map of the region of analysis with isopleths of the mean summer cloudiness for 1967. As observed in earlier studies (Ramage, 1971), this map features maximum areas of cloudiness over the Indian-Southeast Asian region and in a belt extending across central Africa. Summer cloudiness diminishes to a minimum over southern Africa and south of the Asian land mass. Variability of the high cloudiness regions measured with respect to the standard deviation is high (as one would expect in areas of frequent passage of storm systems) with a maximum deviation of 35% over the Indian subcontinent. Figure 2 shows the mean cloudiness for the month of July, the time during which the monsoonal cloudiness reaches a maximum. While the locations of the centers of high and low cloudiness are essentially the same as for the summer map (Figure 1), the magnitudes of the high cloudiness have substantially increased. The area of cloudiness over India and the western portion of Southeast Asia has an average cloudiness of between 70 and 85%.

In order to show more clearly the monthly changes in terms of a northward shift of the maximum cloudiness, average cloudiness over different longitudinal sectors was computed as a function of latitude. The longitudinal belts used were the region west of the Indian monsoon (0° to 60°E), the Indian monsoon region (60°E to 90°E), and the Southeast

Asian monsoon region (90°E to 140°E). It is to be expected that characteristics of the northward shift in cloudiness would be different in the three regions because the first region exhibits only a weak monsoon pattern in comparison to the classic Indian monsoon with general mid-tropospheric subsidence, while the occurrence of the monsoon in the third region is intermittent and less pronounced than it is over India. These characteristics are borne out in a comparison of the graphs of cloudiness versus latitude in Figures 3 through 5. The increase in maximum summer cloudiness in the western region shows only a slight northward shift over the summer months (from 2.5°N to 7.5°N) and a gradual increase of from 18% to 54% from May to July. Because the maximum cloudiness remains so close to the equator, it would appear likely that this shift is due simply to the movement of the Intertropical Convergence Zone rather than any true monsoonal changes. In contrast, region two over the Indian subcontinent shows a very dramatic change between May and June and September and October with a movement of maximum cloudiness from 2.5°N in May to 17.5°N in June and an increase in cloudiness from 30% to 75% between May and July. Region three in Southeast Asia shows a less well defined monsoonal pattern with a shift of the maximum cloudiness from 2.5°N to 12.5°N between May and June, with a secondary maximum still in evidence near the equator. Changes in percent maximum cloudiness are from 30% to 65%. In all three regions little change in the cloudiness amounts can be seen south of the equator. Similar results are true of the other two years examined. Even for the low monsoonal rainfall year (1968), there is a similar progression of monsoonal cloudiness northward in the 60° to 90°E region (Figure 6).

4. SPECTRAL CHARACTERISTICS OF THE HIGH PASS FILTERED CLOUD AMOUNT DATA

Two different sorts of spectral analyses were performed on the filtered cloud amount data: time series correlations between adjacent longitudinal boxes (5° latitude by 10° longitude) and time series correlations between adjacent latitudinal boxes. This made it possible to detect the existence of both north-south and east-west moving waves. Figures 7 and 8 present the normalized power spectral values for two different periods: 8.6 to 20 days and 2.9 to 5.5 days respectively. In general, note that long period waves can be clearly seen in the monsoon region as well as in equatorial and north central Africa, where they contribute more than 30% of the total variance. The short period waves are more evident over the oceanic regions to the south of the Asian land mass. These results suggest that if any cycles do exist in monsoon cloudiness, they are not simply those resulting from single synoptic disturbances, but are connected to some longer term phenomenon. Similar patterns of the same spectral values for 1968 are indicated in Figures 9 and 10 for the same periodicities. Although the longitudes covered extend only from 60° to 120°E, maxima over the Indian subcontinent for the

long periodicities and to the south of the Asian land mass for short periods are still evident. One interesting difference in the two years may be seen in a shift of an area of maximum coherency magnitudes from northern India to parts of Southeast Asia in Figure 9 (2.9 to 5.5 day periods). Comparison of Figures 7 and 8 with Figure 1 reveals that both years show shorter periods in regions of low cloudiness and longer periods in regions of high cloudiness. This is similar to a finding by Sikdar et al. (1972) for the central Pacific. They also found shorter wavelengths predominating near the equator and vice versa away from the equator. No such pattern emerges from the data being examined here.

Some further light can be shed on the motion of these waves by examination of Figures 11a and b, and 12a and b for the years 1967 and 1968. Plotted are the phase angles for periodicities whose coherence exceeds 0.50. Waves with periods of from 8.6 to 20 days show in the region north of the equator (where they are most significant) a tendency for westward motion. Waves with shorter periods (Figures 12a, b) also show the same characteristic of westward motion.

A similar sort of analysis was performed for the latitudinal correlations, although here attention was confined to the area from 60° to 140°E, given the differing characteristics of the area east of 60°E previously described. The phase angle plots for 1967 (Figures 13a, b and 14a, b) indicate for the longer periodicities (8.6 to 20 days) some tendency for northward motion north of the equator and vice versa south of the equator. Results are less clear for the shorter waves (2.9 to 5.5 days). Some suggestion of northward motion north of the equator can still be seen, however. The 1968 data provides similar results.

In summary, these analyses suggest summertime monsoon cloudiness over the Indian subcontinent, the Bay of Bengal, and most of Southeast Asia is associated with northward and westward moving waves with periodicities between 8.6 and 20 days. In some areas to the south of the Asian land mass shorter waves moving both northward and westward are evident.

5. DISCUSSION OF THE RESULTS IN RELATION TO PREVIOUS MONSOON RESEARCH

In previous studies of monsoon characteristics it is notable that no predominating periodicity has been found, although fluctuations in such parameters as rainfall and pressure are readily apparent from conventional data. Although this study cannot claim to have shown that periods of from 8.6 to 20 and from 2.9 to 5.5 days are the most significant fluctuations to be found, unquestionably the occurrence of such periodicities in all three years of data and in both the north-south and east-west spectral analyses points to their possible relation to some physical characteristic of the monsoon circulation.

It seems significant that the 8.6 to 20 day periods are present in both the north-south and east-west patterns. There is possibly some linkage between the two wave patterns either as manifestations of the same phenomenon or part of some alternating phenomena.

The evidence of periods of from 2.9 to 5.5 days south of the Asian land mass suggests their possible relation to passing synoptic disturbances.

In the future, it would be useful to correlate the fluctuations of cloud amounts with conventional data on the circulation and rainfall in order to ascertain more directly the relation of the statistically derived fluctuations with physical parameters.

ACKNOWLEDGEMENTS

Thanks are due to Drs. John A. Young and W. Richard Barchet for reviewing the manuscript and providing suggestions. The research reported in this paper was supported by NOAA under Grant 04-3-158-61.

REFERENCES

Heinricy, D. J. and J. A. Young, 1974: Long-term Variations in High and Low Frequency Cloud Activity Over the East Atlantic-West Africa Region. Submitted to the Monthly Wea. Rev.

Young, J. A. and D. N. Sikdar, 1973a: A Filtered View of Fluctuating Cloud Patterns in the Tropical Pacific. JAS., 30, pp. 392-407.

Young, J. A. and D. N. Sikdar, 1973b: Temporal Cloud Statistics Over the Tropical Atlantic During Summer and Winter, Studies of the Atmosphere Using Aerospace Probes: Annual Report 1973, U. Wis. Space Sci. and Engineering Center, pp. 1-27.

Ramage, C. S., 1971: Monsoon Meteorology. Academic Press, New York.

Sikdar, D. N., J. A. Young, and V. E. Suomi, 1972: Time-Spectral Characteristics of Large-Scale Cloud Systems in the Tropical Pacific. JAS., 29, pp. 229-239.

LIST OF FIGURES

13. a. 1967 predominant coherency phase differences, apparent meridional wavelengths, and propagation speeds for periods of 2.9 to 5.5 days, calculated from data at meridionally adjacent (5° latitude width) sectors. Phases are shown only for narrowband coherencies whose magnitudes exceed 0.5.

13. b. Same as Figure 13a but for 1968.

14. a. Same as Figure 13a but for periods of 8.6 to 20 days.

14. b. Same as Figure 13b but for periods of 8.6 to 20 days.

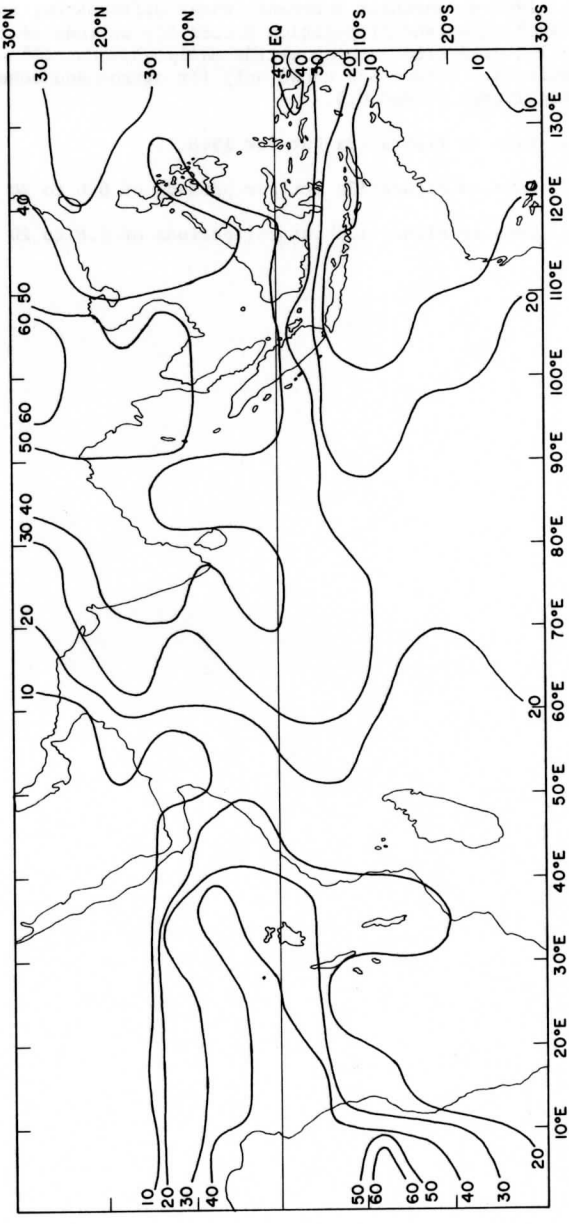
30°N
20°N
10°N
EQ
10°S
20°S
30°S
10°E
20°E
30°E
40°E
50°E
60°E
70°E
80°E
90°E
100°E
110°E
120°E
130°E

Figure 1.

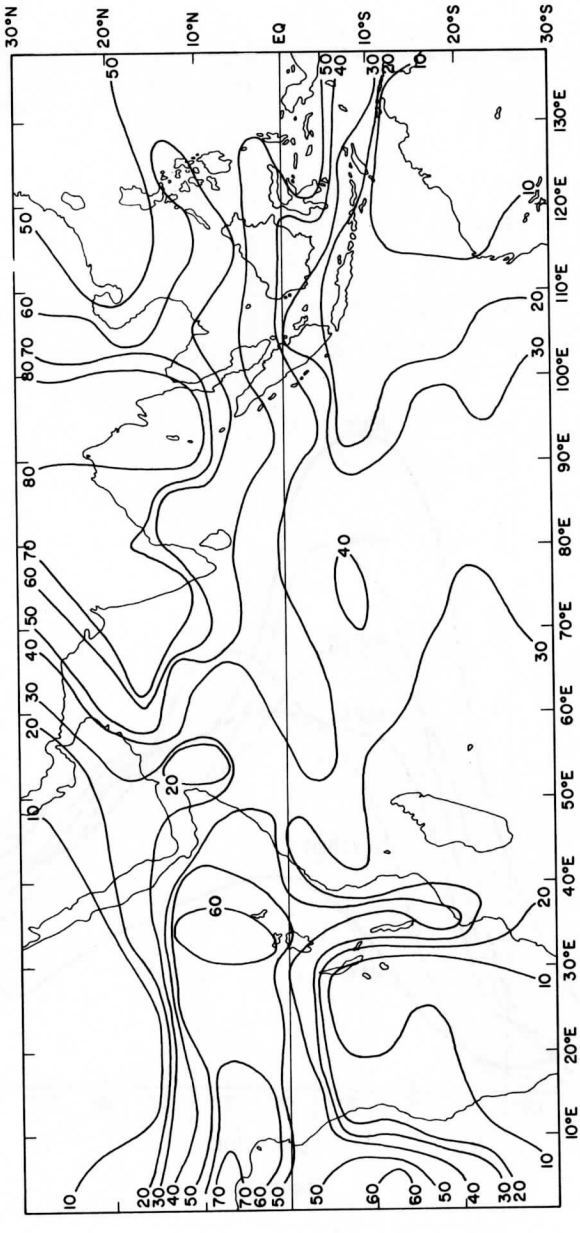
30°N
20°N
10°N
EQ
10°S
20°S
30°S
10°E
20°E
30°E
40°E
50°E
60°E
70°E
80°E
90°E
100°E
110°E
120°E
130°E

Figure 2.

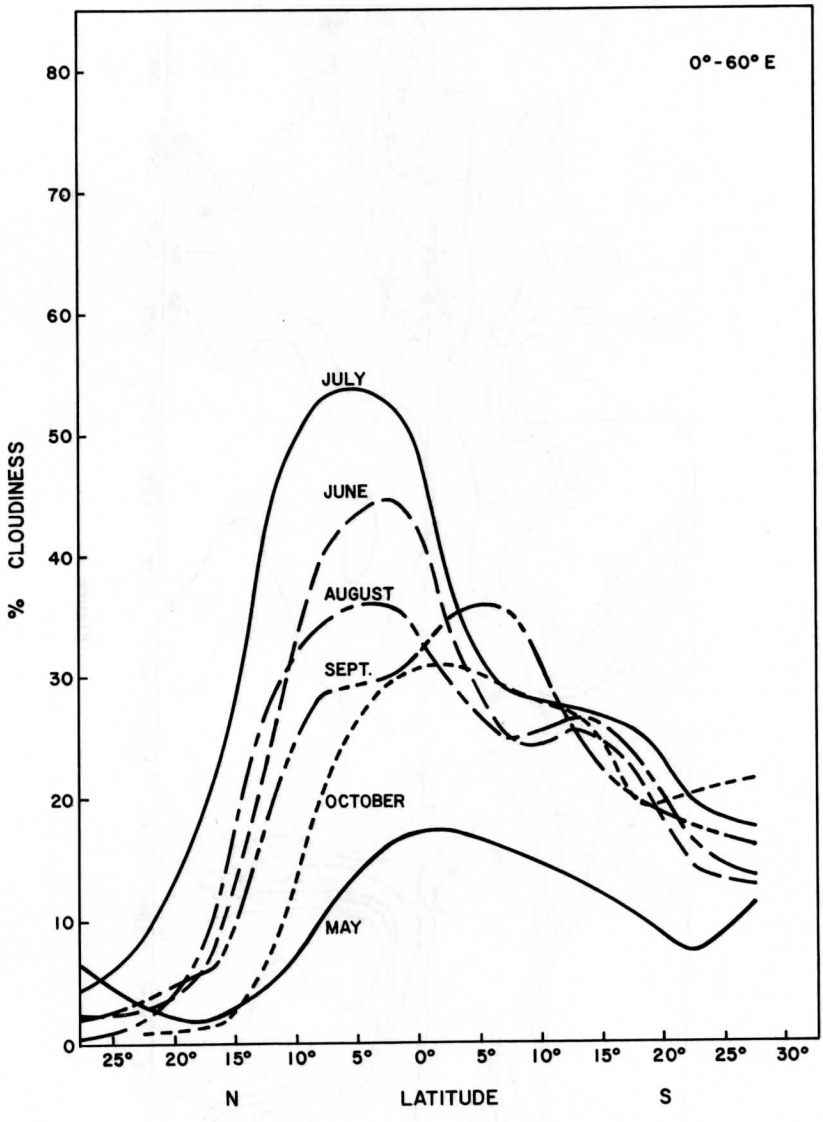
0°-60° E
% CLOUDINESS
80
70
60
50
40
30
20
10
0
JULY
JUNE
AUGUST
SEPT.
OCTOBER
MAY
25° 20° 15° 10° 5° 0° 5° 10° 15° 20° 25° 30°
N
LATITUDE
S

Figure 3.

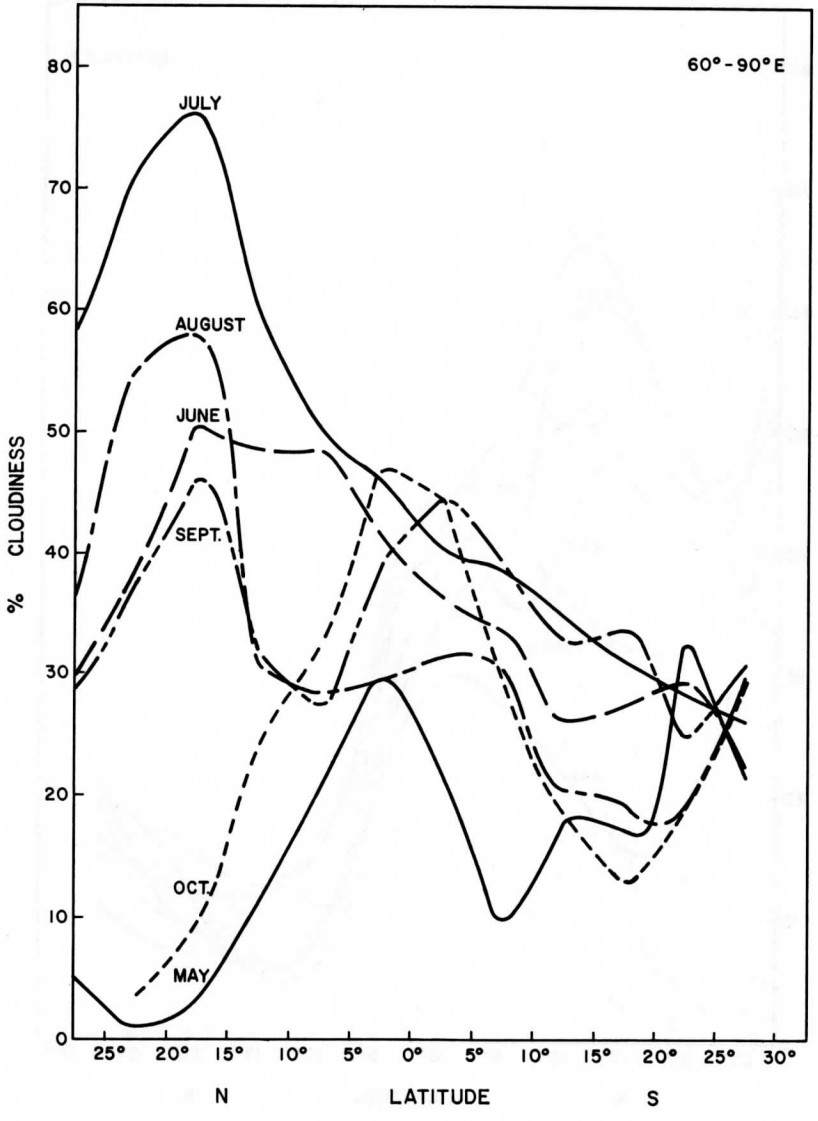
60°-90°E
JULY
AUGUST
JUNE
SEPT.
OCT.
MAY
% CLOUDINESS
80
70
60
50
40
30
20
10
0
25° 20° 15° 10° 5° 0° 5° 10° 15° 20° 25° 30°
N
LATITUDE
S

Figure 4.

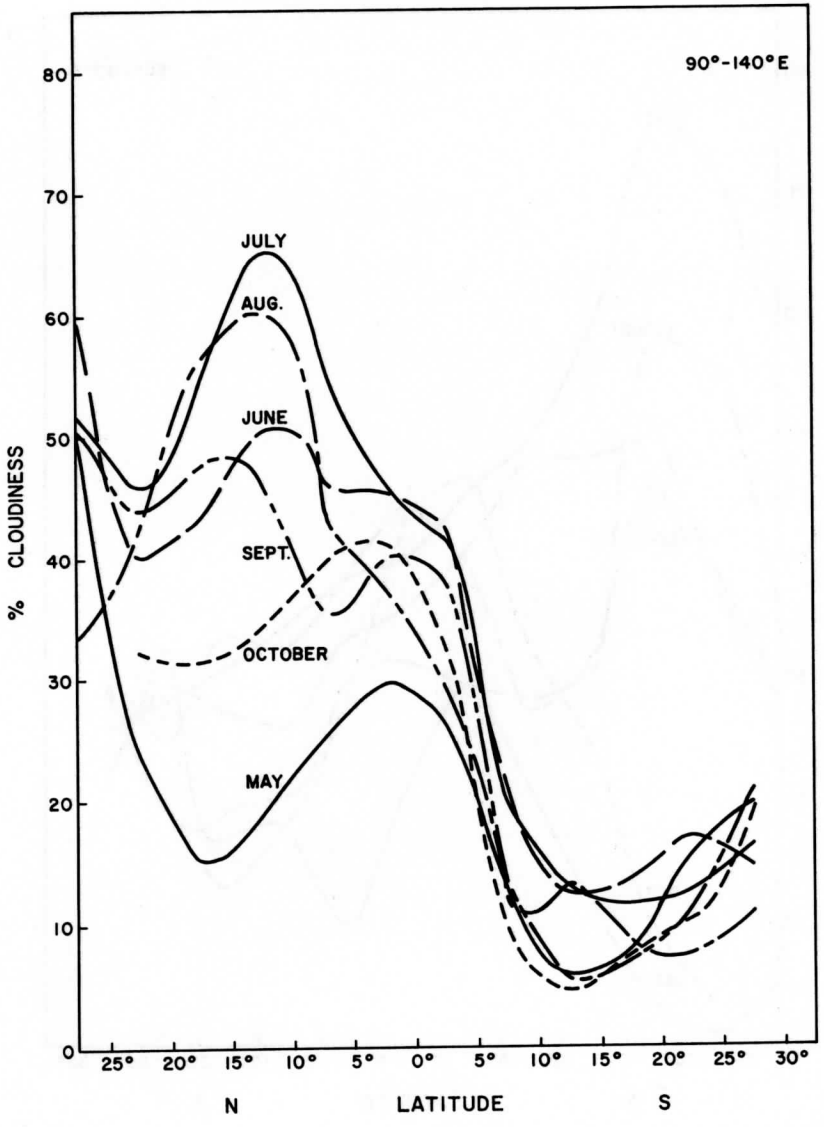
90°-140°E
JULY
AUG.
JUNE
SEPT.
OCTOBER
MAY
% CLOUDINESS
80
70
60
50
40
30
20
10
0
25° 20° 15° 10° 5° 0° 5° 10° 15° 20° 25° 30°
N
LATITUDE
S

Figure 5.

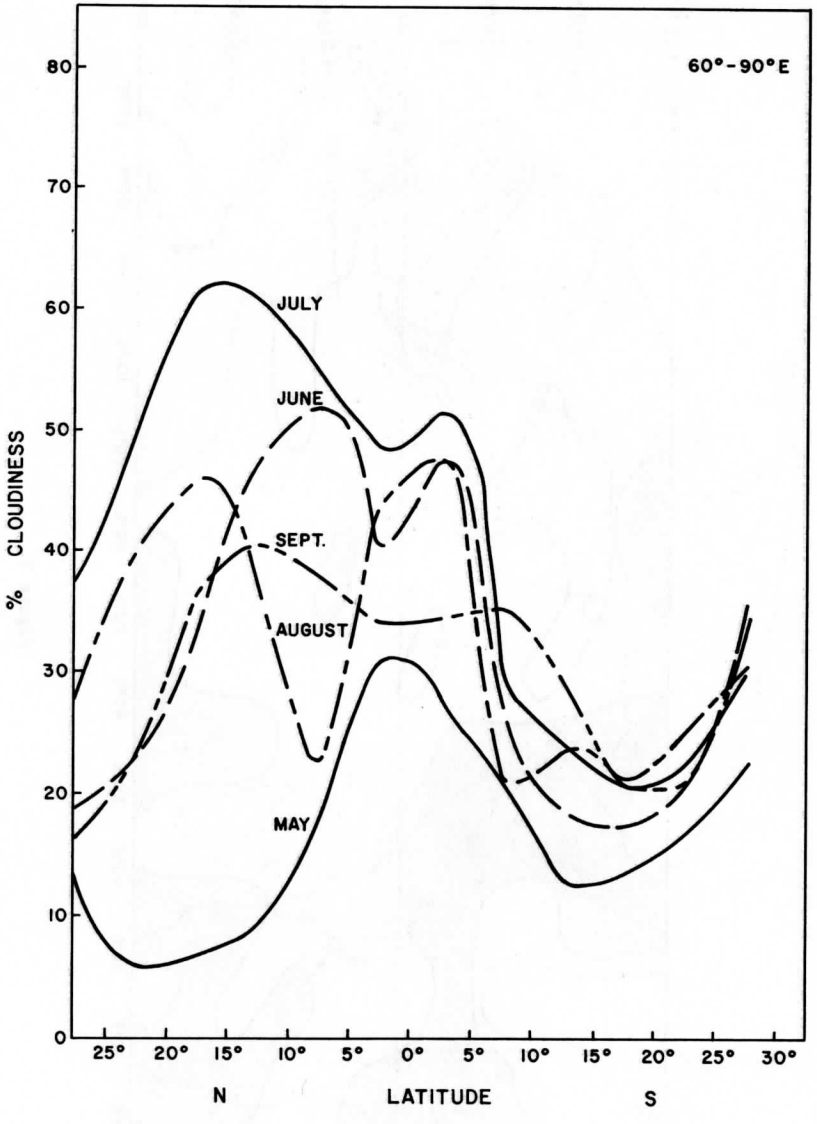
60°-90°E
% CLOUDINESS
80
70
60
50
40
30
20
10
0
JULY
JUNE
SEPT.
AUGUST
MAY
25° 20° 15° 10° 5° 0° 5° 10° 15° 20° 25° 30°
N
LATITUDE
S

Figure 6.

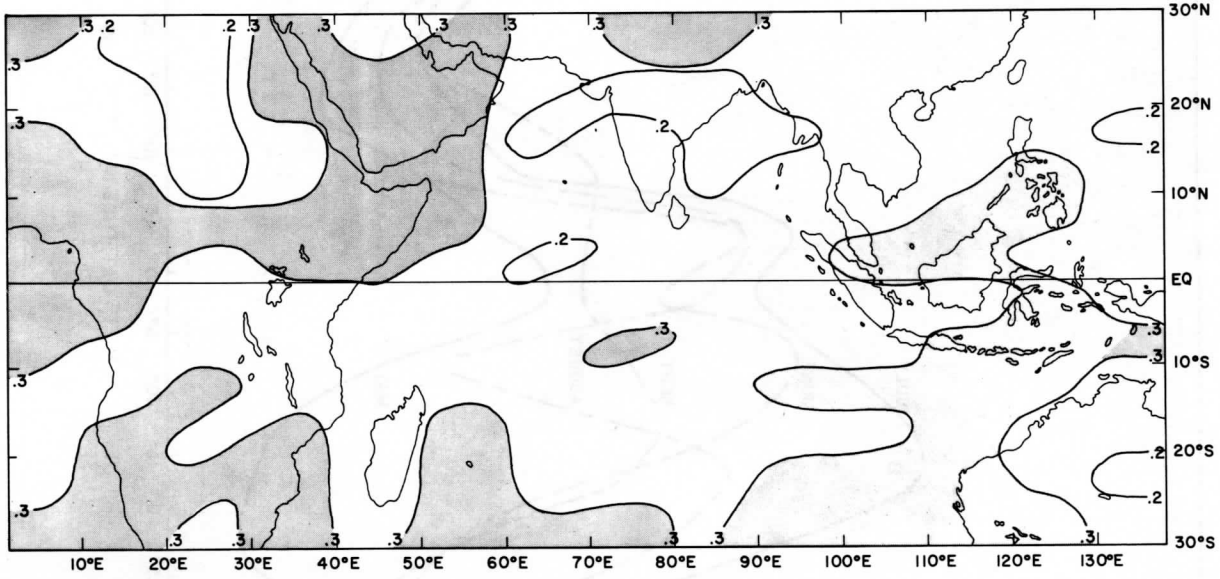
30°N
20°N
10°N
EQ
10°S
20°S
30°S
10°E
20°E
30°E
40°E
50°E
60°E
70°E
80°E
90°E
100°E
110°E
120°E
130°E

Figure 7.

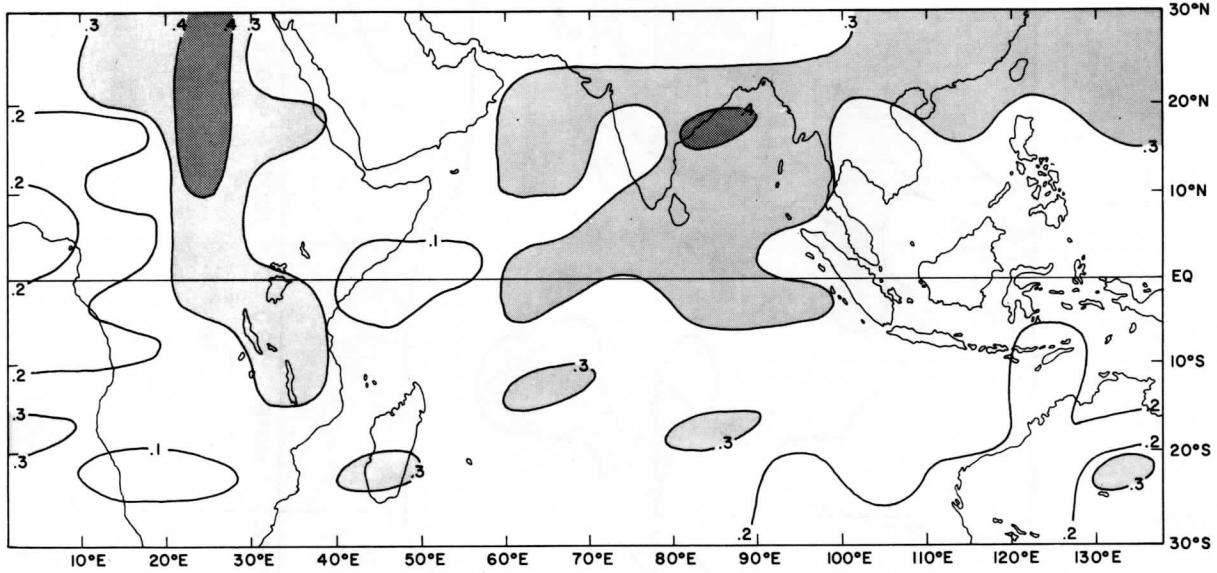
30°N
20°N
10°N
EQ
10°S
20°S
30°S
10°E
20°E
30°E
40°E
50°E
60°E
70°E
80°E
90°E
100°E
110°E
120°E
130°E

Figure 8.

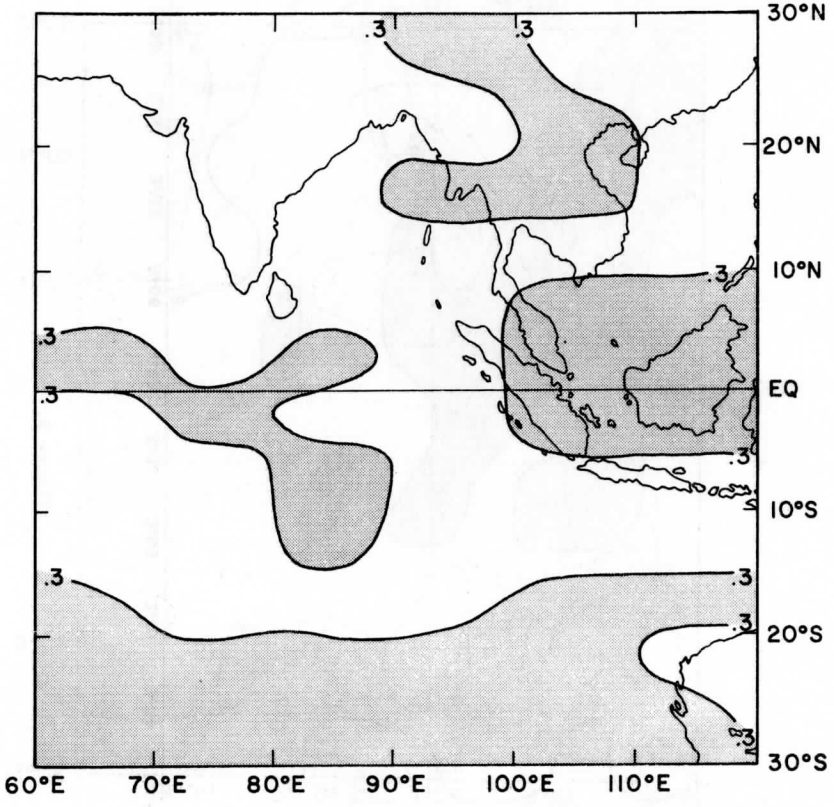

Figure 9.

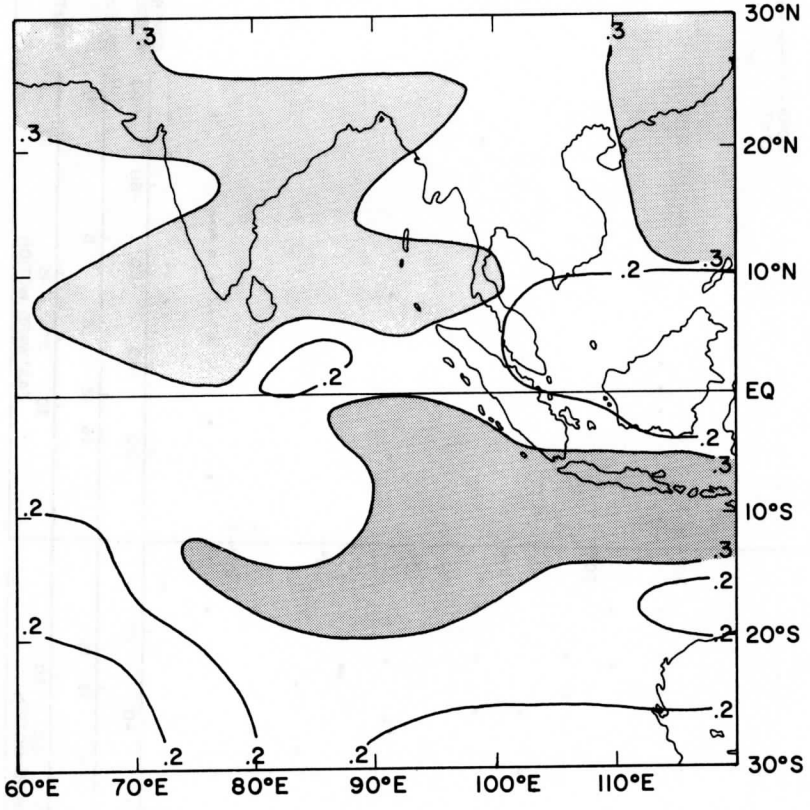

Figure 10.

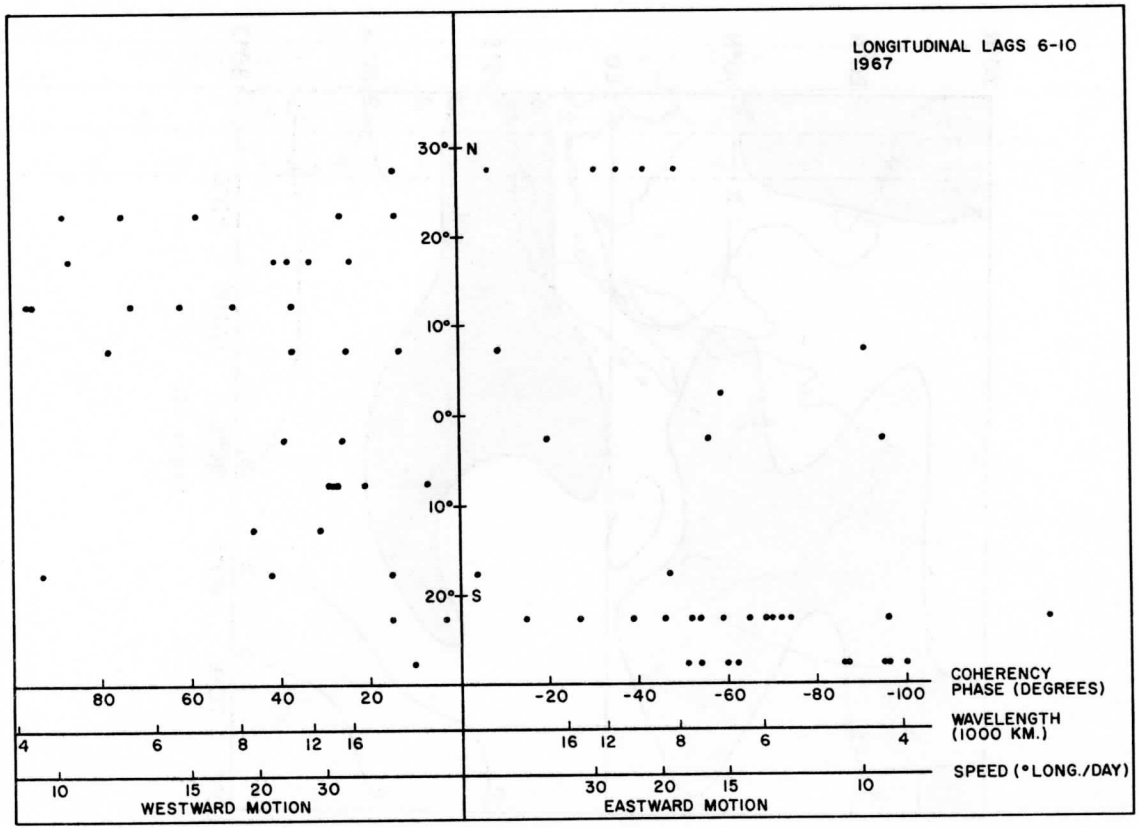
LONGITUDINAL LAGS 6-10
1967
30° N
20°
10°
0°
10°
20° S
80
60
40
20
-20
-40
-60
-80
-100
COHERENCY
PHASE (DEGREES)
4
6
8
12
16
16
12
8
6
4
WAVELENGTH
(1000 KM.)
10
15
20
30
30
20
15
10
SPEED (°LONG./DAY)
WESTWARD MOTION
EASTWARD MOTION

Figure 11a.

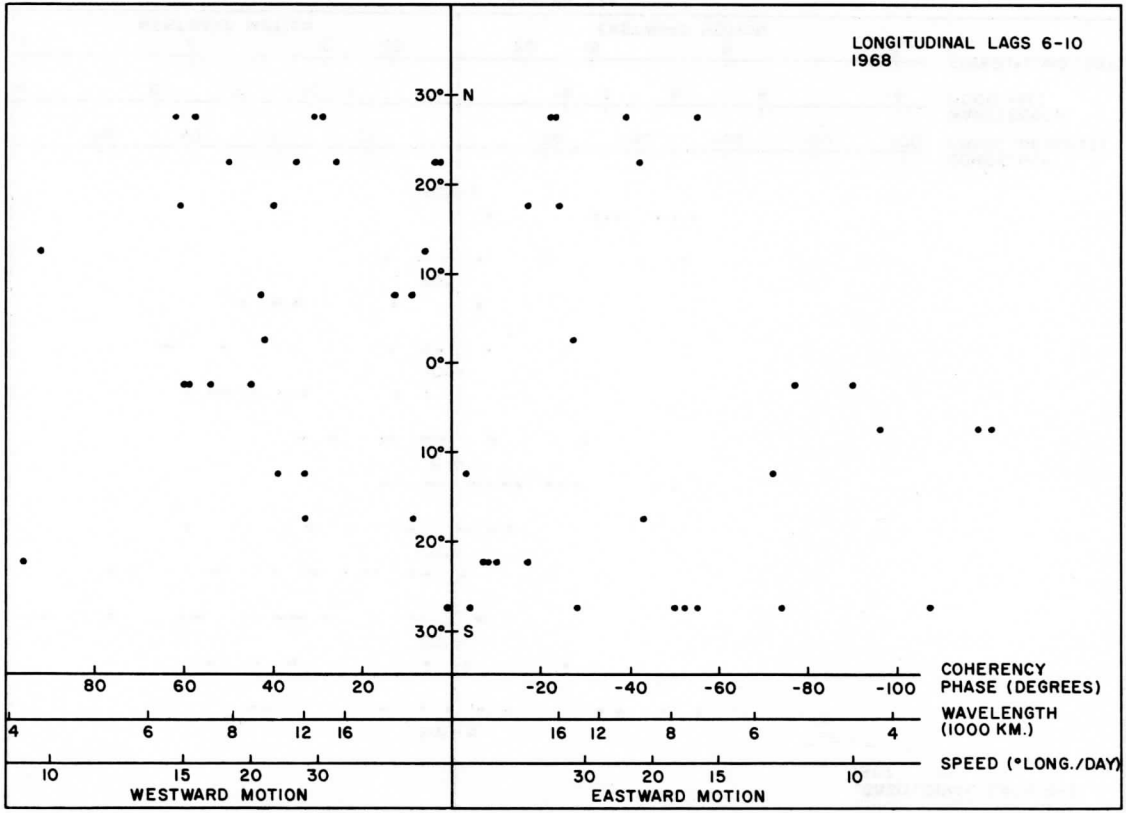
LONGITUDINAL LAGS 6-10
1968
30° N
20°
10°
0°
10°
20°
30° S
80
60
40
20
-20
-40
-60
-80
-100
COHERENCY
PHASE (DEGREES)
4
6
8
12
16
16
12
8
6
4
WAVELENGTH
(1000 KM.)
10
15
20
30
30
20
15
10
SPEED (°LONG./DAY)
WESTWARD MOTION
EASTWARD MOTION

Figure 11b.

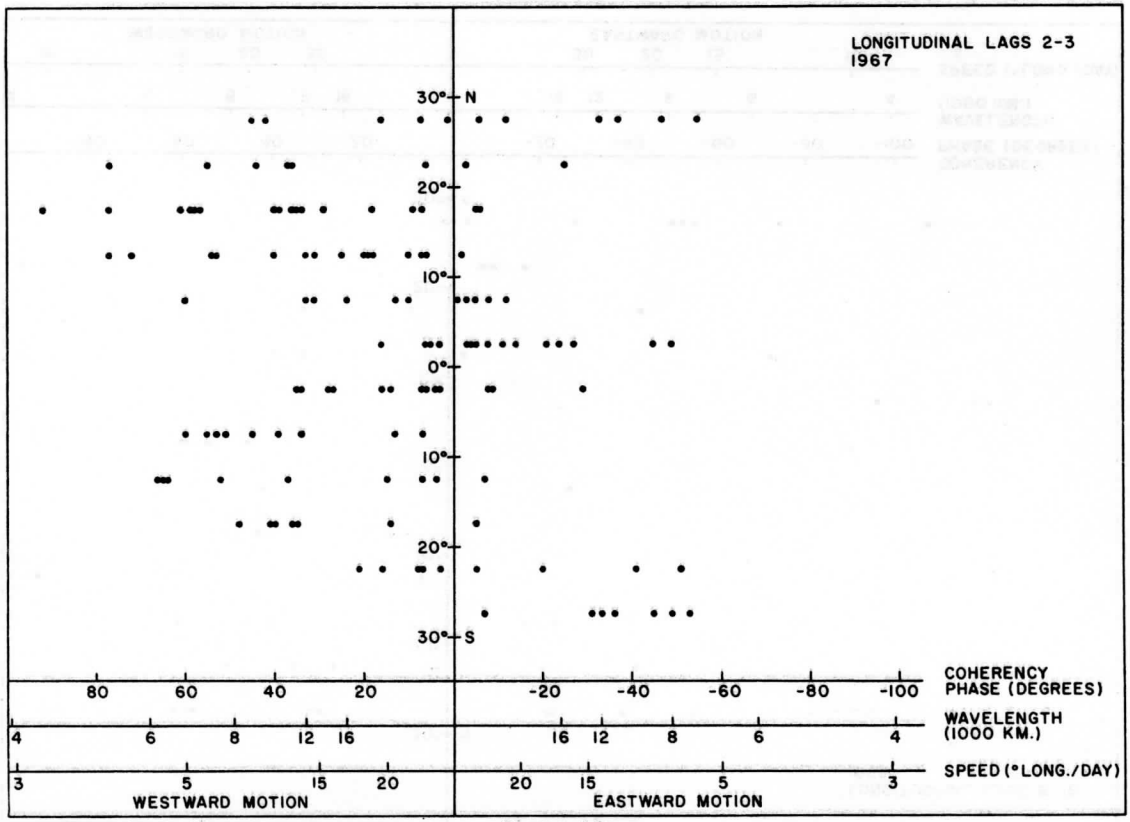
LONGITUDINAL LAGS 2-3
1967
30° N
20°
10°
0°
10°
20°
30° S
80 60 40 20
-20 -40 -60 -80 -100
COHERENCY PHASE (DEGREES)
4 6 8 12 16
16 12 8 6 4
WAVELENGTH (1000 KM.)
3 5 15 20
20 15 5 3
SPEED (°LONG./DAY)
WESTWARD MOTION
EASTWARD MOTION

Figure 12a.

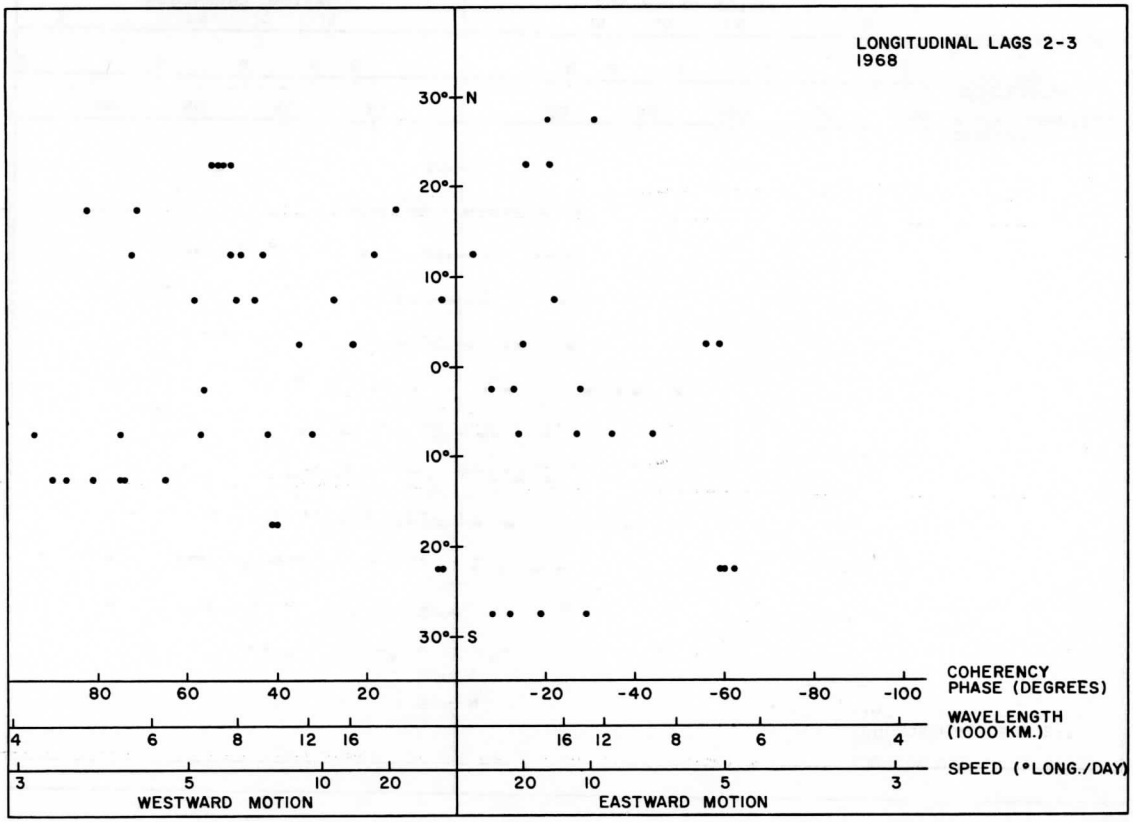
LONGITUDINAL LAGS 2-3
1968
30° N
20°
10°
0°
10°
20°
30° S
80
60
40
20
-20
-40
-60
-80
-100
COHERENCY PHASE (DEGREES)
4
6
8
12
16
16
12
8
6
4
WAVELENGTH (1000 KM.)
3
5
10
20
20
10
5
3
SPEED (°LONG./DAY)
WESTWARD MOTION
EASTWARD MOTION

Figure 12b.

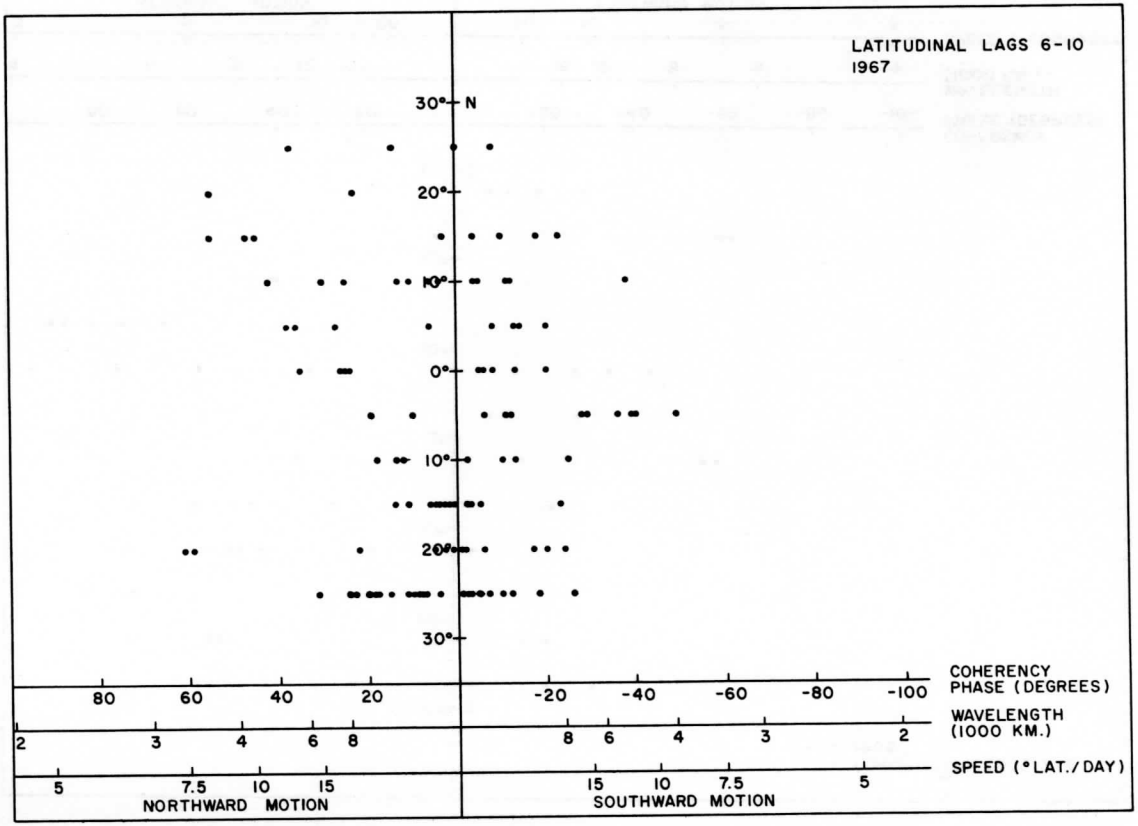
LATITUDINAL LAGS 6-10
1967
30° N
20°
10°
0°
10°
20°
30°
80 60 40 20
-20 -40 -60 -80 -100
COHERENCY PHASE (DEGREES)
2 3 4 6 8
8 6 4 3 2
WAVELENGTH (1000 KM.)
5 7.5 10 15
15 10 7.5 5
SPEED (°LAT./DAY)
NORTHWARD MOTION
SOUTHWARD MOTION

Figure 13a.

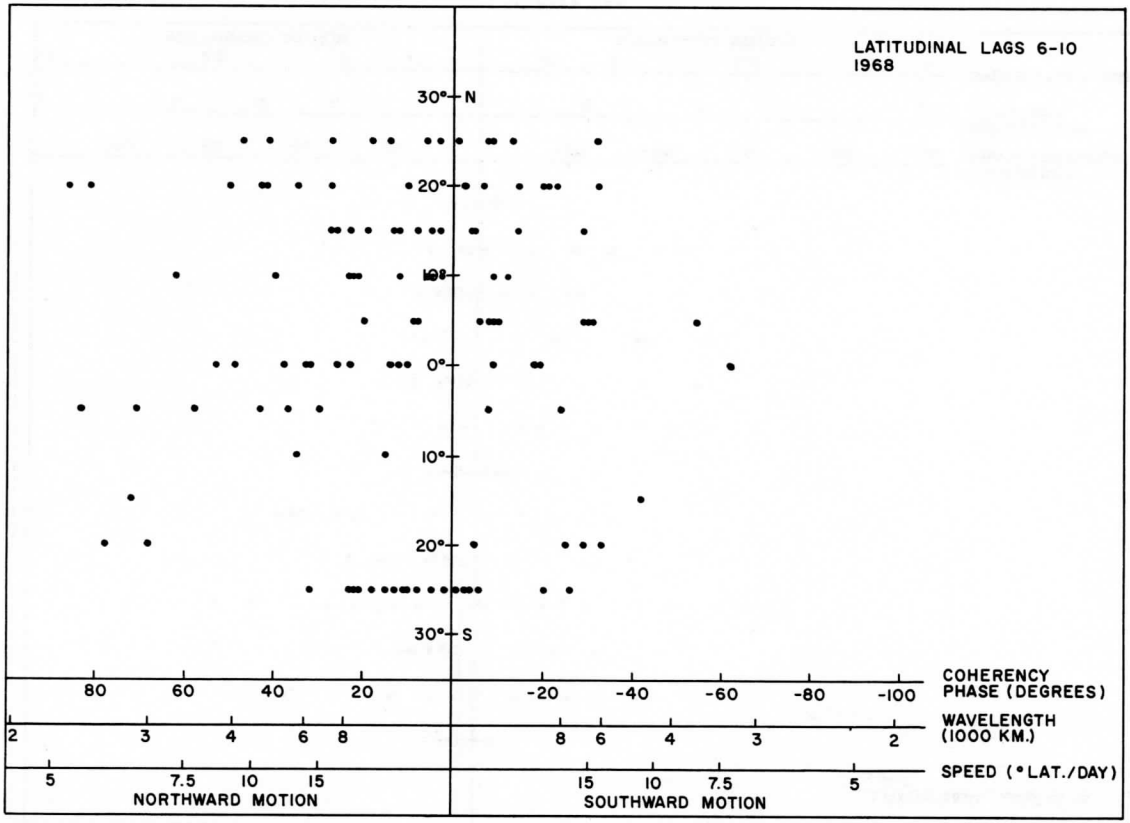
LATITUDINAL LAGS 6-10
1968
30° N
20°
10°
0°
10°
20°
30° S
80 60 40 20
-20 -40 -60 -80 -100
COHERENCY PHASE (DEGREES)
2 3 4 6 8
8 6 4 3 2
WAVELENGTH (1000 KM.)
5 7.5 10 15
15 10 7.5 5
SPEED (°LAT./DAY)
NORTHWARD MOTION
SOUTHWARD MOTION

Figure 13b.

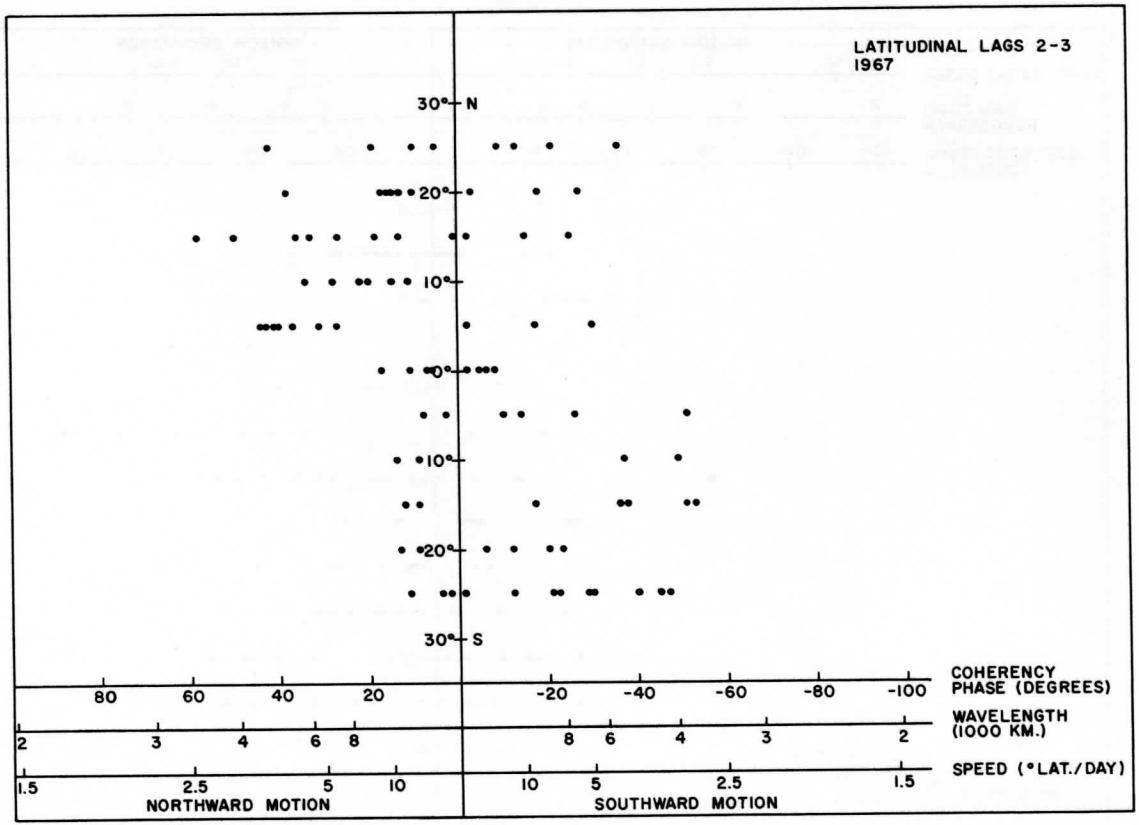
LATITUDINAL LAGS 2-3
1967
30° N
20°
10°
0°
10°
20°
30° S
80 60 40 20
-20 -40 -60 -80 -100
COHERENCY PHASE (DEGREES)
2 3 4 6 8
8 6 4 3 2
WAVELENGTH (1000 KM.)
1.5 2.5 5 10
10 5 2.5 1.5
SPEED (°LAT./DAY)
NORTHWARD MOTION
SOUTHWARD MOTION

Figure 14a.

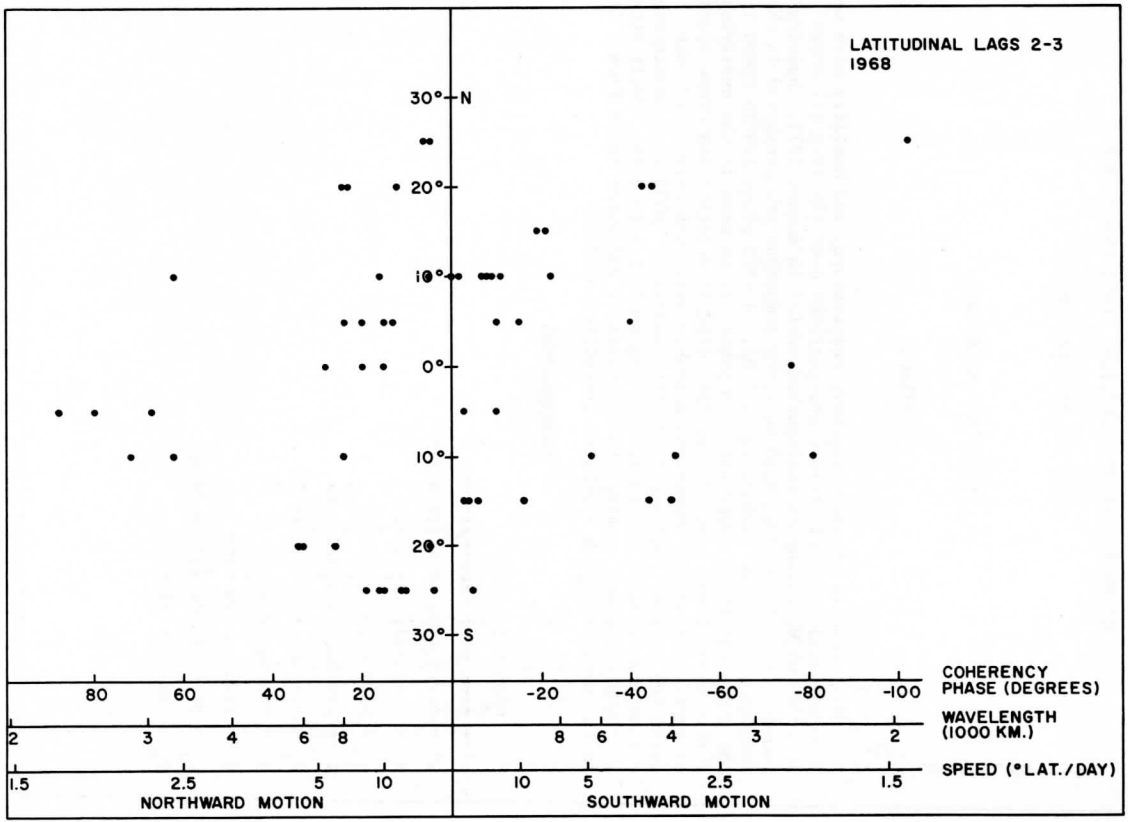
LATITUDINAL LAGS 2-3
1968
30° N
20°
10°
0°
10°
20°
30° S
80
60
40
20
-20
-40
-60
-80
-100
COHERENCY PHASE (DEGREES)
2
3
4
6
8
8
6
4
3
2
WAVELENGTH (1000 KM.)
1.5
2.5
5
10
10
5
2.5
1.5
SPEED (°LAT./DAY)
NORTHWARD MOTION
SOUTHWARD MOTION

Figure 14b.

OBSERVATIONS OF CONVECTIVE SCALE TURBULENCE OVER THE TROPICAL OCEAN

Elizabeth A. Berman

ABSTRACT

Measurements of wind velocity, temperature, and humidity were made from extended tethered balloon observations over the tropical ocean at 20°N, 60°W, during an undisturbed period in August 1973. Spectra of temperature and the down wind velocity component are presented in the frequency band from .000297 to .125 Hz. A -5/3 power law is found in the turbulent mixed layer and a -3 power law is seen in the overlying stable cloud layer. Spectra of the vertical velocity and cross spectra of vertical fluxes of momentum, sensible heat, and water vapor are presented in the frequency band from .000297 to .0178 Hz. Convective eddies are found in the wavelength region from 1 to 3 km. Their structure is found to depend on atmospheric stability and water vapor flux. It is the moisture which regulates convective activity.

NOMENCLATURE

V = mean wind speed

u' = down wind fluctuation

w' = vertical wind fluctuation

θ = vertical tilt angle

ϕ = horizontal angle

T = dry bulb temperature

T_v = virtual temperature

q = mixing ratio

ε = dissipation rate

σ_x = standard deviation of x

S_x = spectrum of x

1. INTRODUCTION

Properties of the tropical boundary layer are of great interest to the meteorology community today. It is important to have a detailed description of the oceanic trade wind region in order to understand the mechanism of convection and its interaction with the energy cycle of the general circulation.

Many studies have already been conducted in the effort to describe the tropical boundary layer. Most previous studies are limited by sampling techniques to describing mean statistics and transports of mean motion in the region above 100 meters. Aircraft measurements, however, have provided a few direct spectral estimates of turbulent transport in this region.

This study concentrates on describing turbulent statistics and transports in the Atlantic trade wind flow between 100 and 1000 meters. The data were acquired from a sea trial of the tethered balloon system designed for GATE. The trial was conducted during August 1973 from a ship located at 20°N, 60°W. The system, which will be described in detail later, measured the meteorological parameters every four seconds. The data were correlated and spectrally analyzed in the frequency range from .000297 to .125 Hz.

Description of the Trade Wind Region From Literature Survey

The vertical structure of the trade winds has been studied by Charnock, Francis, and Shepperd (1956) using pilot balloons, and by Holland (1972) and Augstein et al. (1973) using rawindsonde data from BOMEX and ATEX respectively. A wind speed maximum is generally found in the height range between 350 and 800 meters. There is very little vertical shear of the horizontal wind in this region. Below 150 meters, wind shear is large and positive. Above 900 meters, wind shear increases and is negative.

According to Malkus (1957), the location of the wind maximum is correlated with convective activity. She finds on days with strong convective activity the height of the wind maximum is near cloud base so there is little vertical shear in the lower cloud layer. On days with weak convective activity, the wind maximum is considerably lower than cloud base and the wind shear is negative in the cloud layer.

The statistical fluctuations of the down wind and vertical wind components were obtained from the pilot balloon study and also from aircraft measurements analyzed by Bunker (1973). Both studies show that $\overline{u'^2}$ tends to decrease to a minimum at cloud base and increases with height thereafter. $\overline{w'^2}$ has a maximum value near 150 meters and then decreases through the cloud layer. Vertical transport of horizontal

momentum is downward and decreases with height. Although the trends are the same in both studies, aircraft measurements show less height dependence, larger vertical velocity variance and smaller down wind variance. These differences are not surprising when the different types of observations and sampling rates are considered. While both studies were conducted during undisturbed atmospheric conditions, the balloons were released at 15 minute intervals and the aircraft sampled at much higher frequencies.

The tropical boundary layer can be divided into four layers of different convective regimes: the mixed layer, the transition layer, the cloud layer, and an inversion layer. The layers are defined by temperature and moisture profiles as shown in Figure 1, taken from Malkus (1957).

Below the condensation level (about 600 meters over tropical oceans) the air is well mixed by convective turbulence. Because of mixing, the temperature lapse rate is nearly dry adiabatic and the mixing ratio nearly constant.

The upper 1/5 of the mixed layer is called the transition layer. This layer is defined by a sudden increase in mixing ratio lapse rate and a slight stabilization in temperature lapse rate.

The presence of the transition layer depends on whether clear skies or cloudy skies prevail. Malkus finds that the transition layer is 100% present in clear areas and 45% present in cloudy areas, and during strong trade periods the transition layers are much thicker than for weak trade periods.

The cloud layer is above the condensation level. Cumulus convection is the major transport process in this layer. An inversion layer caps the cloud layer. In this layer the temperature lapse rate stabilizes and small scale turbulence is unable to penetrate and so is dissipated. The moisture lapse rate increases rapidly as the air dries out. These effects are stronger upstream than near the equator.

Temperature and moisture fluctuations have been studied by Bunker (1973) using aircraft measurements. $\overline{T'^2}$ has the largest values in the cloud layer. Sensible heat flux is positive and decreases in magnitude in the first 150 meters. Above this level, sensible heat flux is downward and increases with height. Moisture statistics show considerable variations between runs, but in general, water vapor flux is positive and decreases in magnitude with height as does moisture variance. Moisture statistics are only available beneath cloud base.

Mean mass and energy transports were investigated in the Atlantic Tropical Experiment (ATEX). The data were derived from simultaneous

radiosonde releases at three corners of a large triangle. The results of that study are shown in Figure 2, taken from Augstein et al. (1973). Fluxes at the sea surface were computed by the bulk aerodynamic formulas, but the vertical distribution of turbulent fluxes beyond that point could only be determined by budget box techniques.

It can be seen that both latent and sensible heat are transported equatorward in the boundary layer. The vertical transports by the mean motion are downward for both quantities. Sensible heat flux due to turbulent motion is much smaller than the transport by the mean motion, and the sign changes in the mixed layer as it did in the aircraft measurements described earlier. The turbulent latent transport is upward and of the same magnitude as the transport by the mean motion.

This brief literature survey has shown that while mean statistics and mean motions have been investigated in some detail, there is a growing need to investigate turbulent motions directly. A major weakness of currently available numerical simulation models is their inability to handle tropical convective scale motion.

Arakawa (1974) states that:

> The importance of clouds in climate modeling cannot be overemphasized...The difficulty in modeling clouds is partly due to our inadequate understanding of the function and dissipation process for the individual clouds...Almost all individual clouds are sub grid scale for the ordinary grid size of general circulation models...Therefore clouds need to be parameterized in terms of the dynamical hydrological quantities of resolvable scale.

One of the objectives of the GARP Atlantic Tropical Experiment was to observe the tropical boundary layer on a scale small enough to study convection, and to observe its behavior in steady and disturbed conditions. Radiosondes do not sample adequately to observe convective disturbances. Aircraft instruments sample rapidly but have not provided data series long enough to be statistically reliable for spectral analysis in wavelength regions greater than 1 km. The tethered balloon system designed for GATE eliminated these difficulties.

The GATE Intercomparison Sea Trial (GIST), while testing apparatus for GATE, provided meteorological measurements which begin to fill the gap in the description of trade wind turbulence.

The Data

The Boundary Layer Instrumentation System (BLIS) was developed by the Space Science and Engineering Center, University of Wisconsin-Madison

to meet the observational requirements of GATE. This system provides accurate measurements of dry bulb temperature, wet bulb temperature, pressure and the three wind components in the first 1500 meters of the atmosphere. It consists of a helium filled polyurethane coated nylon balloon, Dacron tether line, and as many as five Boundary Layer Instrumentation Packages (BLIPs). The line is winched out from shipboard. An illustration of the system is given in Figure 3 and a schematic of the BLIP is shown in Figure 4.

The BLIPs rest on plastic ball and ring joints fastened to the tether line. They are free to rotate in any direction. A three cup anemometer at the front of the package measures wind speed.

The vertical tilt of the package is measured by a slightly over-damped pendulum. The pendulum is a metallic sector suspended by the point and free to swing in its plane. The sector remains vertical when the package tilts slowly. Six concentric arcs near the circular edge are perforated with clear areas which are detected by photo-transistors. The six bit Gray output code is a measure of the tilt angle of the BLIP.

Design characteristics put limitations on the tilt sensing device. Resolution is limited to steps of 1/2 degree. High frequency fluctuations are filtered out by the damping fluid. Because of the pie-shaped nature of the pendulum, accelerations of the package caused by jerking of the tether line create torques which move the pendulum even when the package is not tilting. Despite these limitations which occur at high frequencies the tilt sensor provides excellent data on the low frequency range.

The horizontal direction is measured from magnetic north. One arm of the anemometer is magnetized and produces a sinusoidal signal. The amplitude of this signal at the time when the magnetized arm passes a fixed point on the BLIP describes the angle of the package from magnetic north. From the wind speed and two angles the complete wind vector can be found.

The middle section of the BLIP contains the electronics, dry bulb temperature, wet bulb temperature, and pressure sensors. The temperature sensors are shielded from heat conducted through the mount and from direct solar radiation.

The water for the wet bulb is supplied from a tank at the center of gravity of the package. Drift in the electronics is measured by reference signals derived from fixed resistors switched into the temperature circuits.

The tail of the BLIP has a cylindrical fin 20 cm. in diameter. It slides back and forth and is balanced so that the BLIP is horizontal when there is no vertical wind component. The fin causes some fish tailing in the horizontal during operation. A rapid sampling rate of 2 seconds is required to isolate this problem.

The overall length of the BLIP is 70 cm. and it weighs 675 grams with a full water tank, 50 cc of distilled water. The BLIS system is designed to operate continuously for 48 hours and in winds up to 30 knots.

All information collected by the BLIPs is transmitted to a Portable Data Acquisition System (PODAS) on the ship. Each BLIP is completely interrogated every four seconds. A complete interrogation includes: one dry bulb temperature reading, one wet bulb temperature reading, one pressure reading, and two wind vector readings, as well as calibration and identification information. The PODAS is capable of interrogating five BLIPs at the same time.

The resolution and range of the sensors is as follows:

	ABSOLUTE	RELATIVE	RANGE	SAMPLING FREQ.
Wind Speed	1 m/sec	.03 m/sec	.5 - 25 m/sec	2 sec
Pressure	.1 mb	.05 mb	850 - 1040 mb	4 sec
Dry Bulb	.1°C	.03°C	0° - 50°C	4 sec
Wet Bulb	.1°C	.03°C	0° - 50°C	4 sec
Wind Direction	1°		0° - 360°	2 sec
Tilt Angle	1/2°		0° - $\pm$18°4'	2 sec

The GATE Intercomparison Sea Trial (GIST) was performed during August 1973, with the U.S.A., U.S.S.R., and Mexico participating. The U.S.A. conducted their tests aboard the *Researcher*, which was located at 20°N, 60°W. Responsibility for each part of the United States portion of the sea trial is shown schematically in Figure 5.

Several different test modes were tried. One of the tests was constant level operation of multiple BLIPs at different levels. There were approximately 68 hours of testing in this mode with continuous testing for up to 24 hours and 44 minutes. Another experiment tested the profile mode of operation. In this mode, the BLIPs were moved up and down by winching the balloon. There were about 16 hours of testing in this area. Intercomparison tests were also made. Three BLIPs were flown at a distance of 1 meter apart in order to compare their operational accuracy. Soviet sondes were intercompared in the same way. In all of

the testing, about 85 hours and 47 minutes of data were collected at a sampling rate of once per 4 seconds.

The sea trial showed a few engineering and instrument handling changes were needed before GATE. The horizontal angle reading sometimes stuck at 120 degrees. This was caused by interference from the ship's radar.

The plastic water tank used in measuring the wet bulb temperature was exposed to the sun which caused the water temperature to be much warmer than the air temperature. At night the wet bulb readings were reliable. Unfortunately, in some cases the unusually high wet bulb readings were falsely attributed to leakage resistance across the thermistors. These thermistors were replaced and no absolute calibration information is available for them although the slope of the R versus T curves of these thermistors is the same as the calibrated ones.

The absolute calibration of the pressure shifted because the instruments were shipped by air to Miami. The pressure excursion was much higher than design limits, so the spring in the aneroid capacitor was apparently strained during flight.

In a few cases sunlight was allowed to leak into the tilt sensing apparatus causing interference with the light-emitting diodes. This problem can be eliminated by selecting only nighttime data for analysis.

The instrument packages vibrated severely due to aeolian tone vibrations on the tether line. Also, the pitch and roll of the ship jerked the line particularly at lower levels. These motions caused accelerations on the BLIPs other than gravity, which affected the pressure and wind related measurements in the high frequency range. The spectra of the wind speed show a narrow peak in the highest resolved frequency range. The effect is only over a narrow frequency band and is not removed by filtering because it is easily detected visibly. The tilt sensor, horizontal angle sensor, and pressure sensor are affected over a much broader frequency range. It was necessary to filter these parameters in the high frequency range and use resulting data sets only in low frequency analysis.

The sea trial identified potential instrument problems which might have arisen during GATE. Despite the difficulties mentioned, it also provided several days of excellent data which begin to fill the gap in the description of the turbulent structure of the tropical boundary layer.

2. DESCRIPTION OF THE WEATHER AND DATA PROCESSING TECHNIQUES

Two days of GIST data were selected for analysis: from 22:07 GMT August 5 through 18:03 GMT August 6 and from 15:55 August 7 through 14:34 GMT August 8. These days provided 43 hours of data which had several advantages over the rest of the data set.

The operating mode for both runs was constant level flight. This had an advantage over the profile mode because the time series were long enough to provide statistical reliability. However resolution of the vertical profiles is limited to only a few points.

Both days provided a total of 24 hours of nighttime operation. Therefore, any trouble with radiative heating or interference with the light-emitting diodes in the tilt sensor was eliminated.

General Weather

Satellite pictures taken by the U.S.A.F. vehicle #5528 on August 5, 6, 7, and 8 are shown in Figures 6-9. It is clear from these photographs that generally undisturbed conditions prevailed during the days selected for analysis. The mesoscale cellular convection is organized in "open cells" as discussed by Arakawa (1974). Open cells are characterized by clear polygonal areas surrounded by cumuliform walls. Arakawa states that open cells indicate a strong heat flux from the ocean to the atmosphere and little vertical wind shear. The cells range from 20 to 100 km in diameter.

To the east of the GIST data site there are cloud bands which are organized by a synoptic-scale disturbance off the coast of Africa. Arakawa explains that organized cloud bands are indicative of strong vertical wind shear.

The disturbance to the east is moving slowly into the GIST area. In fact, by the morning of August 8 the westward edge of the cloud bands is directly over 20°N, 60°W, so it is not surprising the local weather conditions as described by Garstang (1973) were different on the two days.

He finds that early August 5, the cloud cover was 2/8 Cu with 3/8 Ac on the east horizon, suggesting a weak disturbance. Winds were at 8 mps, relative humidity 83%, and pressure 1019.7 mb. By 10 o'clock, winds had increased to 9 mps, pressure dropped to 1017.3 mb and the ocean had a 1 meter swell. The top of the mixed layer was estimated to be at 440 meters, cloud base at 500 meters and the trade wind inversion at 3.5 km. There were light rains most of the afternoon. By 6 p.m., just before the start of the night run, wind velocity had dropped to 5 mps/80° and the showers were mainly in the west. Cloud base, estimated from the initial profile of the balloon system, was at 600 meters.

At the start of the August 7-8 flight, cloud cover was 3/8 Cu, 1/8 Ac, 2/8 Ci. Wind velocity was 5 mps/88° and the ocean had a 1 meter swell. From the initial profile cloud base was estimated at 700 meters. On the morning of the 8th, cloud cover had diminished to 2/8 Cu but the sky was very hazy and some white caps had developed on the ocean. Garstang's description implies that August 5-6 is less stable than August 7-8.

Data Processing

The GIST data were spectrally analyzed in the frequency range from 56 minutes to 4 seconds. Data processing was accomplished using a set of programs written in Fortran IV for use with the UNIVAC 1110 computer. These programs, documented in detail in another report by Berman (1974), performed the following tasks.

First, the BCD magnetic tapes received from CEDDA were decoded and searched for errors. Three types of errors were discovered and eliminated The timing mechanism on the PODAS required duplication of a complete word every one to two minutes. All duplicated values were easily removed. It was also noted that 4 to 8 second gaps occurred randomly throughout the data. These "holes" were filled by interpolation. Thirdly, all data points which were greater than six standard deviations from the mean were removed and filled by interpolation. Any data blocks in which more than 3 percent of the points were interpolated or in which more than three successive points were interpolated were not used in the analysis.

After the above corrections were completed, all data was stored on drum files in the UNIVAC 1110. The temperature and pressure data were left in engineering units, that is, the raw digital units received from the individual BLIPs. Where the operating range was limited, the conversion to meteorological units could be made with a simple straight line fit to the calibration data. However, when strictly meteorological parameters were required, for example to obtain temperature lapse rates and the wet bulb depression, it was necessary to make direct use of the engineering calibration data. These steps, which are easy to describe, actually took considerable effort. In some instances of incomplete documentation, the data could not be received.

The analysis program, described in detail in Appendix A, performed several steps in calculating spectral and cross spectral estimates. First it provided the gross statistics: means, variances and covariances of each series. Then all series were smoothed by means of a running mean and differencing technique to form filtered sets. The purpose of this filtering was to remove all low frequency components below the resolution of the lagged spectral analysis. Then the gross statistics were recalculated from the smoothed data sets.

Next the autocovariance and cross covariances were computed and Fourier transformed to provide spectral and cospectral estimates. A Hanning spectral window was applied to smooth the raw spectral estimates. Finally, all spectra and cospectra were corrected for filtering and block averaging where necessary.

The raw data from the GIST experiment consisted of wind components every 2 seconds and temperature and pressure measurements at 4 second intervals. All wind measurements were averaged over 4 second intervals. The spectra computed from 4 second wind speed measurements were not corrected for this averaging because, as will be seen, the frequency range it affected was dominated by ship motion.

The wind speed and temperature spectra were calculated in the high frequency range from .00208 to .125 cycles per second. This was done by dividing the raw data into 40 minute intervals. The maximum lag time was set at 4 minutes or 60 points. A 61 point running mean high pass filter was applied to each interval leaving only frequency components greater than 8 minutes. The gross statistics calculated from the smoothed data refer to a sampling time of 8 minutes.

The wind speed, temperature, horizontal angle, tilt angle and pressure were then subjected to spectral and cospectral analysis in the low frequency range from .000297 to .02083 cycles per second. The angles and pressure were first filtered to remove high frequency anomalies. All data sets were averaged over 28 seconds and divided into intervals of 4 hours and 40 minutes. The maximum lag time was 28 minutes or 60 data points. The 61 point smoothing process provided gross statistics for 56 minute sampling times. All low frequency spectra were corrected for the 7 point averaging.

A discussion of the confidence limits for the spectra presented in this report can be found in Appendix A.

The data used in this report represent a limited data set from the total collected during GIST. Surface observations, intercomparisons, rawinsonde ascents and radiation data from any of the ships were not yet available.

Before studying the results of analysis, the problem of balloon motion must be considered. The reliability of the tilt sensor is highly important in this work, as it is used in calculating all vertical transports It is realized that any significant balloon motion will affect the tilt sensing device greatly. This is a difficult problem, because there was no altimeter built into the BLIS system. It is hoped the discussion of the turbulent statistics and one dimensional spectra will establish confidence in the data set before the cross spectral analysis is presented. Appendix B discusses the problem of balloon motion in greater detail in terms of what should be seen in the cross spectral analysis if balloon motion were important.

3. MEAN AND TURBULENT STATISTICS

The data sets for the two days selected for analysis were divided into four groups according to varying wind and temperature profiles. Groups 1 and 2 are from August 5-6 and groups 3 and 4 from August 7-8. Table 1 presents the mean statistics for each group along with the time period during which each group was sampled. These groupings will be referred to throughout this report.

Groups 1 and 3 have lower wind speeds and show a wind maximum beneath cloud base. Groups 2 and 4 have increased wind speed reaching a maximum value at the highest height sampled. The temperature structure shows the mixed layer of groups 1 and 2 was less stable than groups 3 and 4, as suggested by Garstang's notes on the local weather conditions.

The mean heights were determined by triangulation using the amount of tether line winched out and the angle the line made with the horizontal plane. By examining the initial profile of the temperature as the line was winched out it was determined that the triangulation method was satisfactory. Pressure fluctuations indicated the absolute height of each package varied by 20 meters as the whole system moved up and down and the relative distance between BLIPs varied by 8 percent of the mean distance between BLIPs as the shape of the catenary was altered.

Experiments by Davenport (1961) and others have shown in general the statistics of the wind speed and the down wind component are interchangeable The down wind component in the GIST data set can only be resolved for low frequencies because of the high frequency filtering done on the angle measurements required to eliminate tether line vibrations. A comparison of low frequency wind speed statistics with the resolved down wind component was made and it was found they were the same. The down wind component was resolved only when computing cross correlations, to be discussed later. In this section, wind speed and down wind or u-component will be used interchangeably.

Table 2 shows the standard deviations of the wind components, u' and w', as a function of height. Also shown are the standard deviations of the azimuthal and vertical angles. σ_u represents the total standard deviation of the down wind component over the entire period from 4 seconds to 56 minutes. σ_w, σ_θ, and σ_ϕ, do not contain information for fluctuations more rapid than one minute because of the filtering techniques applied in that domain. They represent total standard deviations over the interval from 1 to 56 minutes.

σ_w was derived by assuming that it was related to σ_ϕ by the expression,

$$\sigma_w = \sigma_\theta V \frac{\pi}{180} \qquad (1)$$

TABLE 1. MEAN STATISTICS

GROUP 1

Total run time: 4 hr. 40 min.
Starting time: 19:00 local time August 5

height (meters)	wind speed (m/sec)	dry bulb temperature (°C)	mixing ratio (g/kg)	lapse rate (°C/100 m)
100	5.67	26.3	20.5	
				1.04
500	5.83	22.15	17.5	
				.80
600	5.77	21.35	15.9	
				.75
700	5.60	20.60		

GROUP 2

Total run time: 4 hr. 40 min.
Starting time: 02:00 hrs local time August 6

height	wind speed	dry bulb temperature	mixing ratio	lapse rate
100	7.12	26.15	20.0	
				1.03
500	7.29	22.05	17.4	
				.90
600	7.24	21.15	15.5	
				.70
700	7.44	20.45		

GROUP 3

Total run time: 4 hr. 40 min.
Starting time: 14:00 local time August 7

height	wind speed	dry bulb temperature	mixing ratio	lapse rate
300	5.42	25.00	--	
				.75
500	5.39	23.50	--	
				.90
600	5.39	22.60	--	
				.85
700	5.38	21.75	--	
				.62
1000	5.00	19.90	--	

TABLE 1 continued

GROUP 4

Total run time: 13 hr. (The three 4 hr. 40 min. runs shown here were averaged in Group 4.)

Starting time: 18:00 hr. local time August 7

height (meters)	wind speed (m/sec)	dry bulb temperature (°C)	mixing ratio (g/kg)	lapse rate (°C/100 m)
300	6.13	24.70	16.7	.75
500	6.11	23.20	--	.80
600	6.16	22.40	16.7	.80
700	6.17	21.60	16.2	.47
1000	6.10	20.20	--	
300	5.71	24.40	17.2	.80
500	5.73	22.80	--	.80
600	5.85	22.00	17.2	.70
700	6.04	21.30	16.5	.35
1000	6.92	20.25	--	
300	6.19	24.50	17.5	.80
500	6.20	22.90	--	.80
600	6.26	22.10	16.9	.70
700	6.28	21.40	16.4	.37
1000	6.53	20.30	--	

TABLE 2

group / height	1		2		3		4	
	σ_u		σ_u		σ_u		σ_u	
100 m	34		39					
300					32		27	
500	32		35		31		29	
600	33		35		32		30	
700	36		39		31		30	
1000					37		30	
	σ_θ	σ_w	σ_θ	σ_w	σ_θ	σ_w	σ_θ	σ_w
100 m	2.1	20	1.9	24				
300					3.7	35	3.0	31
500	2.6	27	2.2	28	3.5	33	2.7	28
600	1.8	18	1.8	22	2.3	21	1.8	19
700	1.5	15	1.5	20	2.2	21	1.8	19
1000					2.2	19	1.5	17
	σ_ϕ		σ_ϕ		σ_ϕ		σ_ϕ	
100 m	6.6							
300					9.0		7.4	
500	8.9		6.7					
600					10.4		3.9	
700								
1000					3.6		2.4	

UPPER: Standard deviation of longitudinal velocity, σ_u = cm/sec

MIDDLE: Standard deviation of vertical tilt angle (degrees) and standard deviation of vertical velocity (cm/sec)

BOTTOM: Standard deviation of azimuthal angle σ_ϕ degrees

While this expression is not strictly true, it requires only that the mean tilt angle be zero and that wind speed and tilt angle be statistically independent. Incorporating statistical dependence yields corrections smaller than the resolution of the instrument.

As can be seen from Table 2, σ_u is nearly constant with height in all cases. However, a slight minimum is suggested near cloud base for the more turbulent conditions of groups 1 and 2. Larger values of σ_u at 100 meters are not surprising when the source of turbulent energy at that height is considered. As will be discussed in detail later, the largest energy source beneath 150 meters is mechanical shear production. Lumley and Panofsky (1964) have shown mechanical production directly affects the downwind component. The large value of σ_u at 1000 meters in group 3 may also be related to increased vertical wind shear.

The effect of stability on vertical velocity fluctuations is very pronounced. The vertical velocity variance increases with height in the unstable mixed layer of groups 1 and 2 and decreases with height in the cloud layer and in the stable mixed layer of groups 3 and 4. There is a sharp decrease in σ_w between 500 and 600 meters in all cases.

Although less data are available for the standard deviation of the azimuthal angle, it appears that for this quantity, also, there is a noticeable decrease above cloud base. This tendency in both the vertical and cross wind variances is a manifestation of the change in structure between the well mixed turbulent layer and the overlying stable cloud layer. The ratio of σ_u/σ_w as a function of height brings out some very interesting properties as can be seen in Figures 10 and 11. The ratio in the layer between 300 and 500 meters approaches unity regardless of the mean wind speed, suggesting this portion of the mixed layer is isotropic.

Both beneath 300 meters and in the cloud layer the variance in the downwind component increasingly dominates. This feature is expected if the fluctuations are caused by convective activity. This important result will be examined and described in more detail later when the spectral estimates are presented.

The standard deviations of temperature and mixing ratio are given in Table 3 as a function of height. The standard deviation of the mixing ratio was calculated by assuming dry bulb and wet bulb temperatures were statistically independent. While this is not strictly true, the variations in the wet bulb temperature are far more important than the smaller dry bulb variances. This assumption also cut computer costs considerably. With this assumption, the standard deviation of the mixing ratio is given by

$$\sigma_q^2 = \left(\frac{Lq_s}{RT_w^2} + \frac{C}{L}\right)^2 \sigma_{TW}^2 + \left(\frac{C}{L}\right)^2 \sigma_T^2 \ . \qquad (2)$$

TABLE 3. Standard deviation of temperature (degrees C) and standard deviation of mixing ratio (g/kg) for each group as a function of height.

GROUP / HEIGHT	1	2	3	4	1	2	3	4
	σ_T				σ_q			
100 m	.05°	.05°	--	--	.40	.56	--	--
300	--	--	--	.10°	--	--	--	.60
500	--	.10°	.13°	.12°	.49	.40	--	.49
600	.10°	.15°	.14°	.14°	.44	.56	--	.55
700	.15°	.20°	.14°	.16°	.79	.97	--	1.07
1000	--	--	--	.19°	--	--	--	--

It can be seen from Table 3 the standard deviations of both temperature and water vapor are largest in the cloud layer. This was to be expected because of the structure of the mixed layer where both the potential temperature lapse rate and mixing ratio lapse rate are small. These properties inhibit thermal and moisture vibrations. In the cloud layer the vibrations increase as the lapse rates steepen. Also, the time series are long enough to sample both clear and cloudy areas, which increases temperature and moisture variations in the low frequency range.

Correlations between meteorological parameters will be considered in the context of the turbulent kinetic energy budget. For horizontally homogeneous incompressible flow, the turbulent kinetic energy equation is given by

$$\frac{\partial \bar{e}}{\partial t} = -\overline{u'w'}\frac{\partial V}{\partial Z} + \frac{g}{T_V}\overline{w'T'_v} - \frac{\partial(\overline{ew'})}{\partial Z} - \varepsilon \qquad (3)$$

where e is the turbulent kinetic energy per unit mass, ($e = u'u'/2$) and ε is the dissipation rate. In order, the terms on the right hand side represent mechanical shear production, buoyant energy production, divergent transport, and kinetic dissipation rate.

The momentum flux as a function of height is shown in Table 4. Momentum flux is downward and decreasing with height. The only exception to this is group 1, where momentum flux is upward above the wind maximum.

Mechanical energy production is dependent on the wind shear as well as momentum flux. Wind shear between 100 and 700 meters is negligible, so shear production is small in this region. Above 700 meters, the wind

TABLE 4. Mean velocity (m/sec) and $\overline{u'w'}$ (cm^2/sec^2)

group / mean height	1		2		3		4	
	V	$\overline{w'u'}$	V	$\overline{w'u'}$	V	$\overline{w'u'}$	V	$\overline{w'u'}$
100	5.67	- 54	7.12	-208				
300					5.42	-141	6.01	-125
500	5.83	- 51	7.29	-109	5.39	-109	6.01	-111
600	5.77	+ 13	7.24	-136	5.39	- 73	6.09	- 61
700	5.76	+ 21	7.44	- 37	5.38		6.16	
1000					5.00	- 57	6.52	- 54

shear is somewhat larger, but even here the magnitude of the shear production term is less than .1 cm^2/sec^3.

The vertical flux of sensible heat, water vapor transport, and buoyant energy production are presented in Table 5. The buoyancy term was estimated for the vertical flux of water vapor and sensible heat in the following way.

The vertical temperature is defined by

$$T_v = T\frac{(1 + q/\varepsilon)}{(1 + q)} \tag{4}$$

where ε is the ratio of the molecular weight of water vapor to the molecular weight of dry air. By expanding this equation, subtracting the mean, and correlating the fluctuations in virtual temperature with fluctuations in vertical velocity, it is found

$$\frac{g}{T_v}\overline{T'_v w'} \sim .61g\,\overline{q'w'} + \frac{g}{T_v}\overline{T'w'} \tag{5}$$

neglecting second order effects.

As can be seen from Table 5, sensible heat flux is upwards in the lowest part of the mixed layer. In the upper mixed layer and cloud layer, sensible heat is being transported downwards. The region of vertical convergence is between 100 and 500 meters on August 5-6 and beneath 300 meters on August 7-8. Water vapor flux is always upward, reaching maximum values near the top of the mixed layer where water vapor is accumulating. Beneath 400 meters, the atmosphere is positively buoyant, but in the cloud

TABLE 5

group / height	1 $\overline{w'T'}$	2 $\overline{w'T'}$	3 $\overline{w'T'}$	4 $\overline{w'T'}$
100 meters	+.11	+.32	--	--
300	--	--	--	-.22
500	-.63	-1.37	-.40	-.80
600	-.61	-1.15	-.72	-.82
700	-.57	-1.36	-.44	-.31
1000	--	--	--	-1.14
	cm/day	cm/day	cm/day	cm/day
100 meters	.29	.29	--	--
300	--	--	--	.38
500	.36	.34	--	.53
600	.28	.26	--	.16
700	.27	.20	--	.04
1000	--	--	--	--
	$\frac{g}{T_v}\overline{T'_v w'}$	$\frac{g}{T_v}\overline{T'_v w'}$	$\frac{g}{T}\overline{T'w'}$	$\frac{g}{T}\overline{T'_v w'}$
100 meters	+2.38	+3.09	--	--
300	--	--	--	+1.90
500	+ .43	-2.15	-1.31*	+1.05
600	- .12	-2.04	-2.38*	-1.60
700	- .04	-3.18	-1.46*	- .72
1000	--	--	--	-3.82*

* No moisture measurements were available so only the dry bulb temperature above was used.

UPPER: Sensible heat flux, $\overline{w'T'}$ (C° cm/sec)

MIDDLE: Water vapor transport (cm/day)

BOTTOM: Buoyant energy production (cm^2/sec^3)

layer energy is dissipated by the negative buoyancy of the stable atmosphere.

The transport of turbulent kinetic energy was computed using 3/2 the sum of the squares of the vertical and downwind turbulent energies as a measure of the kinetic energy, since the azimuthal component was not often available. The energy transport, $\rho\overline{ew'}$, is found to be upward beneath 600 meters in all groups. On August 7-8, the cloud layer has a downward energy transport. The divergence of the kinetic transport is shown in Table 6. There is a net energy gain in the layer between 550 and 650 meters for all cases.

The dissipation rate, ε, will be calculated in Section Four from the downwind spectra using the laws of the inertia subrange. The results from Section Four are plotted along with the average values for each of the terms on the energy equation in Figure 12. Also shown in Figure 12 are the results of Pennell and LeMone (1974) and Bunker (1973), both from aircraft measurements taken during an undisturbed period of tropical trade wind flow.

TABLE 6. Divergent energy transport $-\frac{\delta(\overline{ew'})}{\delta z}$ (cm^2/sec^3)

mean height \ group	1	2	3	4
300 meters	-.14	-.20		
400				0
550	+.18	-.42	+.21	+.18
650	+.11	+.12		+.41
850			-.11	-.23

The first term in the energy equation, the shear production, is not shown for the GIST data set because it was evaluated above 300 meters and found negligible. This agrees well with Bunker's results. Pennell and LeMone found a highly unusual and unexplained dissipative value for this term in the upper mixed layer. However, it is small and the trend agrees well with the other results.

The buoyancy term in the GIST data and Pennell and LeMone's data agree very well, showing positive buoyancy in the mixed layer and a sign change near cloud base. The buoyant production in Bunker's work was calculated from the dry bulb temperature only, which explains his much smaller and even dissipative values in the mixed layer.

The divergent transport term shows large discrepancies between studies. Pennell and LeMone obtain much larger values in the lower mixed layer. Bunker's data varies greatly with height and the GIST values are always small. These discrepancies may be due to different atmospheric conditions, however, it is more likely they are a result of computational errors. The divergence of turbulent transport is a very difficult term to measure because it requires taking the derivative of a triple moment.

The kinetic dissipation was computed from the laws of the inertial subrange in the GIST study and by Pennell and LeMone. The GIST values are smaller in the lower mixed layer, but are in general agreement with Pennell and LeMone. Bunker evaluated the dissipation by forcing the energy equation to balance. This technique resulted in values which were in disagreement with the other two studies and is assumed to be unsatisfactory. Bunker's values are not shown in Figure 12.

The energy budget does not balance in any of these studies. It is probable that above 500 meters the residual comes from the pressure transport term, $\delta/\delta z\ \overline{w'\ p'/\rho}$, which was not evaluated. Also, incorporation of radiative effects may improve the balance greatly.

Even with these differences, the trends in the terms of the kinetic energy budget are similar. This uniformity suggests it may be possible to parameterize the vertical structure of the mixed layer in terms of its bulk properties. If possible, it will be very useful for large scale modeling which does not have high vertical resolution.

Table 7 gives the horizontal sensible heat flux, $\rho c_p \overline{u'T'}$, at each level. Turbulent sensible heat is flowing downstream and has its maximum flux in the lower cloud layer. This suggests the origin of sensible heat is latent heat released by condensation. The production or dissipation rate of sensible heat cannot be determined because the data set is limited to one point in the horizontal plane, so no gradient heat flux can be resolved. The highly unusual result of upstream heat flux in group 3 is as yet unexplained.

TABLE 7. Horizontal energy flux (cal cm^{-2} sec^{-1})

group / height	1 $\rho c_p \overline{u'T'}$	2 $\rho c_p \overline{u'T'}$	3 $\rho c_p \overline{u'T'}$	4 $\rho c_p \overline{u'T'}$
100 m	$.05 \times 10^{-3}$	$.06 \times 10^{-3}$		
300				$.11 \times 10^{-3}$
500		.27	-.06	.19
600	.27		-.04	.26
700	.32	.55	+.05	.36
1000				-.04

4. SPECTRAL ANALYSIS

The spectra of the variance of the downwind component and dry bulb temperature as a function of frequency are presented in Figure 13-21 and 22-28 respectively. The spectral estimates are not normalized, and are plotted on log-log axes in order to observe the functional dependence of energy on frequency in the high frequency dissipative region of the spectrum. The triangular symbol on each graph represents a lower mean wind speed than the X.

The large peak in the downwind spectra at 8 to 10 seconds is due to ship roll. It decreases in magnitude with height as the ship's motion becomes less effective. The much smaller peak at 12 seconds is a result of the ship's pitching motion. A similar but much smaller peak is observed in the temperature spectra. The ship's motion causes some high frequency profiling, thereby sampling the lapse rate.

The downwind spectra show a shift in variance from high frequencies to low frequencies with increasing height. On August 5-6, an increase in wind speed increased the variance in the high frequency range. On August 7-8, the variance decreased with increased wind speed, most noticeably at the highest and lowest altitudes where the wind speed change was the greatest. The difference can be attributed to the different atmospheric structure of group 3.

Group 3 is the most stable of the four groups and also has the lowest mean wind speed. Later examination of the cospectra and cross spectra will show group 3 is the only one which does not exhibit organized convective activity. The organization which does exist is at much higher frequencies than for the other cases. Therefore, it is expected this group will show greater downwind variance in the high frequency portion off the spectrum.

The temperature variance also shows a shift from high frequencies to low frequencies with increasing height. In general, groups with lower wind speeds have less total temperature variance, indicating the temperature field is a passive scalar advected by the velocity field.

If a range of the spectrum exists where there is no production or dissipation of energy, turbulent flow is isotropic and energy can only be transported from one wave number to another at a constant rate. The energy in this so-called inertial subrange will be a function of wave number k and dissipation rate ε only.

Kolmogroff (1941) and others have studied the inertial subrange and have found by dimensional reasoning the energy spectra of the velocity components obey

$$E_u(k) = \alpha\varepsilon^{2/3} k^{-5/3} \tag{6}$$

where α is a universal constant. The inertial subrange is bounded from below by energy production and from above by viscous dissipation.

The inertial subrange for the temperature spectra is defined in a different way. Temperature fluctuations are transported by the velocity field. The inertial subrange for the temperature spectra is bounded from above by thermal diffusivity. The spectra for thermal fluctuations in this range are a function of thermal dissipation rate $-\overline{w'T'}\,\partial\theta/\partial z$ as well as ε and k. Therefore, by dimensional reasoning,

$$E_T(k) = \beta\varepsilon^{-1/3} k^{-5/3} \left[-\overline{w'T'}\frac{\partial\theta}{\partial z}\right] \tag{7}$$

where again, β is a universal constant. The low wavelength cutoff for an inertial subrange is generally found to be much less than the height of the sampling for a three dimensional spectrum. However, Gifford (1959) has shown one dimensional spectra obey the - 5/3 power law to much longer wavelengths. Taylor (1955) and later Van de Hoven (1956) and Zublovski (1962) have all shown one dimensional spectra obey the - 5/3 power law to wavelengths much larger than the height of the sampling.

A - 2/3 slope is plotted on the spectral plots rather than a - 5/3 slope because all estimates were multiplied by the frequency. With the exception of the spectra at 1000 meters, a - 2/3 slope is observed. The spectral estimates from August 7-8 show a much more extensive inertial subrange than August 5-6 estimates.

The universal constant, α, has been shown to be about .46 by Panofsky (1967) and others. Using this value and the assumption of frozen turbulence, i.e., $k = 2\pi f/V$, the dissipation rate ε was computed from equation (6). The results are given in Table 8.

TABLE 8. Dissipation rate, ε, (cm^2/sec^3) computed from equation (6).

group / height	1 ε	2 ε	3 ε	4 ε
100 meters	1.43	3.45		
300			3.81	1.68
500	1.45	2.39	2.71	1.42
600	1.27	3.06	2.06	1.20
700	1.00	3.54	1.36	1.11
1000			1.11	.47

One of the restrictions of the inertial subrange is that the dissiptation rate ε is constant. Lumley (1964) suggested in some cases there is a small leakage in the energy cascade due to buoyant dissipation removing energy from ε. His theory, including buoyant dissipation, predicts a -3 dependence on wave number. Returning to Table 1, it is apparent there is negative buoyancy above 500 meters, which is particularly large at 700 meters in group 2 and at 1000 meters in groups 3 and 4. A -2 slope (again, the spectral estimates are multiplied by frequency) is shown on the spectral plots at these heights. Leakage from ε due to negative buoyancy is readily apparent.

Willis and Deardorff (1974), using a laboratory model of an unstable planetary boundary layer, have also shown a -3 law is obeyed in a stable layer overlying a well mixed turbulent layer. They speculated that in this range,

$$E_T(k) = A\left(\frac{T}{z} + \frac{g}{c_p}\right)^2 k^{-3} \qquad (8)$$

and found $A = 4 \times 10^{-3}$. This equation was applied to the temperature spectrum of group 4 at 1000 meters and it was found that $A = 4.2 \times 10^{-3}$. Considering the rough way in which the temperature lapse rate was estimated, this value is in excellent agreement with the results of Willis and Deardorff.

In general, an extensive isotropic region following the - 5/3 law is observed in the stable region above cloud base. In the transition region both laws may be observed.

There are several possible physical explanations for observing both slopes. It may be the buoyant leakage is effective at lower frequencies closer to the input region of the spectrum and the smaller scales are not affected, and therefore obey a - 5/3 law. It was suggested by Willis (personal communication) that the height of the transition layer may have varied over the period of sampling so that both slopes were observed. Finally, it is possible the - 5/3 slope which is seen over a short range when the -3 slope is also present is not real, but caused by the pitch of the ship near that region of the spectra. It is noted, however, that Myrup (1969) has also seen both slopes occurring in the same spectrum near 600 meters.

It should be mentioned here Bolgiano (1956 and 1962) investigated the possibility of a buoyant subrange where eddy sizes are small enough to be uninfluenced by the shear, but yet not small enough to be affected by buoyancy. His theory predicts a - 11/5 power law for the energy spectrum and a - 7/5 law for the temperature spectrum. Lumley's theory better describes the behavior of the inertial subrange in the cloud layer of the tropical boundary layer.

The vertical velocity spectra and latitudinal velocity spectra are plotted in Figures 29-32 and 33-34 respectively. Each figure contains the estimates for all available heights of the respective group. The spectral estimates are multiplied by the frequency and normalized by dividing by the total variance. They are not plotted on a logarithmic scale, so the area under the curve represents the total energy density contained within a frequency range.

The wind and temperature spectra exhibit several prominent characteristics. There is a peak near 840 sec. (~5 km) in the velocity spectra of all groups except group 1. The temperature spectra also show this structure at 500 meters in group 2 and at greater heights in groups 3 and 4. Groups 1 and 4 have a noticeable increase in variance at 400 sec. (~2.4 km) whereas groups 2 and 3 show more structure at 250 (~1.5 km). Finally, at 100 sec. (~600 m), a large energy input is observed in all spectra and especially in the temperature spectra of group 3.

Examination of these characteristic peaks, their cause, and the atmospheric structure they suggest will be done in correlation with the cospectra and quadrature spectra of the meteorological parameters which describe the important energy transports.

5. CROSS SPECTRAL ANALYSIS

Figures 35 through 42 display the cosprectra and quadrature spectra of $\overline{u'w'}$, $\overline{w'T'}$, $\overline{q'w'}$, and $\overline{u'T'}$. Each figure shows the variations with height of the respective quantity within a group. The spectral estimates are multiplied by the frequency and normalized to represent correlations rather than covariances. The correlations are plotted versus the logarithm of the inverse wavelength computed from the assumption of frozen turbulence, $\lambda = V/f$.

The physical meaning of the cospectrum and quadrature spectrum can be seen in the following way. Mathematically, the cospectrum is the real part of the cross spectrum. Physically, it represents the amount of correlation between two quantities at a given frequency. A negative value implies the correlated quantities are out of phase by 180°. A positive value implies an in-phase relationship.

The quadrature spectrum is the imaginary part of the cross spectrum. Physically, it represents the lack of correlation between two quantities at a given frequency. If the quadrature spectrum is large, the quantities are out of phase by 90°.

An example of ideal convective cells is shown in Figure 44. In convective circulation, u' is 90° out of phase with w'. Near the bottom of the cell, w' leads u' by 90° (quadrature spectrum negative). Near the top, u' leads w' by 90° (quadrature spectrum positive). There is no cospectrum of $\overline{w'}$, no momentum transported, in this ideal circulation.

Temperature fluctuations are also shown in Figure 43. They are placed 180° out of phase with w'. Therefore, the cospectrum, $\overline{T'w'}$, is large and negative, and there is no quadrature spectrum. This type of circulation is "indirect" in the sense that sensible heat is transported downward so cold air rises and warm air sinks.

This is in fact the situation which arises in the warm moist tropical boundary layer. In this region, vertical water vapor transport is often large enough that positive buoyancy exists even though sensible heat is being transported downward. It can be seen from equation (5) that if water vapor flux is large enough, the flux of "virtual sensible heat" can be upward even though $\overline{T'w'}$ is negative. The condition for this is

$$.61\, T_v\, \overline{q'w'} > \overline{-T'w'} \qquad (9)$$

A brief survey of Figures 36-42 shows certain trends. The cospectra of $\overline{u'w'}$ indicate momentum flux is generally small. The cospectra are noisy, but show momentum flux is most important at wavelengths shorter than 800 meters. Vertical heat flux is generally downward above 300 meters for wavelengths greater than 1 km. At shorter wavelengths, heat flux is upward, particularly at the lower levels. Sensible heat is transported downstream in the long wavelength region, and water vapor is transported upwards.

The quadrature spectra of u'w', Figure 36, show very clearly u' and w' are close to 90° out of phase. The height relationship indicates motion in the 1 to 5 km range is convective or cellular in nature. The quadrature spectra of moisture flux and heat flux support this conclusion.

Only group 3 does not show convective organization. Group 3 has more Reynolds stress, particularly at short wavelengths, and the quadrature spectra in general show little structure. For these reasons, group 3 will be discussed separately.

The longest wavelength structure observed in the one-dimensional spectra of Section Four was at 840 seconds, which for the mean wind speeds observed during GIST lies between 5 and 6 km. Table 9 shows the cospectra, quadrature spectra, and phase relationships at several heights for this peak seen in groups 2 and 4.

The cross spectral estimates are much larger for group 2, but the phase relationships are similar for both groups. Momentum and sensible heat are transported downward with maximun values in the top of the mixed layer. Moisture is transported upward.

Figure 44 illustrates the structure which has developed in the 5 to 6 km range. The moisture flux is large enough to compensate for the

GROUP 2 at 840 sec ~ 6.3 km

height	C(uw)	Q(uw)	Phase	C(Tw)	Q(Tw)	Phase	C(uT)	Q(uT)	Phase	C(qw)	Q(qw)	Phase	σ_u^2	σ_w^2	σ_T^2	σ_q^2
100	-.158	-.123	35°	-.032	+.077	69°	+.050	+.201	76°	+.245	+.041	9°	.369	.250	.384	.564
500	-.125	+.030	12°	-.440	+.051	6°	+.234	-.057	14°	+.238	+.072	21°	.290	.407	.728	.382
700	-.069	+.102	63°	-.278	+.138	26°	+.123	-.093	37°	+.191	-.101	28°	.214	.365	.543	.552

GROUP 4 at 840 sec ~ 5.6 km

height	C(uw)	Q(uw)	Phase	C(Tw)	Q(Tw)	Phase	C(uT)	Q(uT)	Phase	C(qw)	Q(qw)	Phase	σ_u^2	σ_w^2	σ_T^2	σ_q^2
300	-.067	-.045	40°	-.118	-.022	10°	+.034	+.078	60°	+.049	+.033	34°	.283	.320	.305	.200
600	-.073	+.061	43°	-.219	+.006	0°	+.149	-.034	10°	+.077	+.011	8°	.295	.304	.408	.296
1000	-.043	+.134	70°	-.211	+.064	15°	-.022	-.088	80°	--	--	--	.301	.457	.399	--

TALLE 9. Spectral and cross spectral estimates for the lowest productive peak observed. All spectral estimates are normalized by dividing by the appropriate mean variance or covariance.

downward heat flux at 100 meters, but above that level it is not large enough to maintain convective activity. Instead, a wavelike motion is present in the mixed layer which transports momentum downward and sensible heat downward and downstream.

At 2.24 km wavelengths, a much larger effect is seen in the cross spectral estimates. This is especially true in groups 1 and 4, but is also seen to a smaller extent in group 2. The cross spectral estimates and phase relationships at 2.24 km are shown in Table 10.

The u' and w' wind components are out of phase by nearly 90°. T' tends to be in phase with w' and out of phase with u'. Through 500 meters, water vapor flux is large enough to outweigh downward heat transport, providing positive buoyancy as defined by equation (5). This situation is indicative of convective circulation as shown in Figure 45.

The cells slant slightly in order to transport momentum downward. The temperature fluctuations as indicated in Figure 45 are such that sensible heat is transported downward and downstream above 100 meters. Moisture fluctuations are not shown to avoid confusion. Moisture is in phase with vertical velocity and the transport is large enough below 500 meters to provide positive buoyancy.

The convective cell just described is clearly visible over a wide band of wavelengths. In group 2, the 1.5 km wavelength is the strongest. This wavelength is apparent to a much smaller extent in groups 1 and 4. At 1.5 km, the downward transport of sensible heat is much smaller and the air is more positively buoyant.

The physical picture which develops is depicted in Figure 46. Warm, moist air is rising from the air sea interface. Above cloud base, dry subsiding air is warming dry adiabatically in the clear areas. In the cloudy areas, cool moist air is rising.

The statistics in the convective region between 1.5 and 3 km have shown the cloud layer is negatively buoyant even though there is upward water vapor transport. Active clouds, however, must be positively buoyant. For this to occur, the clouds, while actually cooler than the air in which they are embedded, must be virtually warmer. An estimate of the increase in moisture content in the cloudy region necessary to make the cloud virtually warmer than the surrounding air is given by:

$$\text{increase in } q \geq 5.2 \times \text{decrease in dry temperature}$$

Computation of the fluctuation of virtual temperature above cloud base in the 2.24 km wavelength region showed the updraft regions averaged .02° virtually cooler than the surrounding air. This fluctuation is smaller

GROUP 1 at 2.24 km

height	C(uw)	Q(uw)	Phase	C(Tw)	Q(Tw)	Phase	C(uT)	Q(uT)	Phase	C(qw)	Q(qw)	Phase	σ_u^2	σ_w^2	σ_T^2	σ_q^2
100	+.075	-.230	71°	+.159	-.120	37°	+.155	+.065	23°	+.099	+.119	50°	.507	.543	.375	.388
600	-.067	+.283	78°	-.220	+.225	45°	+.263	-.131	26°	+.233	+.117	27°	.400	.442	.478	.517
700	-.013	+.221	84°	-.301	+.150	27°	+.200	-.200	45°	+.148	+.095	32°	.477	.595	.438	.378

GROUP 2 at 2.24 km

height	C(uw)	Q(uw)	Phase	C(Tw)	Q(Tw)	Phase	C(uT)	Q(uT)	Phase	C(qw)	Q(qw)	Phase	σ_u^2	σ_w^2	σ_T^2	σ_q^2
100	+.020	-.143	81°	+.095	-.035	20°	+.086	-.090	45°	+.161	-.009	3°	.361	.233	.435	.237
500	-.001	+.070	82°	-.190	+.091	25°	+.059	+.046	37°	+.158	+.027	9°	.243	.343	.377	.330
700	-.043	+.141	68°	-.176	+.054	17°	+.094	-.131	54°	+.092	+.014	9°	.260	.301	.409	.409

GROUP 4 at 2.24 km

height	C(uw)	Q(uw)	Phase	C(Tw)	Q(Tw)	Phase	C(uT)	Q(uT)	Phase	C(qw)	Q(qw)	Phase	σ_u^2	σ_w^2	σ_T^2	σ_q^2
300	+.011	-.116	85°	-.027	-.011	22°	+.020	-.029	55°	.143	-.030	12°	.243	.436	.280	.253
600	-.017	+.115	82°	-.135	-.006	0°	+.014	-.207	55°	.093	+.050	28°	.283	.435	.306	.480
1000	-.016	+.246	86°	-.258	+.136	28°	-.027	-.250	83°	--	--	--	.384	.425	.571	--

TABLE 10. Spectral and cross spectral estimates for the convective peak at 2.24 km. Spectral estimates are normalized by dividing by the appropriate variance or covariance.

than the resolution of the instruments, but even so, a slightly virtually cooler updraft region is not entirely unexpected. The mixing ratio variances have been slightly underestimated by assuming the dry bulb and wet bulb temperatures were statistically independent. It is also probable the clear dissipative regions are biased by the sampling techniques. Finally, it is possible and has been observed by Malkus (1957) that cool updrafts occur when small cumulus clouds temporarily "overshoot" their equilibrium.

Examination of two cases of trade cumuli passing over the BLIS system showed in both cases the cloud was "actually" cooler but "virtually" warmer than the surrounding air. A comprehensive investigation could not be undertaken because almost all cloud passes observed and logged occurred during the day when the wet bulb readings were unavailable.

Only group 3 does not show convective structure. The prominent peaks in the wind and temperautre spectra for group 3 are near 800, 200, and 100 seconds. The structure is difficult to determine from the cross spectral estimates because the coherence is low and moisture measurements are unavailable. However, it appears momentum flux is large and negative for all three periods and the structure is wavelike, similar to that shown in Figure 12.

The peak at 56 seconds in the downwind spectra at 600 and 700 meters of group 1 and 2 and at 1000 meters of group 4 has not been discussed. It is beyond the high frequency limit of cross spectral analysis. Moisture measurements for this frequency range are only available for group 2 at 600 meters. This moisture data suggests the velocity peak at 56 seconds is due to moisture buoyancy.

6. SUMMARY AND CONCLUSIONS

The GATE Intercomparison Sea Trial took place during a period of undisturbed trade wind flow. The trade cumulus observed during this period averaged 1 to 3 km in diameter.

Mean statistics indicate the region between 300 and 600 meters is a region of convergence. The level of convergence is determined by atmospheric stability. Sensible heat is transported into this layer from above and below and is exported downstream. Kinetic energy and moisture are also accumulated here. The variance of vertical velocity is largest in this layer whereas the variance of the downwind component is small.

Spectra analysis showed the upper mixed layer was isotropic in the high frequency range where the spectral energy was proportional to - 5/3 power of wave number. In the stable cloud layer, a -3 power law was observed following the prediction of Lumley. These power laws, together

with the regularity of the trends of the terms in the turbulent energy equation as a function of height, suggest a useful parameterization scheme can be developed.

Spectral and cross spectral analysis showed excitations were harmonic in nature. The periods excited were near 800 seconds, 400 seconds, 200 seconds, 100 seconds, and 50 seconds. The dominant mode for each depended on stability conditions.

The least stable run, group 1, showed dominant spectral peaks and convective activity at 400 seconds. Group 2 data was taken later in the evening when wind speeds had increased noticeably and the temperature lapse rate had stabilized slightly. The convective motion, while still large at 400 seconds, had built up significantly at 200 seconds. A peak at 800 seconds also developed, but was wavelike rather than convective in nature. Convective activity at 800 seconds was always suppressed by downward sensible heat flux which acts as a negative feedback mechanism to regulate it. It is interesting to note Bunker (1973) found 5 to 6 km (~800 seconds) was the average size of precipitating clouds in the BOMEX array.

In general, as stability decreases, longer wavelengths show convective activity. Convective activity is regulated by the water vapor transport. Positive buoyancy in the upper mixed layer is a result of layer upward water vapor transport. Condensation in the cloud layer provides sensible heat which is transported downward, regulating the buoyancy and acting as a feedback mechanism necessary to prevent increasing instability.

The fundamental frequency for the harmonics is as yet unknown. Satellite pictures show a large disturbance moving toward the GIST site from the east. Long belts of clouds precede the storm as can be seen in the fundamental frequency for the harmonics observed during GIST. If so, it has exciting potential for numerical modeling.

Arakawa (1974) explains cloud structure is often very regular in the trade wind region. He finds undisturbed regions of "open cell" structure are often located downwind from cloud bands generated from large scale disturbances off continental shores.

Before a useful parameterization scheme can be developed, more careful study of the small scale turbulence not only in the open cell region, but in the cloud band regions and disturbed regions is necessary. It is highly important to understand the affects of stability and wind structure on convective activity. The forthcoming GATE data will enable careful study of small turbulence in many different types of convective conditions. This will be a tremendous step forward in the effort to develop accurate models for large scale weather prediction.

ACKNOWLEDGEMENTS

I extend my utmost gratitude to Verner E. Suomi, whose inspiration and experience made this work possible. Many thanks also to David Houghton, Theodore Green, Donald Johnson, and Constance Blanchard, for their guidance and patience.

I would also like to acknowledge all those who were responsible for collecting and reducing the data set before I received it. A special thanks to SSEC Project Engineer Stan Burns for many long discussions on instrumentation and calibration. Thanks also to Ship's Scientist Michael Garstang for fruitful visits over the past year, and to CEDDA sending the data set to the Space Science and Engineering Center with no delay.

Without the constant support of my mother and husband I could not have completed this study. To them I will always be grateful.

This work was funded in part by NOAA Department of Commerce Contract number BOA 3-35314.

REFERENCES

Arakawa, A., 1974: JOC International Study Conference on the Physical Basis of Climate and Climate Modeling. Unpublished.

Augstein, E., H. Riehl, F. Ostapoff, and V. Wagner, 1973: Mass and Energy Transports in an Undisturbed Atlantic Trade-Wind. Monthly Weather Review, Vol. 101, No. 2, p. 110.

Berman, E.,1974: Computer Programs for Spectral Analysis of Stationary Time Series. Unpublished.

Blackman, R. B. and J. W. Tukey, 1958: The Measurement of Power Spectra. Dover Publications, Inc., New York.

Bolgiano, R., Jr., 1962: Structure of Turbulence in Stratified Media. J. Geophys. Research, Vol.67, p. 3015.

Bolgiano, R., Jr., 1959: Turbulent Spectra in a Stable Stratified Atmosphere. J. Geophys. Research, Vol. 64, p. 2226.

Bunker, A. F., 1973: Observations and Interpretation of Turbulence, Wind Variations and Showers in the Tropical Marine Boundary Layer. Technical Report, Woods Hole Oceanographic Institution, Massachusetts.

Charnock, H., J. R. D. Francis, and P. A. Sheppard, 1956: An Investigation of Wind Structure in the Trades: Anegada 1953. Phil. Trans., Vol. 249, pp. 179.

Davenport, A. G., 1961: The Spectrum of Horizontal Gustiness Near the Ground in High Winds. Quart. J. Roy. Meteorol. Soc., Vol. 87, pp. 194.

Garstang, M., 1973: Personal notes from GIST. Unpublished.

Gifford, F., Jr., 1959: The Interpretation of Meteorological Spectra and Correlations. J. Meteorol., Vol. 16, p. 344.

Holland, J. Z., 1972: BOMEX Sea-Air Interaction Program: Background and Results to Data. NOAA Technical Memorandum ERL BOM P-9, BOMAP Office, National Oceanic and Atmospheric Administration, U.S. Department of Commerce, Rockville, Md.

Kolmogorov, A. N., 1941: The Local Structure of Turbulence in Incompressible Viscous Fluid for Very Large Reynolds Numbers. Doklady ANSSSR, Vol. 30, p. 301.

Lumley, J. L., 1964: The Spectrum of Nearly Inertial Turbulence in a Stable Stratified Fluid. J. Atmos. Sci., Vol. 21, p. 99.

Lumley, J. L. and H. A. Panofsky, 1964: The Structure of Atmospheric Turbulence. Interscience Publishers, New York.

Malkus, J. S., 1957: On the Structure of the Trade Wind Moist Layer Technical Report, Reference No. 57-9, Woods Hole Oceanographic Institution, Woods Hole, Mass.

Myrup, L. O., 1969: Turbulence Spectra in Stable and Convective Layers in the Free Atmosphere. Tellus, Vol. XXI, p. 341.

Panofsky, H. A., N. Busch, B. Prasad, S. Harma, E. Peterson, and E. Mares, 1967: Properties of Wind and Temperature at Round Hill, South Dartmouth, Mass. Final Report, Grant No. DAA BO7-67-C-0035, Pennsylvania State University, University Park.

Pennell, W. T. and M. A. LeMone, 1974: An Experimental Study of Turbulence in the Fair-Weather Trade Wind Boundary Layer. J. Atmos. Sci., Vol. 31, p. 1308.

Taylor, R. J., 1955: Some Observations of Wind Velocity Autocorrelations in the Lowest Layers of the Atmosphere. Australian J. Phys., Vol. 8, p. 535.

Van der Hoven, I., 1957: Power Spectrum of Horizontal Wind Speed in the Frequency Range from .0007 to 900 Cycles Per Hour. J. Meteorol., Vol. 14, p. 160.

Willis, G. E. and J. W. Deardorff, 1974: A Laboratory Model of the Unstable Planetary Boundary Layer. J. Atmos. Sci., Vol. 31, p. 1297.

Zubkovski, S. L., 1962: Frequency Spectra of the Horizontal Wind Speed Component Close to the Ground. Izvestia ANSSSR, Geophys. Ser., No. 10, p. 1425.

APPENDIX A: The Analysis Program

The procedures followed in the analysis program were based on methods of spectral and cospectral analysis for discrete stationary time series described by Blackman and Tukey (1958). This approach can be described as follows.

Start with N equally spaced terms of a time series x_i. The time difference between each point is Δ and the total time length of the series is ΔN.

The serial autocovariances, $C_{xx}(k)$, were co puted for all lag times $\tau = 0, \Delta, 2\Delta, \ldots k\Delta \ldots L\Delta = M$ according to the formula

$$C_{xx}(k) = \frac{1}{N-k} \sum_{i=1}^{N-k} (x_i - \bar{x})(x_{i+k} - \bar{x}) \qquad 0 \leq k \leq L \tag{A1}$$

where L is the maximum number of lag times, $\bar{x}$ is the mean of the series computed from

$$\bar{x} = \frac{1}{N} \sum_{i=1}^{N} x_i \tag{A2}$$

and $C_{xx}(0)$ is the variance of the series.

The spectrum is the Fourier transform of the autocovariance function. For a stationary process $C_{xx}(\tau)$ is symmetric in τ. The spectrum $S_{xx}(f)$ is then an even function of frequency, so it is only necessary to calculate it over the range $0 \leq f \leq 1/2\ \Delta$. However, to preserve the Fourier transform relationship, it is necessary to double the power associated with each frequency. Therefore, the algorithm used was

$$S_{xx}(f) = 2\Delta \{C_{xx}(0) + 2 \sum_{k=1}^{L-1} C_{xx}(k)\, W(k) \cos 2\pi fk\Delta\} \tag{A3}$$

W(k) in this equation is the hanning spectral window. It has the properties that

$$W(k) = \frac{1}{2}\left(1 + \cos \frac{\pi k}{L}\right) \quad k = 0, \ldots L \tag{A4}$$

and

$$W(k) = 0 \quad k > L \tag{A5}$$

The procedure for handling two different stationary time series is similar. The cross covariance is defined as

$$C_{xy}(\pm k) = \frac{1}{N-|k|} \sum_{i=1}^{N-|k|} (x_i - \bar{x})(y_{i\pm k} - \bar{y}) \quad k=0,L \tag{A6}$$

The cross covariance is not necessarily symmetric but can be separated into even and odd components for the purpose of Fourier transforming.

$$\begin{aligned} C_{xy}(k) &= \frac{1}{2}\left[C_{xy}(k) + C_{xy}(-k)\right] + \frac{1}{2}\left[C_{xy}(k) - C_{xy}(-k)\right] \\ &= EV_{xy}(k) + OD_{xy}(k) \end{aligned} \tag{A7}$$

The cospectra and quadrature spectra are then given by

$$S_{xy}(k) = 2\Delta\{EV_{xy}(0) + 2 \sum_{k=1}^{L-1} EV_{xy}(k)\, W(k) \cos 2\pi fk\Delta\} \tag{A8}$$

and

$$Q_{xy}(k) = 4\Delta \sum_{k=1}^{L-1} OD_{xy}(k)\, W(k) \sin 2\pi fk\Delta \tag{A9}$$

respectively, where W(k) is again the hanning spectral window. Further, the phase is given by

$$\text{Phase } (k) = \text{ARCTAN}\left[-\frac{Q_{xy}(k)}{S_{xy}(k)}\right] \tag{A10}$$

and the coherence by

$$COH^2_{xy}(k) = \frac{S^2_{xy}(k) + Q^2_{xy}(k)}{S_{xx}(k)\ S_{yy}(k)} \tag{A11}$$

Filtering Techniques

All data sets were subjected to high pass statistical filtering. The filter was designed to remove all frequencies lower than $f = 1/2\Delta M$, the lowest frequency resolved by the above technique. It was done by subtracting an L + 1 term running mean from each data point. As before, L is the number of lags and $M = \Delta L$ is the maximum time lag. The filtered data set is defined by

$$z_i = x_i - \frac{1}{L+1} \sum_{j=-L/2}^{L/2} x_{i+j} \qquad i = (\tfrac{L}{2} + 1) \ \ldots \ (N - \tfrac{L}{2}) \tag{A12}$$

where z_i is the ith value of the filtered data set corresponding to x_i of the original series. The number of points in the filtered series is reduced by L.

The response function of the high pass filter is

$$H(f) = 1 - \frac{2}{L+1} \sum_{n=1}^{L/2} \cos 2\pi nf\Delta \tag{A13}$$

H(f) represents the ratio of amplitude after filtering to that before filtering at each frequency point.

The spectra of the smoothed series are corrected for filtering by dividing by $|H(f)|^2$.

$$S_{xx}(f) = \frac{S'_{xx}(f)}{|H(f)|^2} \tag{A14}$$

Low pass filtering was done on measurements of tilt angle and horizontal angle to remove high frequency oscillations due to instrument characteristics. The response function for the low pass filter was

$$H(f) = h_0 + \sum_{n=1}^{3} h_n \cos 2\pi fn\Delta \tag{A15}$$

where $h_0 = .4674$

$h_1 = .2275$

$h_2 = .0381$

$h_3 = .0007$

This function is graphed in Figure A.1. All data subjected to this filtering were used only in low frequency analysis.

Confidence Intervals

The hanning spectral window reduces the variance of the spectral estimates. The variance ratio,

$$\text{variance ratio} = \frac{1}{T}\int_{-\infty}^{\infty} W^2(\tau)\, d\tau \qquad \text{(A16)}$$

represents the proportional reduction in variance as a result of using a smoothed spectral estimator. For the hanning spectral window, the variance ratio is .75 M/T = .75 L/N.

The ratio of the smoothed spectral estimates to the actual spectral estimates is approximately distributed as a χ^2_ν, so that the number of degrees of freedom is $\nu = 2.667$ T/M. The confidence intervals for both frequency ranges discussed in this work are the same because the number of degrees of freedom is the same. The confidence for several ranges calculated from a chi square distribution function are listed in Table A.1.

	95%	90%	80%
$\frac{\nu}{\chi\ (1-\alpha/2)}$	.61	.66	.72
$\frac{\nu}{\chi\ (\alpha/2)}$	1.94	1.74	1.53

Table A.1

These limits are for one spectral estimate. When a number of independent spectral estimates are averaged together, the confidence limits narrow rapidly because the number of degrees of freedom is proportional to the number of independent estimates.

The number of independent downwind and temperature spectra computed and averaged in the high frequency range and plotted in this study are listed in Table A.2.

Height \ Group	Down Wind				Temperature			
	1	2	3	4	1	2	3	4
100	6	6			4	6		
300			6	18				
500	6	6	6	9	4	6	6	16
600	6	6	6	18	4	6	6	16
700	6	6	6	18	4	6	6	10
1000			6	18			5	15

Table A.2. # of Downwind and Temperature Spectra Averaged in the frequency range from .00208 to .125 Hz.

All spectra and cross spectra plotted in the low frequency range are for one independent run, except for Group 4. The number of spectra averaged and plotted in Group 4 is given in Table A.3.

The confidence intervals are not shown on the spectral plots in this study because of the confusion which would result in having different error bars for each spectrum in a graph.

Height	u'^2	T'^2	w'^2	ϕ'^2
300	3	2	3	0
500	3	3	3	0
600	3	3	3	3
700	3	1	0	3
1000	3	2	2	3

Table A.3

Methods for evaluating confidence intervals for coherence and phase estimates are discussed in detail by Jenkins and Watts (1968). They assume that estimates of arctanh $[COH^2(f)]$ and tan [Phase (f)] can be approximated by a Normal distribution. Confidence intervals for the phase angle for 24 degrees of freedom are given in Table A.4 as a function of $COH^2(f)$.

COH^2	± 95%	90%	80%
.6	± 15°	12°	± 8°
.5	± 18°	15°	± 10°
.4	± 22°	18°	± 12°
.3	± 27°	22°	± 15°
.2	± 34°	± 27°	± 19°

Table A.4. Confidence limits for phase angle as a function of coherence.

Individual coherence estimates can be computed from Tables 9 and 10 for the frequency bands of interest. A rough estimate of the 90% interval on the phases discussed in this text is ± 20°.

The resolution of the sensors limits the precision of the results. The precision of a correlation between two different quantities is only as good as the precision of the worst quantity. The tilt sensor is limited to resolving the tilt in steps of 1/2°. Assuming a mean wind speed of 6 m/sec, the resolution of vertical velocity fluctuations is ± 3 cm/sec. However, all vertical velocity fluctuations are averaged over 14 points so, providing the errors are Normally distributed around zero, the resolution becomes $\pm 3/\sqrt{13}$ cm/sec or ± .83 cm/sec. A similar result is obtained for the 14 point averaged downwind components. Therefore, the resolution of the momentum flux is

$$\overline{u'w'} \pm \frac{.83\ u'}{\sqrt{600}} \pm \frac{.83\ w'}{\sqrt{600}} \pm \frac{.69}{\sqrt{600}}$$

or approximately

$$\overline{u'w'} \pm 1.5\ \frac{cm^2}{sec^2}.$$

The resolution of the temperature sensor after 7 point averaging becomes ± .008°C, so the resolution of vertical flux of sensible heat is

$$\overline{w'T'} \pm \frac{.83\ T'}{\sqrt{600}} \pm \frac{.008\ w'}{\sqrt{600}}$$

or approximately

$$\overline{w'T'} \pm .01°C\ cm/sec.$$

A quantitative description of balloon motion was not available; therefore, error limits due to this effect could not be obtained.

APPENDIX B

The problem of balloon motion is a difficult one. It was thought at first the pressure sensing device could act as an altimeter by assuming P would remain constant at constant height. The pressures were analyzed in the same way as the vertical tilt, i.e. the data was low pass filtered and averaged over 28 second intervals. After the 61 point smoothing function was applied, the standard deviation of pressure was calculated. Some results for groups 3 and 4 are shown in Table B.1.

height	group 3	group 4
1000 m	1.6 mb	1.5 mb
600	1.4	1.2
300	5.3	5.2

Table B.1

The acceleration forces caused by the tether line had not been removed at the lowest levels by the filtering, however, it appeared the highest BLIPs were operating satisfactorily. Spectral analysis unfortunately resulted in noise. Several other filters were tried, hoping removal of more high frequency noise would develop meaningful spectrum in the low frequency range discussed in this study. Averaging the pressure over 1/2 hour intervals produced realistic daily trends, but any attempt to use the pressure in the frequency range of interest here was abandoned. The device was much too sensitive to external forces to be useful.

Even though this method of attack failed, balloon motion can still be detected if it exists as is shown by the following Gedenken experiment.

In order for the balloon to change altitude, the velocity field must change. The altitude change would result in fictitious changes in the wind components and temperature field. These fluctuations would be in phase with each other and in the same direction at all heights. All possible changes in the wind field are depicted in Figure B.1. The double arrows show the real change and the single arrows the fictitious, forced changes in each case. In no case can the forced change be larger than the real change.

If the vertical velocity increases, the balloon rises. This causes an apparent increase in horizontal velocity and downward vertical velocity. The apparent downward vertical velocity cannot be large enough to outweigh the upward velocity causing the initial motion. Therefore, cross correlation of the fluctuations in the velocity components shows they are in phase and result in the appearance of a fictitious upward momentum flux.

If the horizontal velocity increases, the balloon falls in altitude. This results in an apparent upward vertical velocity and decreasing horizontal velocity. Again, the decrease cannot be larger in magnitude than the initial increase forcing the motion, and again, fluctuations are in phase and positively correlated.

Further identification of balloon motion can be done by considering the affect on vertical and horizontal heat flux. In the first case of changing vertical motion, heat flux would appear to be downward and upstream. In the second case, heat flux would be upward and downstream. Finally, it is clear that if balloon motion is causing fictitious momentum and heat fluxes, the effect should be the same at all heights with only the magnitude changing.

Comparing the results of this Gedenken experiment with the cross spectra of the GIST data shows the above cases do not exist. In fact, in most cases the velocity components were out of phase over most of the frequency range studied. Also, the direction of the energy transports varied with height. The only remaining possibility is a combination of increasing horizontal wind and decreasing or downward vertical wind. In this case the actual downward transport of momentum would be reduced in magnitude and the downward sensible heat flux increased in magnitude, but the trends would be the same as the actual conditions. This may be a factor in the 840 second peak observed, but is not observed in the higher frequency range.

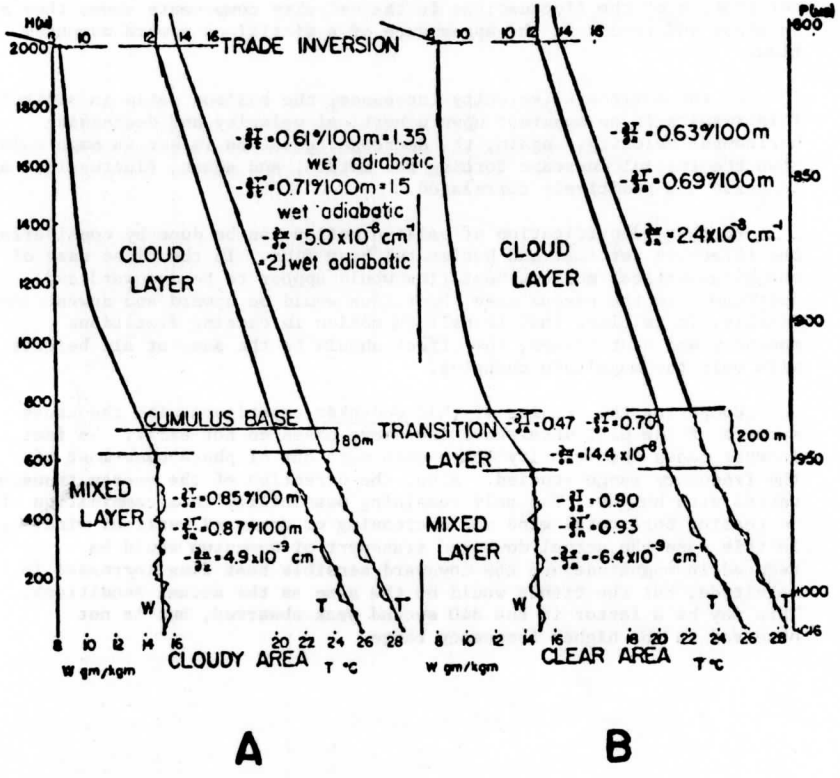

Figure 1. Average soundings for April 1946 Woods Hole expedition during a strong trade, compiled by taking the average temperature, T, virtual temperature, T*, and mixing ratio, w, at the base of each layer, the average lapse rate within the layer of each property and the average vertical thickness of the layer. Height in meters is the ordinate. Figure 1A is the average cloudy area sounding (compiled from nine individual soundings) and Figure 1B is the average clear area sounding (compiled from nineteen individual soundings). Generally one or more soundings of each type were made on a given day. (From Malkus, 1957.)

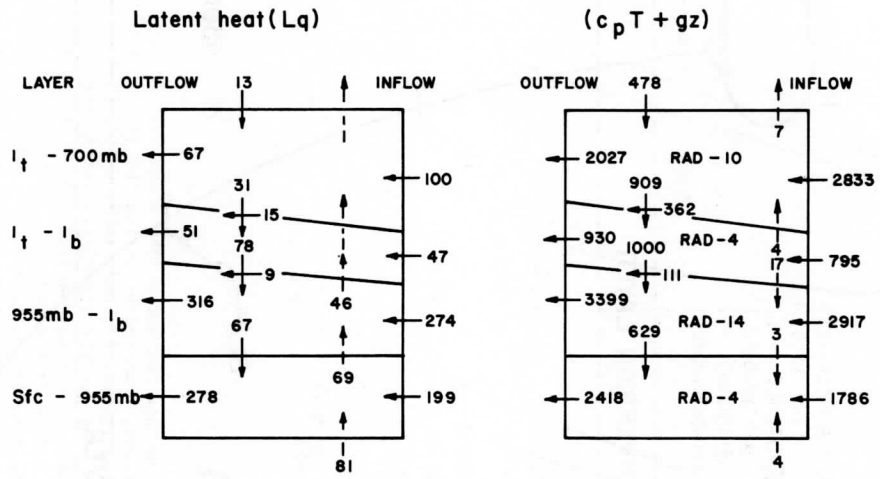

Figure 2. Budgets of latent heat (10^{16} cal/day), and of enthalpy plus geopotential energy (10^{16} cal/day), for the subcloud layer, the cloud layer, the inversion layer, and the layer above the inversion up to 700 mb for the ATEX triangle, Feb. 7-12, 1969. Full arrows indicate transports by the mean motion; broken arrows, the residual turbulent fluxes. Radiation sink is indicated in the sensible heat budget; the net latent heat release is zero for the moisture budget. (From Augstein, 1973.)

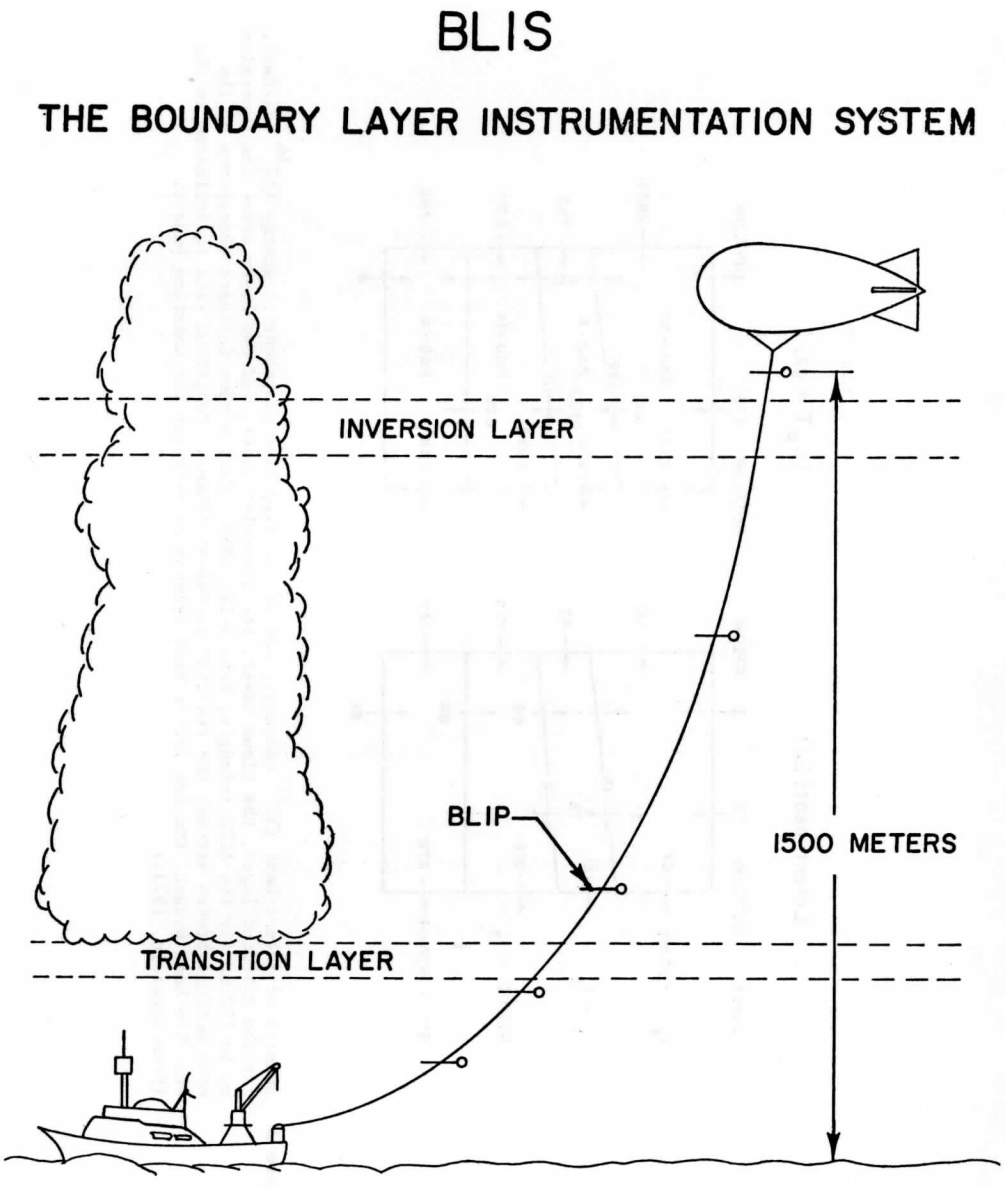

Figure 3. Schematic of the BLIS as it operated during the GATE Intercomparison Sea Trial.

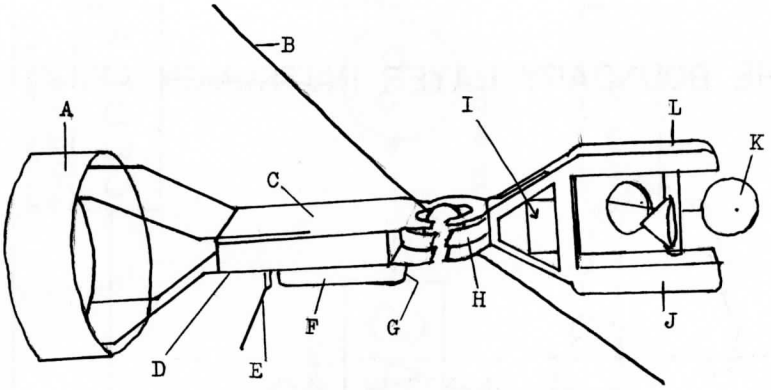

Figure 4. Schematic of the BLIP.

A. Titanium tail
B. Tether line
C. Windav and logic circuits
D. Capacitor and Resistor controlled oscillators
E. 420 MHz. dipole
F. Radiation shield
G. Wet and dry bulb thermistors
H. Water tank
I. Sony diode circuitry and tilt indicator
J. Batteries
K. Anemometer
L. Sony magnetic diode

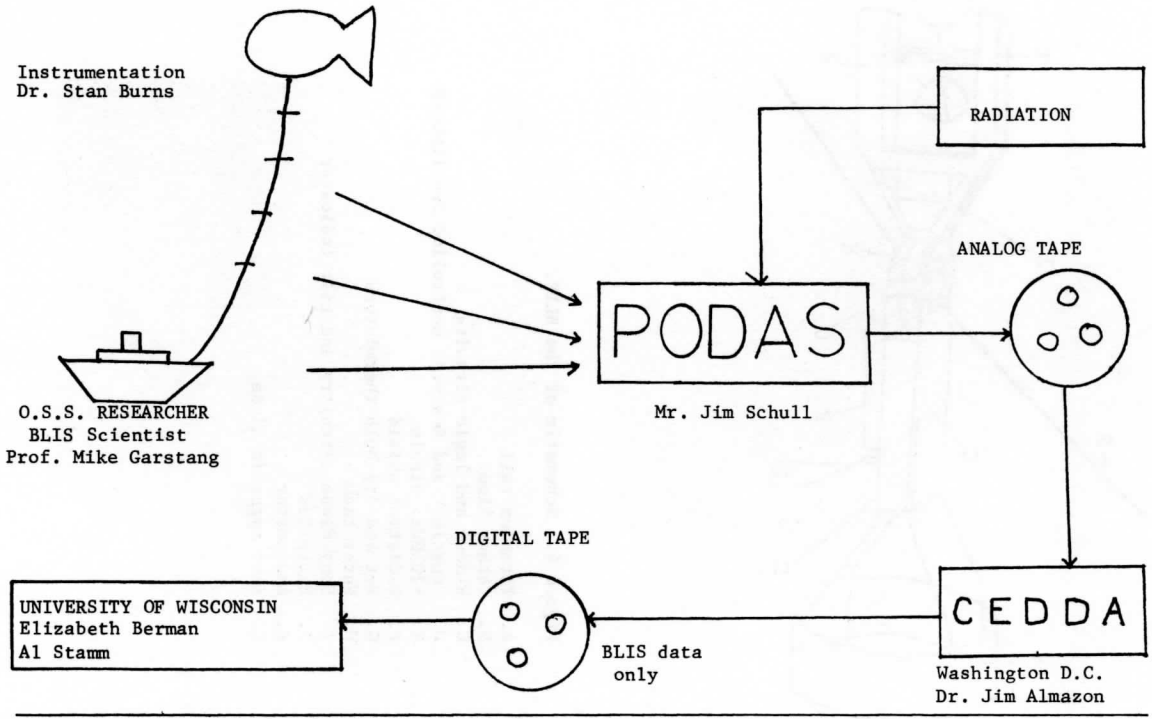

Figure 5. Flow chart of data handling and personnel for BLIS data acquired during GIST.

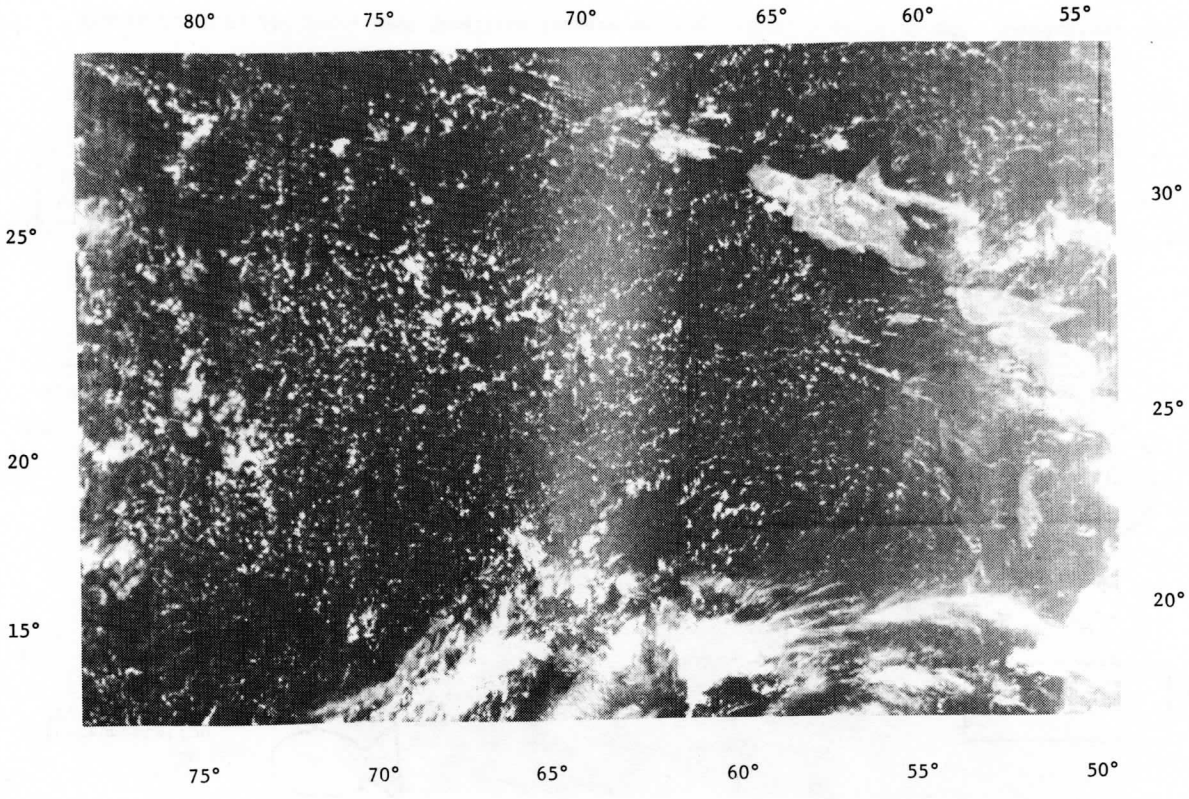

Figure 6. U.S. Air Force DMSP Satellite imagery recorded August 5 at 16:30 GMT. Resolution, .3nm.

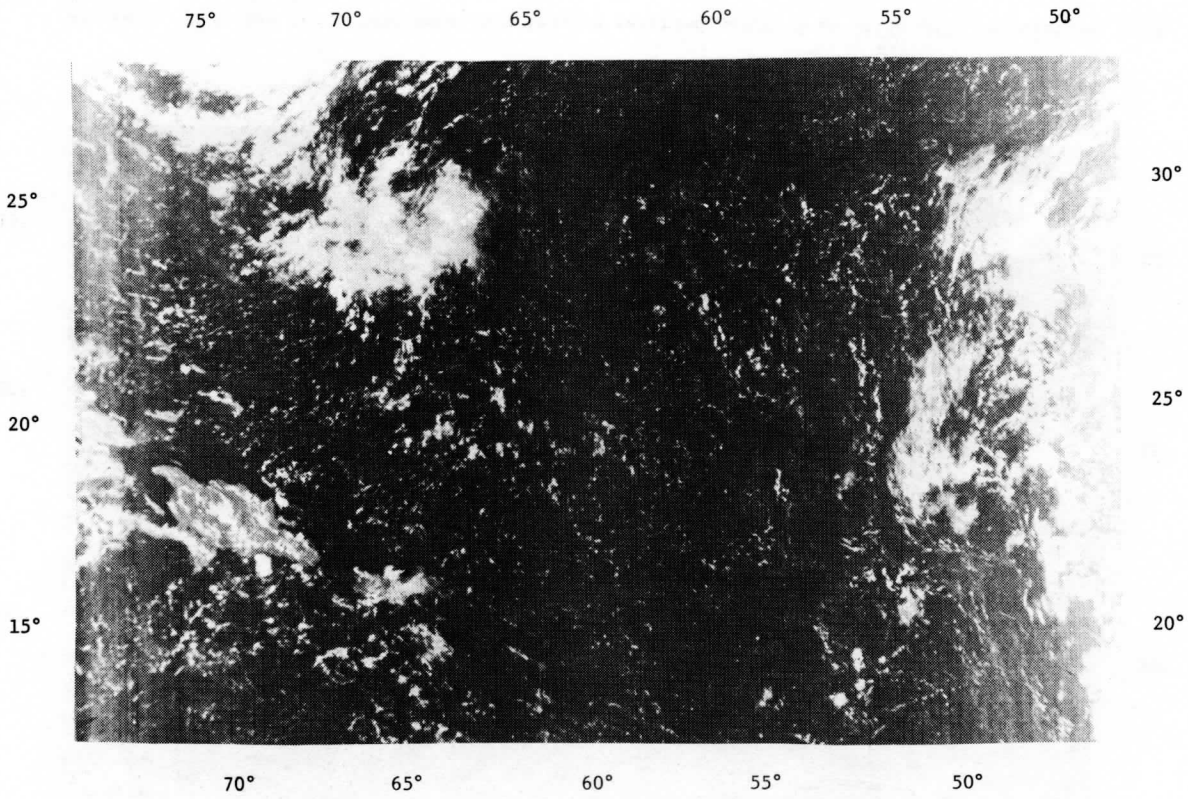

Figure 7. U.S. Air Force DMSP Satellite imagery recorded August 6 at 16:20 GMT. Resolution, .3nm.

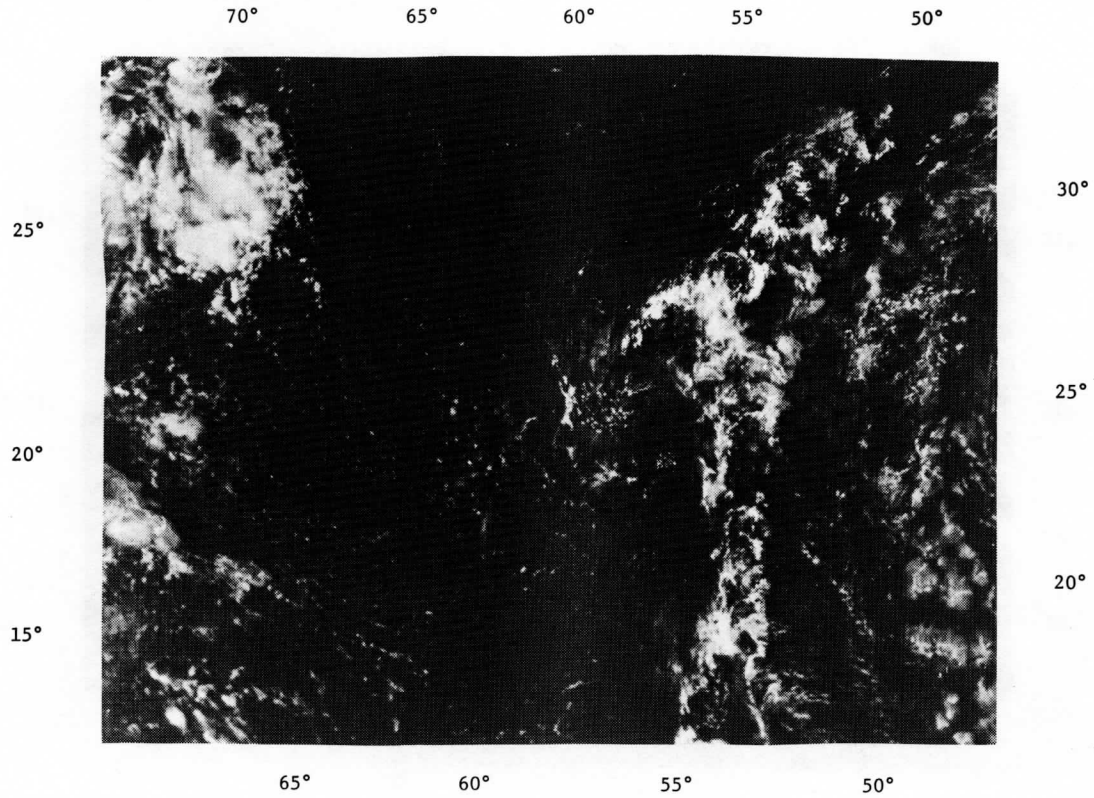

Figure 8. U.S. Air Force DMSP Satellite imagery recorded August 7 at 16:00 GMT. Resolution, .3 nm.

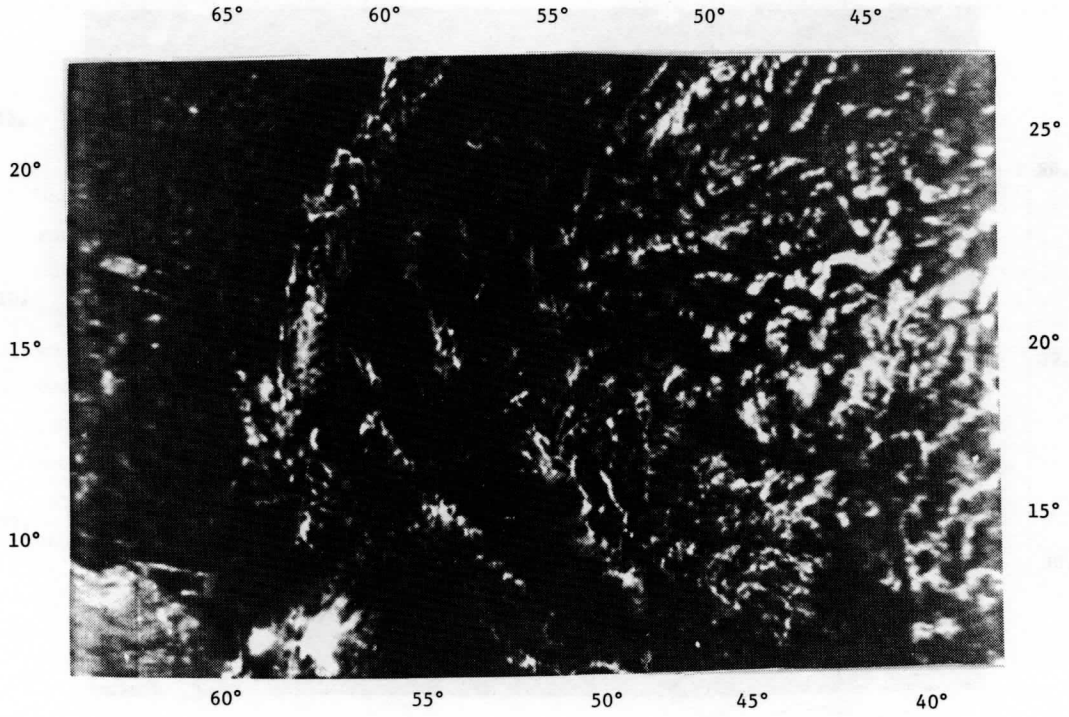

Figure 9. U.S. Air Force DMSP Satellite imagery recorded August 8 at 15:45 GMT. Resolution, 2 nm.

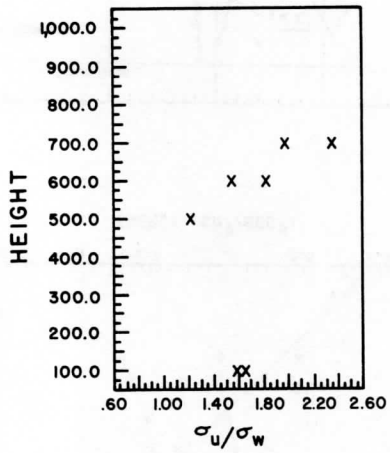

Figure 10. Ratio σ_u/σ_w calculated from Groups 1 & 2. Turbulent mixed layer.

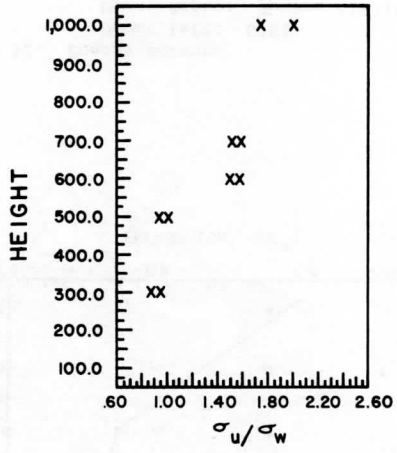

Figure 11. Ratio σ_u/σ_w calculated from Groups 3 & 4. Stable atmosphere.

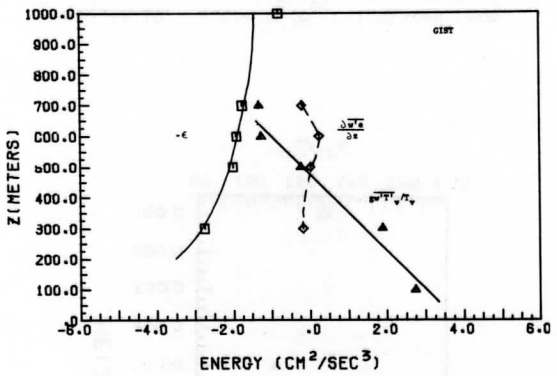

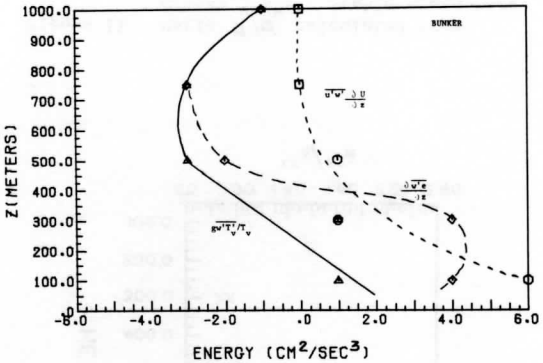

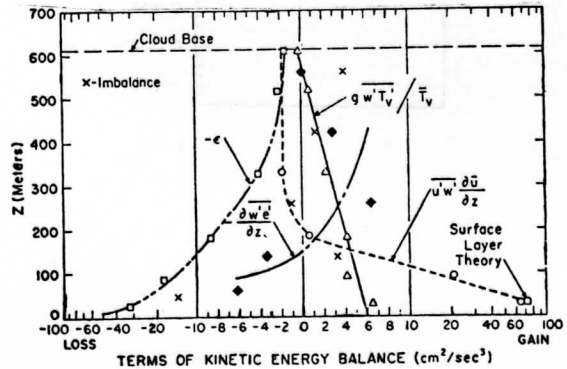

Figure 12. Energy Balance
Upper left: GIST
Upper Right: Bunker (1973)
Lower Left: Pennel and LeMone (L974)

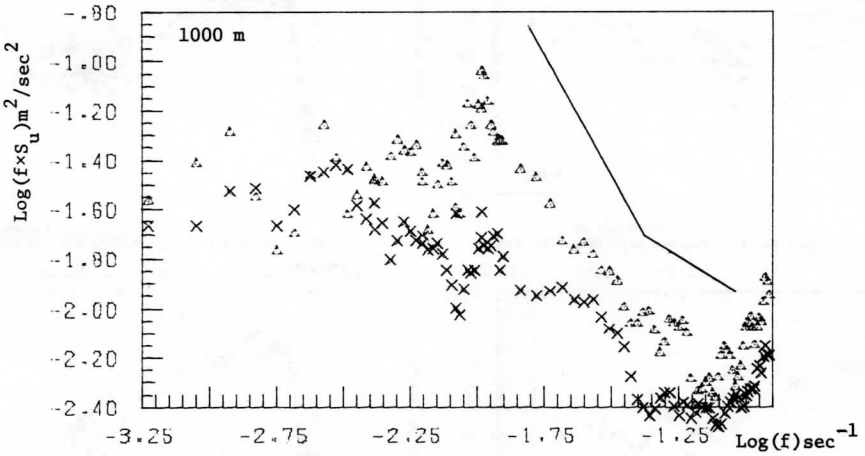

Fig 13. Down wind spectra of group 3 (Δ) and group 4 (x) at 1000 meters.

U SPECTRUM

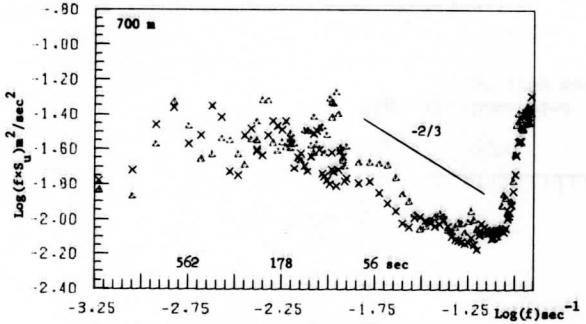

Fig. 14 . Down wind spectra of group 3 (Δ) and group 4 (x) at 700 meters.

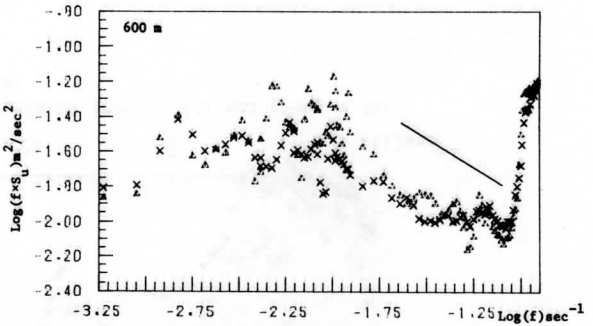

Fig. 15 . Down wind spectra of group 3 (Δ) and group 4 (x) at 600 meters.

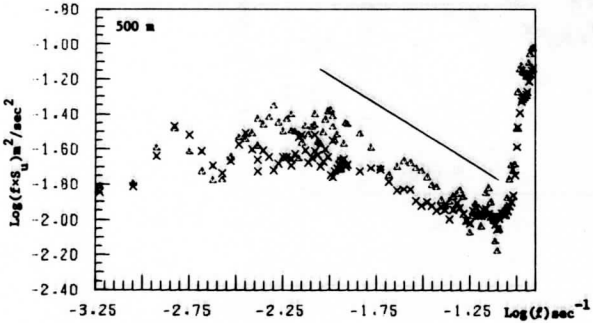

Fig. 16 . Down wind spectra of group 3 (Δ) and group 4 (x) at 500 meters.

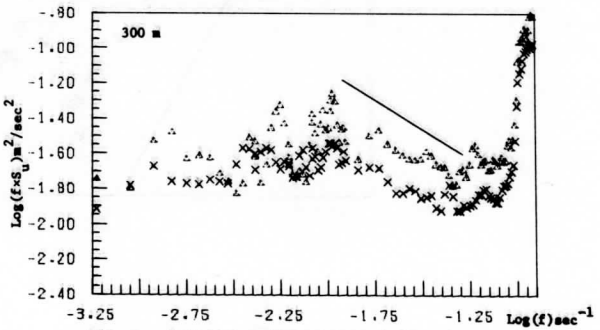

Fig. 17 . Down wind spectra of group 3 (Δ) and group 4 (x) at 300 meters.

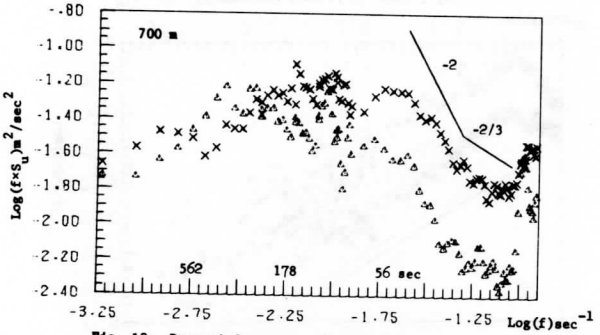

Fig. 18. Down wind spectra of group 1 (Δ) and group 2 (x) at 700 meters.

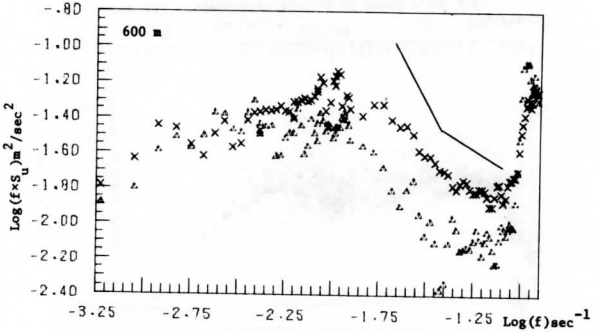

Fig. 19. Down wind spectra of group 1 (Δ) and group 2 (x) at 600 meters.

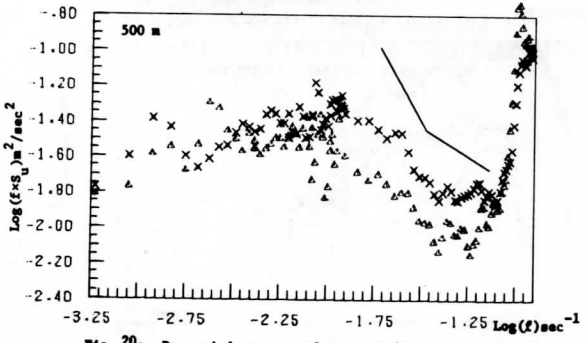

Fig. 20. Down wind spectra of group 1 (Δ) and group 2 (x) at 500 meters.

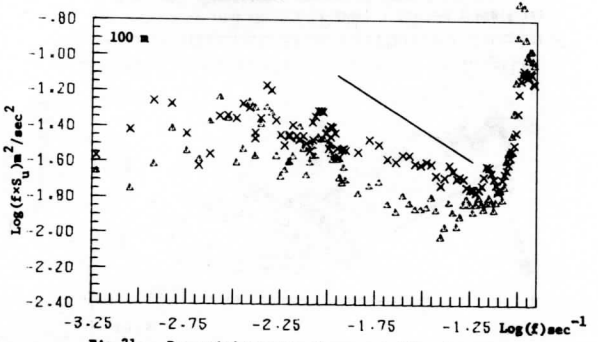

Fig. 21. Down wind spectra of group 1 (Δ) and group 2 (x) at 100 meters.

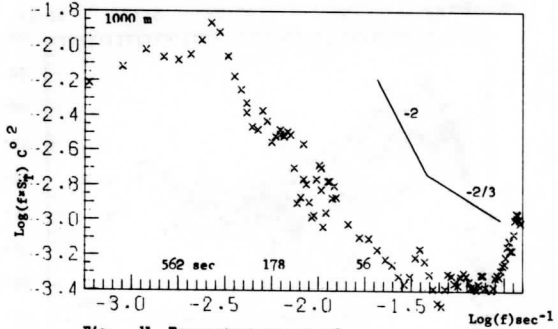

Fig. 22. Temperature spectra of group 4 (x) at 1000 meters.

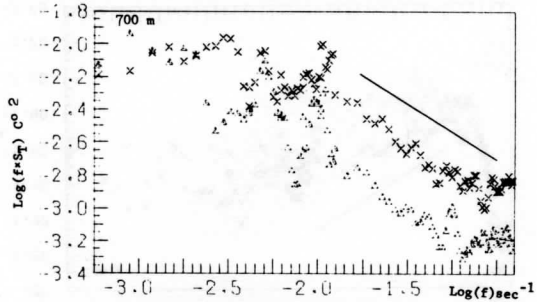

Fig. 23. Temperature spectra of group 3 (Δ) and group 4 (x) at 700 meters.

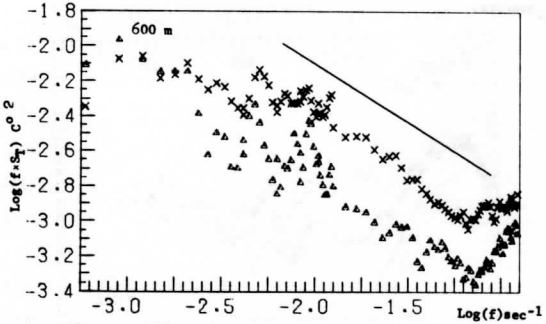

Fig. 24. Temperature spectra of group 3 (Δ) and group 4 (x) at 600 meters.

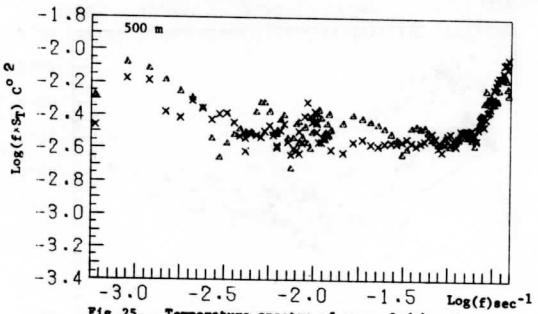

Fig 25. Temperature spectra of group 3 (Δ) and group 4(x) at 500 meters.

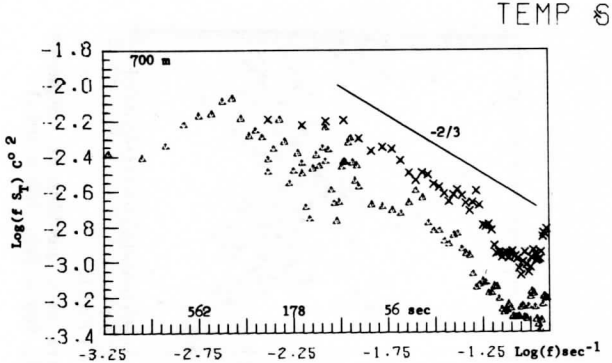

Fig. 26. Temperature spectra of group 1 ( ) and group 2 (x) at 700 meters.

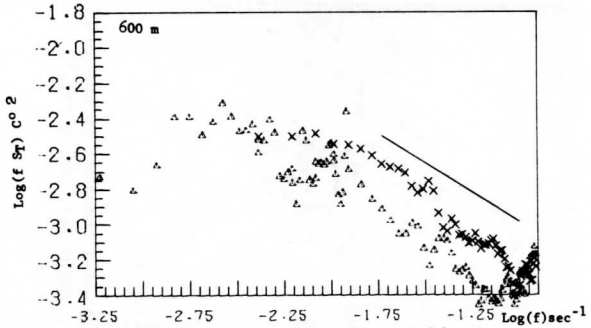

Fig. 27. Temperature spectra of group 1 ( ) and group 2 (x) at 600 meters.

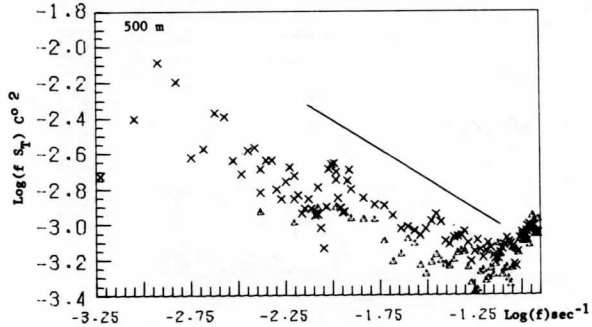

Fig. 28. Temperature spectra of group 1 ( ) and group 2 (x) at 500 meters.

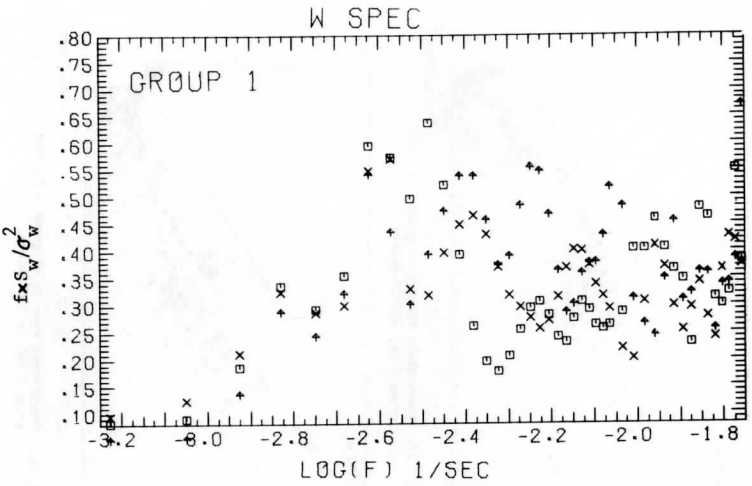

Figure 29. Vertical velocity spectra as a function of frequency and height. (700 m (□), 500 m (x), 100 m (+).)

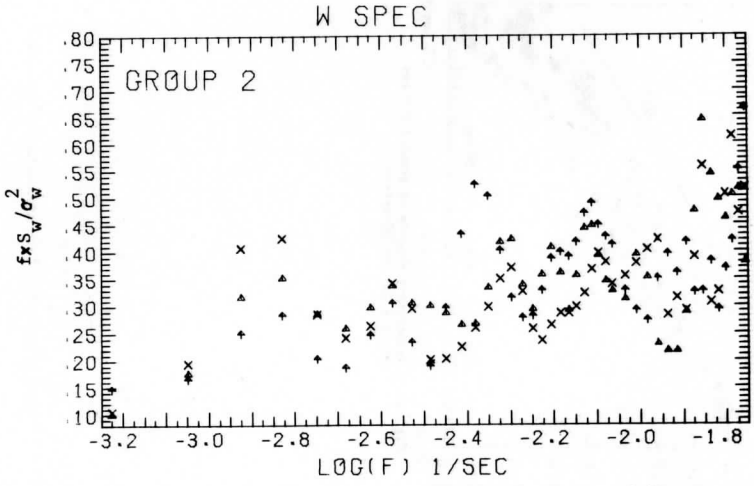

Figure 30. Vertical velocity spectra as a function of frequency and height. (600 m (Δ), 500 m (x), 100 m (+).)

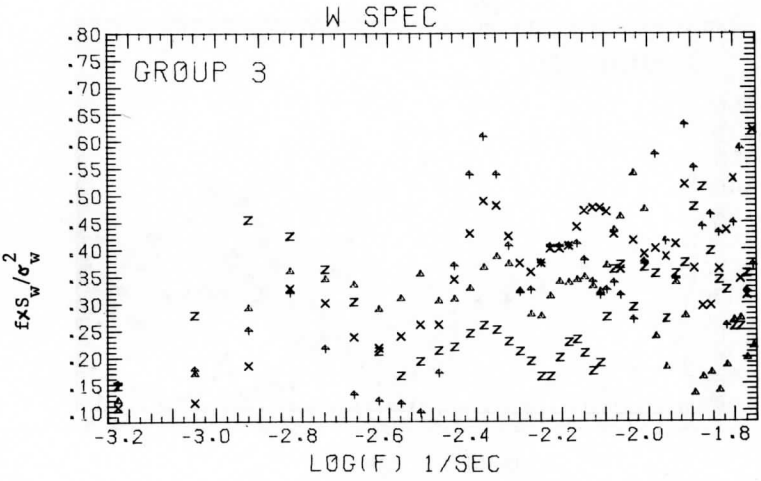

Figure 31. Vertical velocity spectra as a function of frequency and height. (1000 m (z), 600 m (Δ), 500 m (x), 300 m (+).)

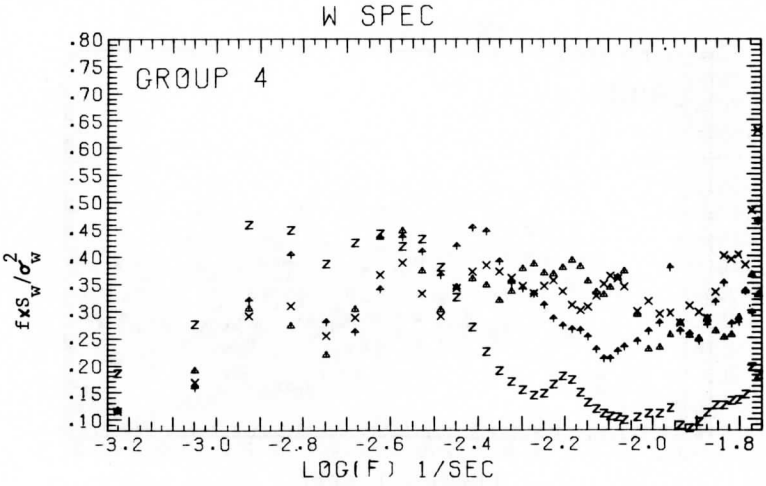

Figure 32. Vertical velocity spectra as a function of frequency and height. (1000 m (z), 600 m (Δ), 500 m (x), 300 m (+).)

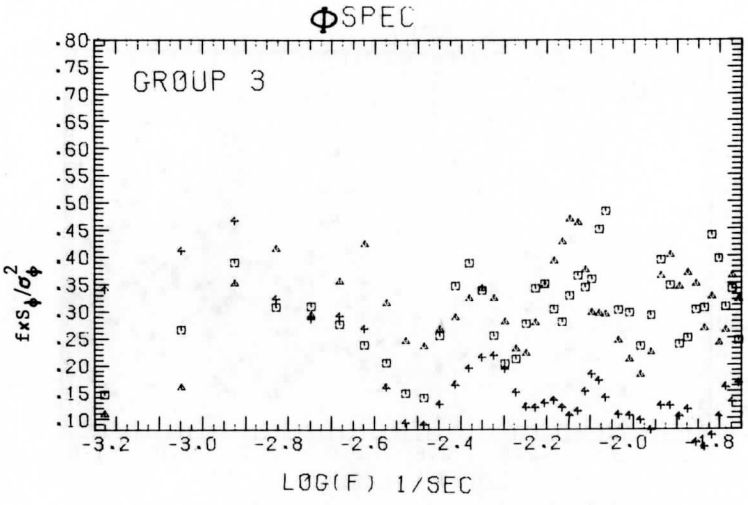

Figure 33. Horizontal angle spectra as a function of frequency and height. (700 m (□), 600 m (Δ), 300 m (+).)

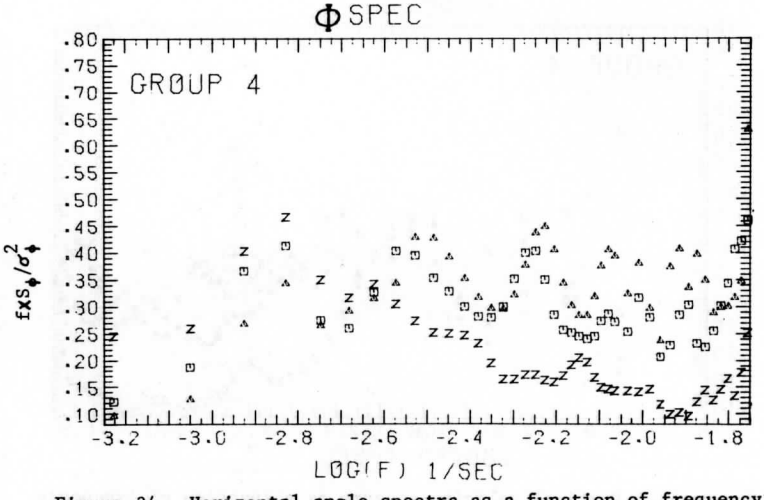

Figure 34. Horizontal angle spectra as a function of frequency and height. (1000 m (z), 700 m (□), 600 m (Δ).)

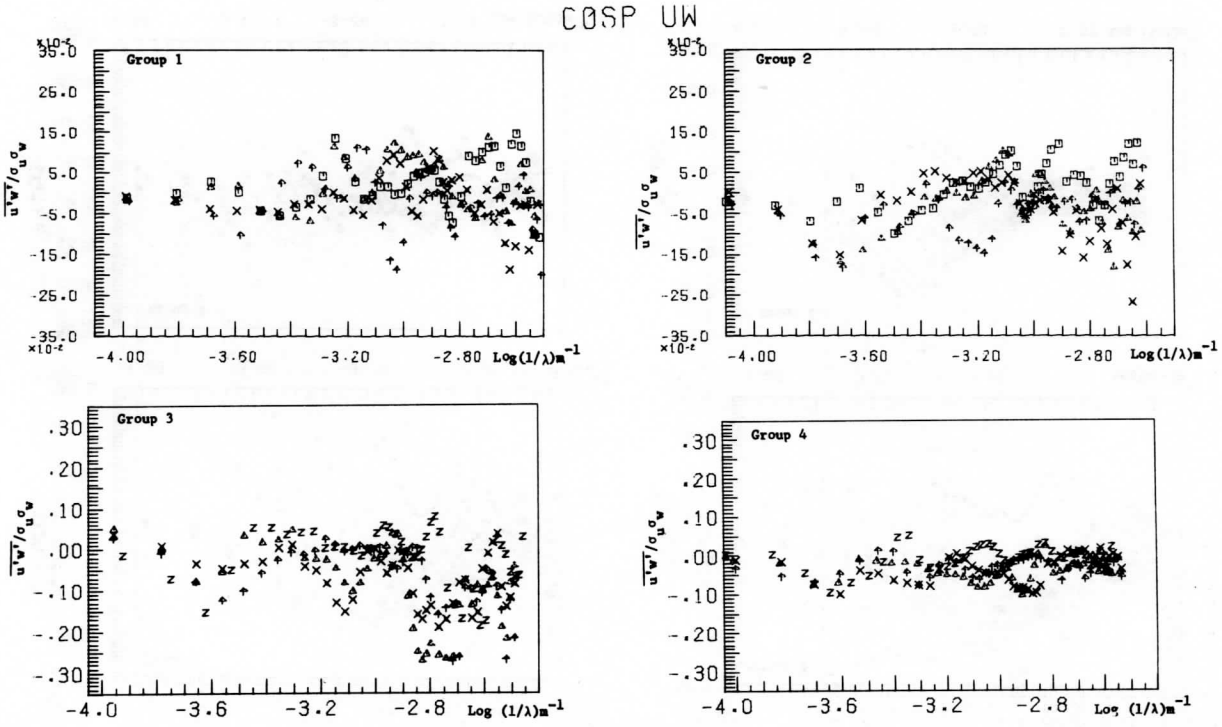

Figure 35. Cospectra of $\overline{u'w'}$ as a function of inverse wavelength and height. (1000 m (z), 700 m (□), 600 m (Δ), 500 m (x); Groups 1 and 2, 100 m (✦); Groups 3 and 4, 300 m (✦).)

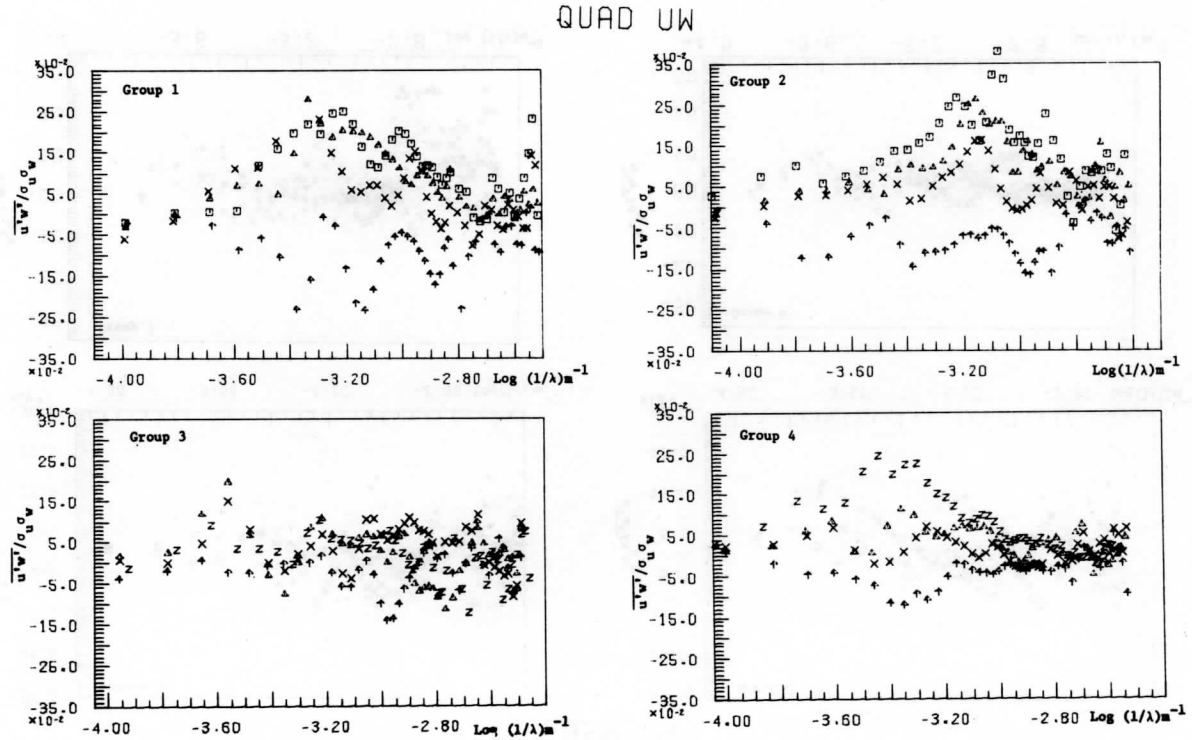

Figure 36. Quadrature spectra of $\overline{u'w'}$ as a function of inverse wavelength and height. (1000 m (z), 700 m (□), 600 m (Δ), 500 m (x); Groups 1 and 2, 100 m (↑); Groups 3 and 4, 300 m (↑).)

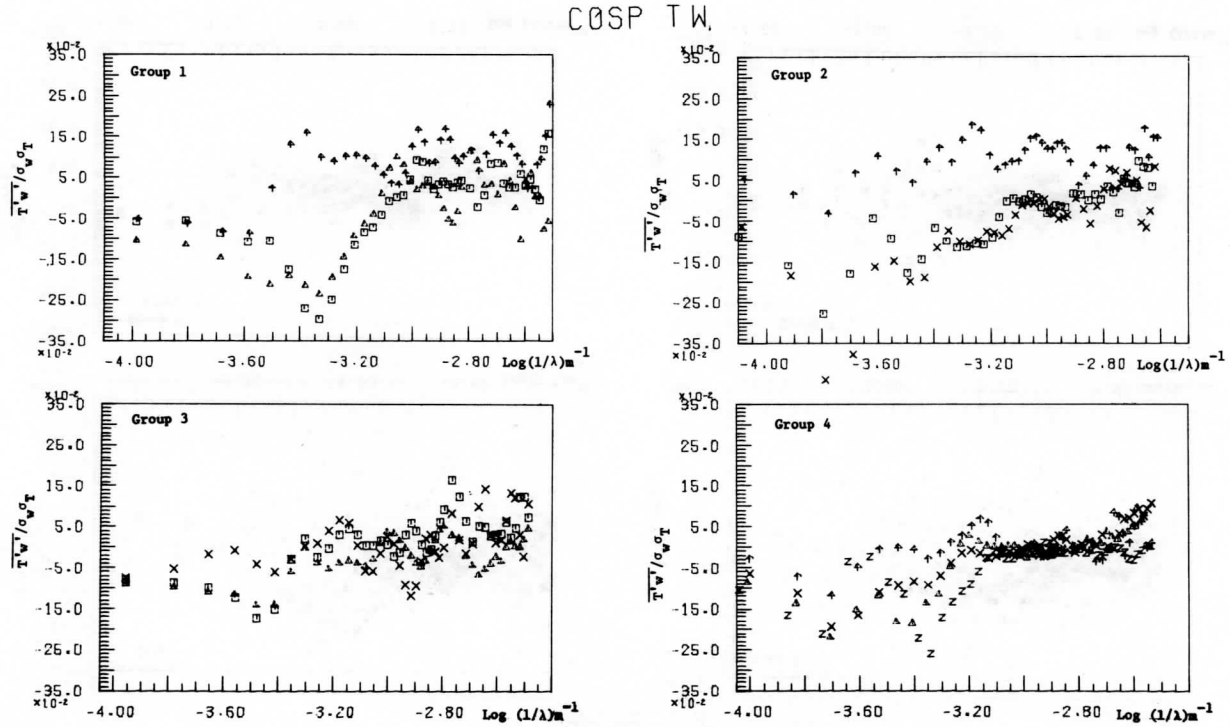

Figure 37. Cospectra of $\overline{T'w'}$ as a function of inverse wavelength and height. (1000 m (z), 700 m (□), 600 m (Δ), 500 m (x); Groups 1 and 2, 100 m (+); Groups 3 and 4, 300 m (+).)

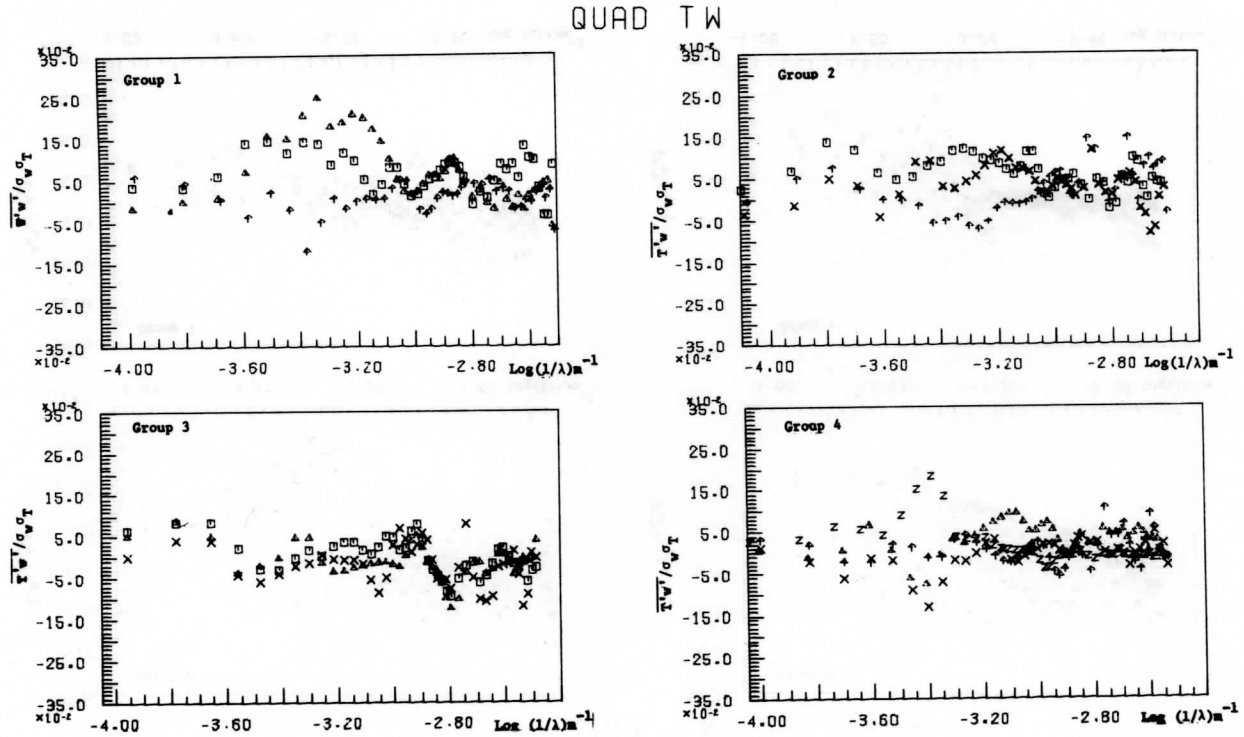

Figure 38. Quadrature spectra of $\overline{T'w'}$ as a function of inverse wavelength and height. (1000 m (z), 700 m (□), 600 m (Δ), 500 m (x); Groups 1 and 2, 100 m (+); Groups 3 and 4, 300 m (+).)

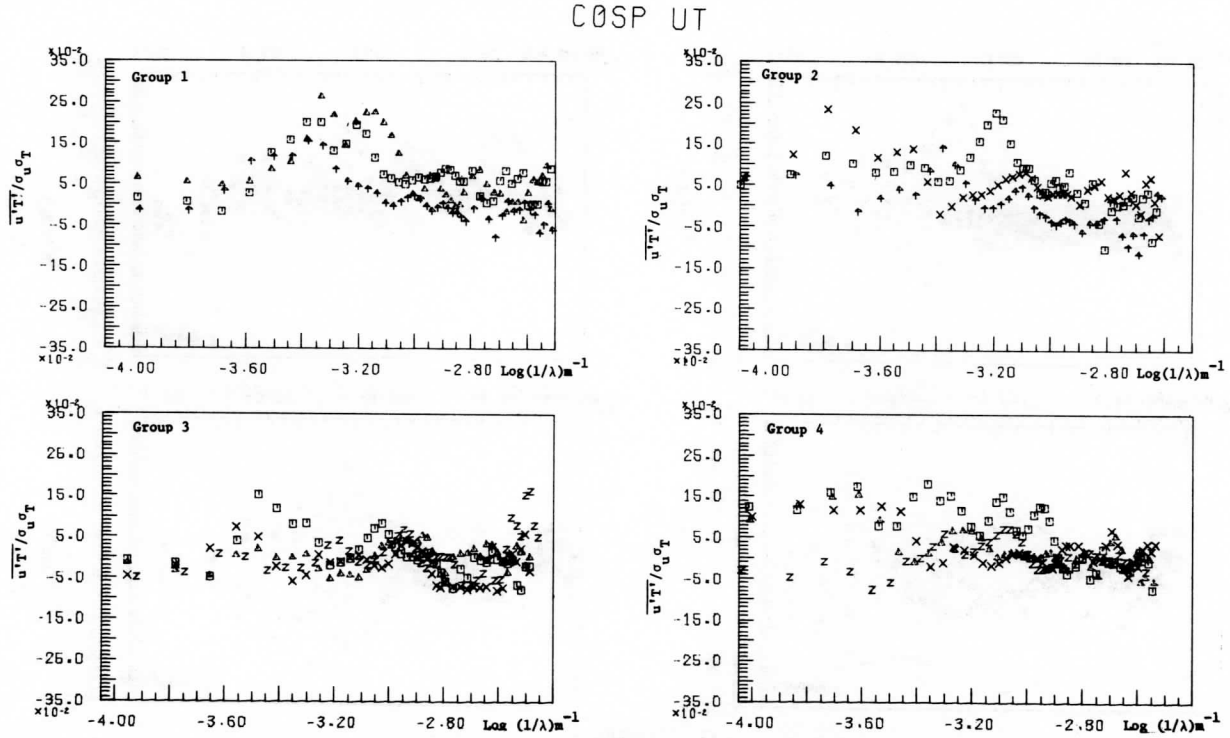

Figure 39. Cospectra of $\overline{u'T'}$ as a function of inverse wavelength and height. (1000 m (z), 700 m (□), 600 m (Δ), 500 m (x); Groups 1 and 2, 100 m (+); Groups 3 and 4, 300 m (+).)

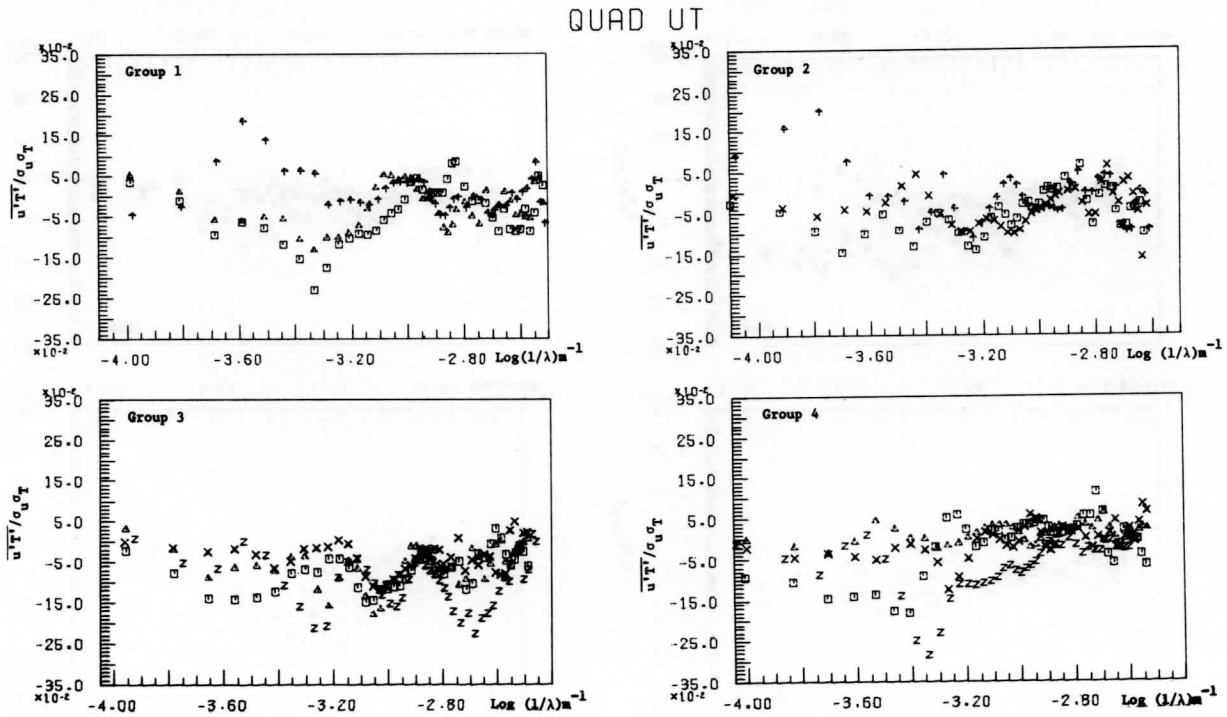

Figure 40. Quadrature spectra of $\overline{u'T'}$ as a function of inverse wavelength and height. (1000 m (z), 700 m (□), 600 m (Δ), 500 m (x); Groups 1 and 2, 100 m (+); Groups 3 and 4, 300 m (+).)

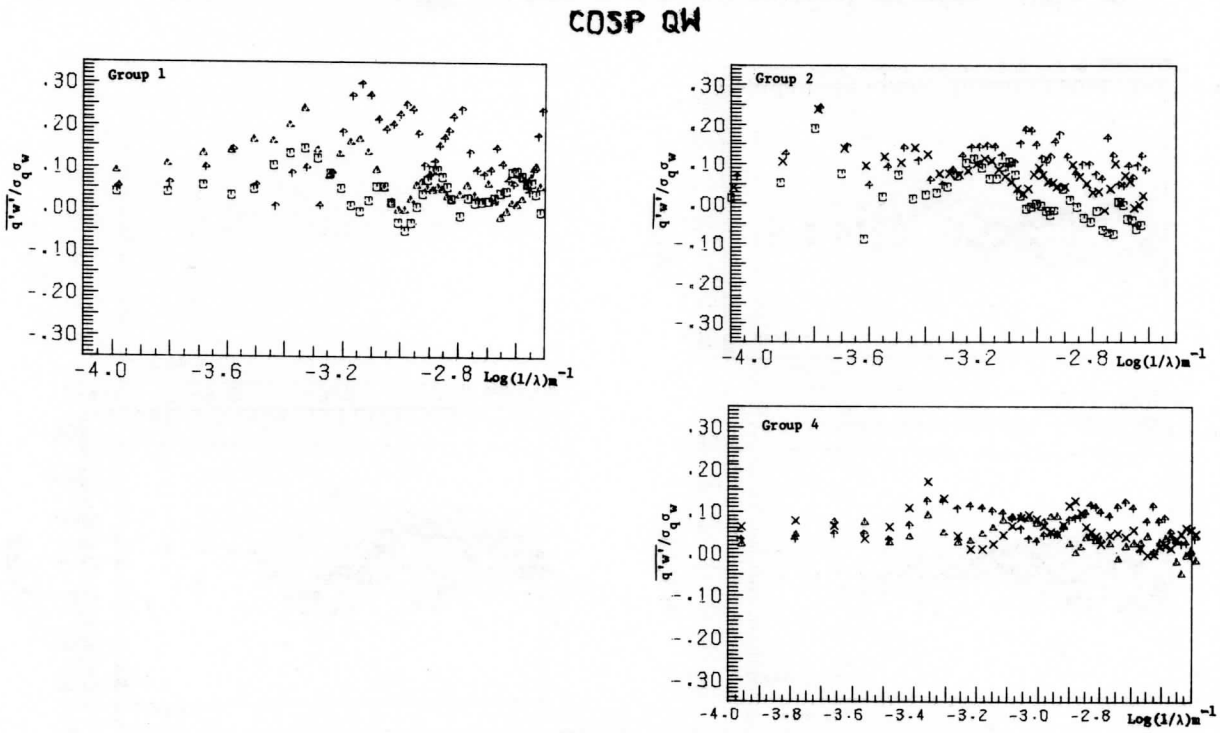

Figure 41. Cospectra of $\overline{q'w'}$ as a function of inverse wavelength and height. (700 m (□), 600 m (Δ), 500 m (x); Groups 1 and 2, 100m (+); Group 4, 300 m (+).)

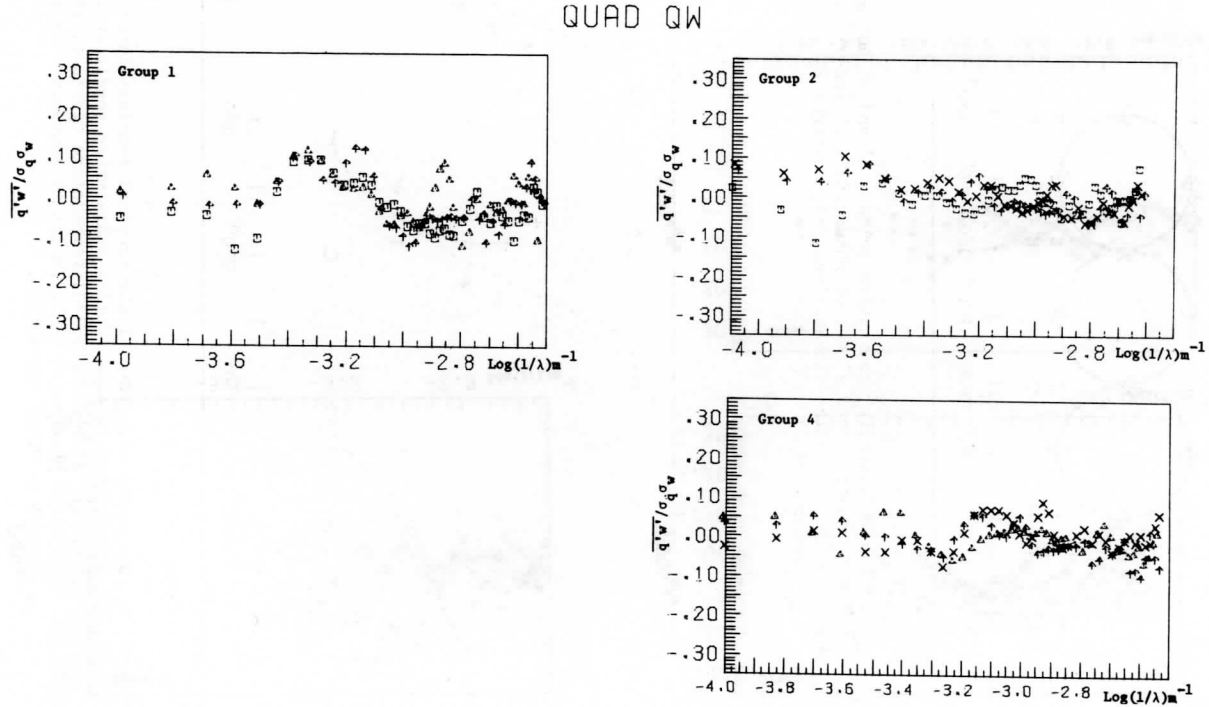

Figure 42. Quadrature spectra of $\overline{q'w'}$ as a function of inverse wavelength and height. (700 m (□), 600 m (▲), 500 m (x); Groups 1 and 2, 100 m (+); Groups 4, 300 m (+).)

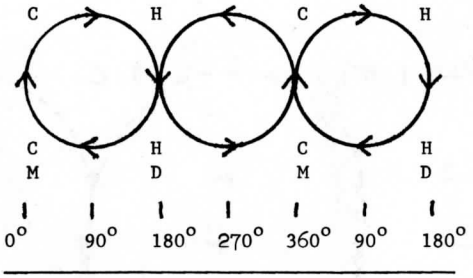

Figure 43. Ideal "indirect" convective cells. u' and w' 90° out of phase; T' and w' out of phase 180°; q' and w' in phase. Velocity fluctuations (↑), temperature (H,C), moisture (M,D).

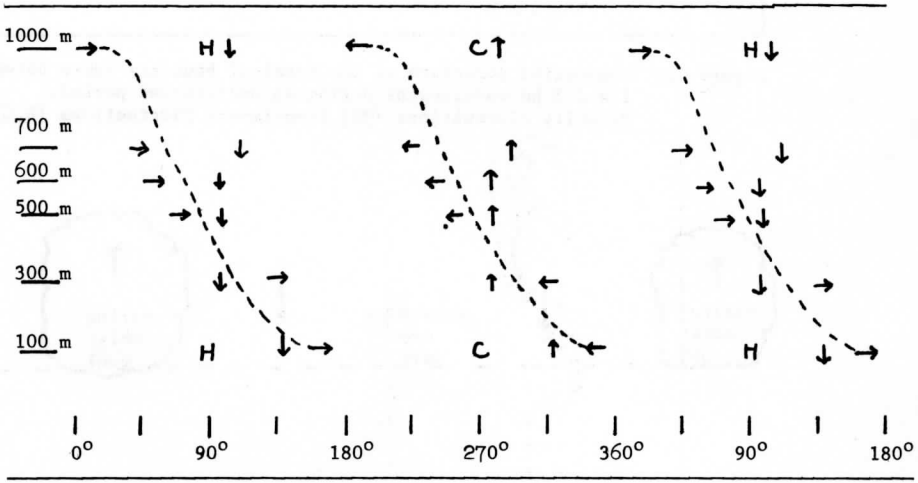

Figure 44. Turbulent structure of the tropical boundary layer near wavelengths of 6 km. during undisturbed conditions. Velocity fluctuations (↑); temperature fluctuations (H,C). q' is in phase with w' but moisture buoyancy is not large enough to drive convection.

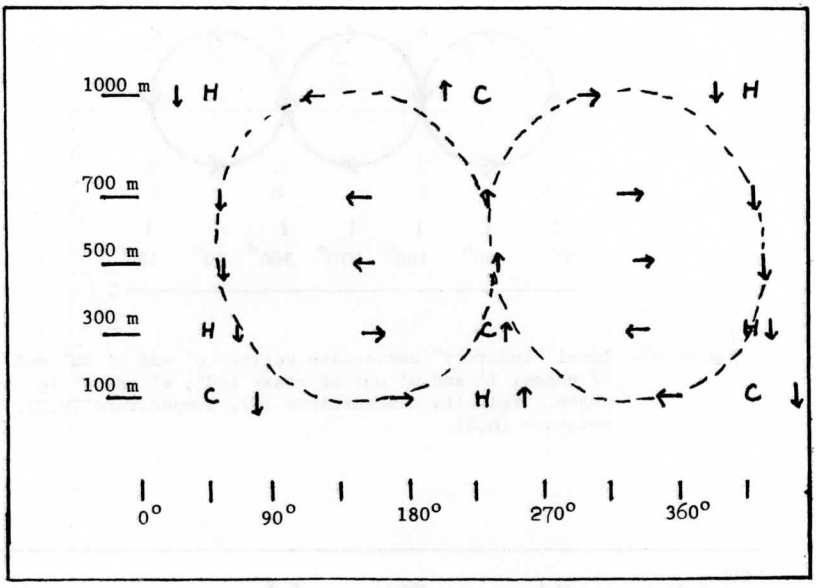

Figure 45. Convective structure of the tropical boundary layer between 1 and 3 km wavelengths during an undisturbed period. Velocity fluctuations (↑); temperature fluctuations (H,C).

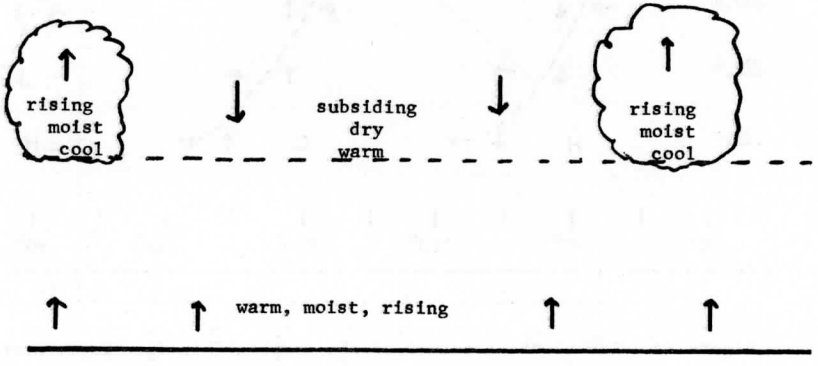

Figure 46.

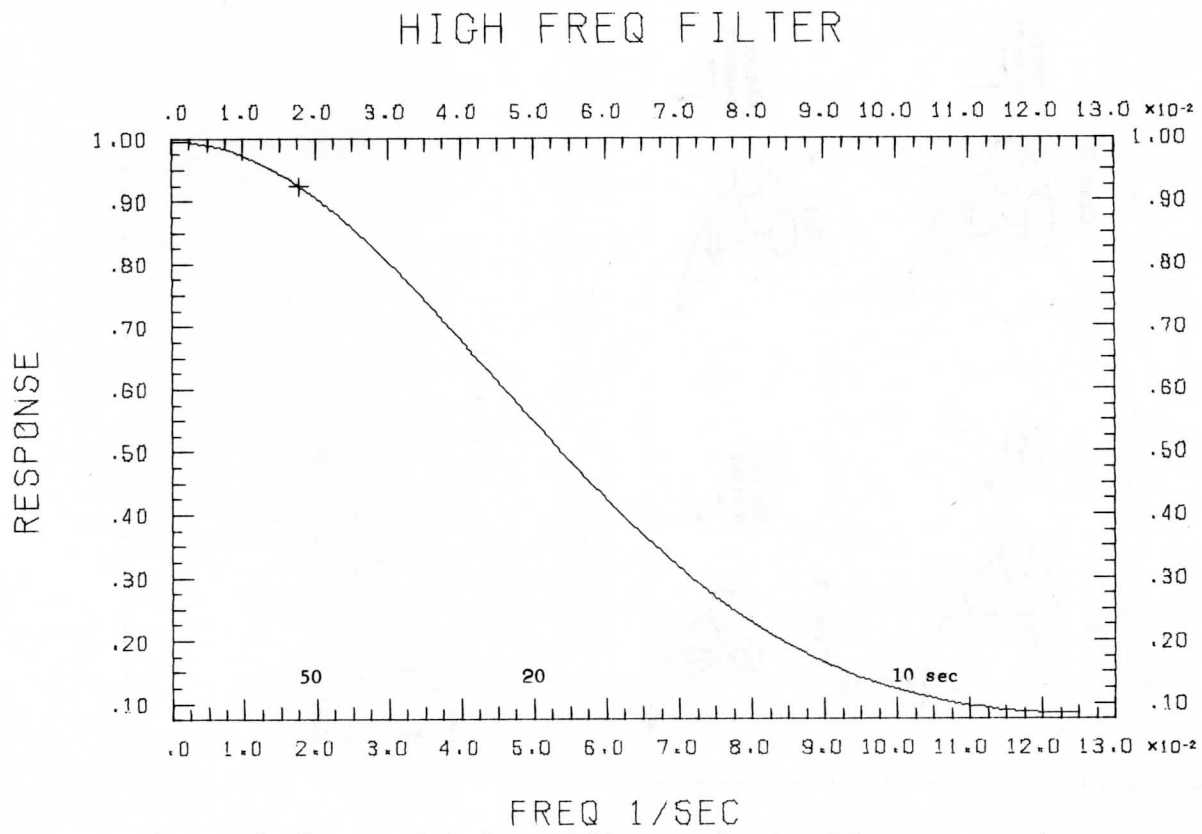

Figure A.1. Response of the low pass filter as a function of frequency. + marks the location of the high frequency cut off for cross spectral analysis.

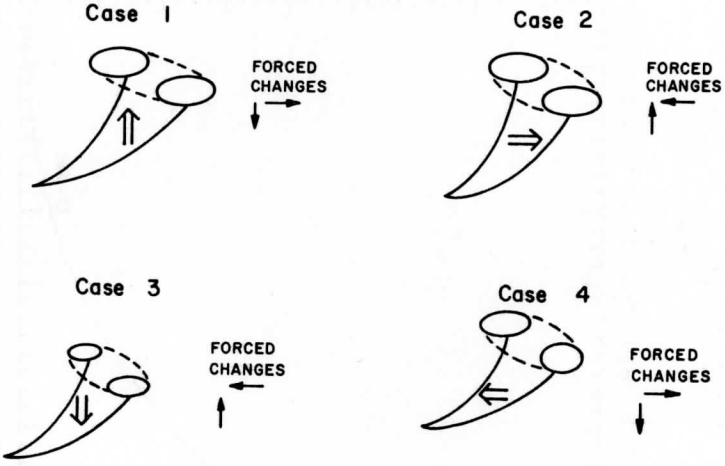
Case 1
FORCED CHANGES
Case 2
FORCED CHANGES
Case 3
FORCED CHANGES
Case 4
FORCED CHANGES

Figure B.1.

REPORTS AVAILABLE FROM

THE UNIVERSITY OF WISCONSIN PRESS, BOX 1379, MADISON, WISCONSIN 53701

97024. Studies in Atmospheric Energetics Based on Aerospace Probings: Annual Report, 1966. 129 pages. 1967. $5.00

97026. Studies in Atmospheric Energetics Based on Aerospace Probings: Annual Report, 1968. 162 pages. 1969. $5.00

97027. Radiation Experiment in the Vicinity of Barbados: Final Report, NSF Grant Ga. 12603. 100 pages. 1970. $5.00

97028. The Study of Radiation in a Tropical Atmosphere: Final Report. 100 pages. 1970. $5.00

97029. The Educational and Social Uses of Communications Satellites: A Bibliography. 42 pages. 1970. $3.50

97030. Measurements from Satellite Platforms: Annual Scientific Report on NAS5-11542, 1968-69. 388 pages. 1970. $10.00

97031. A Pilot Study on the Application of Geosynchronous Meteorological Satellite Data to Very Short Range Terminal Forecasting. 113 pages. 1970. $5.00

97032. Studies of the Atmosphere Using Aerospace Probings: Annual Report, 1969. 243 pages. 1970. $7.50

97033. Teleconferencing: A Bibliography. 1971. $3.50

97034. Legal and Political Aspects of Satellite Telecommunication: An Annotated Bibliography. 126 pages. 1971. $7.50

97035. Multidisciplinary Studies of the Social, Economic, and Political Impact Resulting from Recent Advances in Satellite Meteorology: An Interim Report, Vol. 1. 459 pages. 1971. $15.00

97036. Multidisciplinary Studies of the Social, Economic, and Political Impact Resulting from Recent Advances in Satellite Meteorology: An Interim Report, Vol. 2. 431 pages. 1971. $15.00

97037. Measurements from Satellite Platforms: Annual Scientific Report on NAS5-11542, 1969-70. 180 pages. 1971. $7.50

97038. Studies of the Atmosphere Using Aerospace Probings: Annual Report, 1970. 69 pages. 1971. $5.00

97039. Legal Aspects of Satellite Teleconferencing. 213 pages. 1971. $7.50

97040. Teleconferencing in Wisconsin. 240 pages. 1971. $10.00

97041. Measurements from Satellite Platforms: Annual Scientific Report on NAS5-11542, 1970-71. 270 pages. 1972. $10.00

REPORTS AVAILABLE FROM

THE UNIVERSITY OF WISCONSIN PRESS, BOX 1379, MADISON, WISCONSIN 53701

(continued from inside back cover)

97042. Experiments in Medical Communications via the ATS-1 Satellite. 136 pages. 1972. $7.50

97043. Specifications for a Vertical Temperature and Moisture Sounder for the Synchronous Meterological Satellites. 82 pages. 1972. $5.00

97044. Scientific Requirements of Sea Surface Measurements for the GARP Tropical Experiment. 18 pages. 1972. $2.50

97045. Studies of the Atmosphere Using Aerospace Probings: Annual Report, 1971, Vol. II: Application Studies. 104 pages. 1972. $5.00

97046. Multidisciplinary Studies of the Social, Economic, and Political Impact Resulting from Recent Advances in Satellite Meteorology: An Interim Report, Vol. 3. 252 pages. 1972. $10.00

97047. Multidisciplinary Studies of the Social, Economic, and Political Impact Resulting from Recent Advances in Satellite Meteorology: An Interim Report, Vol. 4. 199 pages. 1972. $10.00

97048. Satellite Teleconferencing: An Annotated Bibliography. 130 pages. 1972. $7.50

97049. Measurements from Satellite Platforms: Annual Scientific Report on NAS5-11542, 1971-72. 228 pages. 1972. $7.50

97050. Synchronous Meteorological Satellite Sounder Specification: Final Report Under NASA Contract NAS5-21607. 73 pages. $5.00

97051. Multidisciplinary Studies of the Social, Economic, and Political Impact Resulting from Recent Advances in Satellite Meteorology: An Interim Report, Vol. 5. 290 pages. 1973. $10.00

97052. Measurements from Satellite Platforms: Annual Scientific Report on NAS5-21798, 1972-73. 331 pages. 1974. $10.00

97053. Visual Channel Data Analysis for Synchronous Meterological Satellite. Scientific Report on NOAA/NESS Grant NG-26-72. 252 pages. 1974. $7.50

97054. Studies of the Atmosphere Using Aerospace Probes. Annual Report, 1973. 272 pages. 1974. $7.50

97055. Meteorological Measurements from Satellite Platforms. Annual Scientific Report on NAS5-21798, 1973-74. 97 pages. 1975. $5.00

97056. Studies of the Atmosphere Using Aerospace Probes. Annual Report, 1974. 154 pages. 1975. $5.00